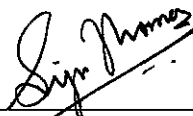


MULTISCALE MODELING OF THIN FILMS IN DIRECT NUMERICAL SIMULATIONS OF MULTIPHASE FLOWS

by

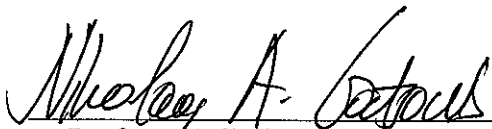


Siju Thomas

A dissertation submitted to the faculty of
Worcester Polytechnic Institute in partial fulfillment
of the requirements for the degree of
Doctor of Philosophy in Mechanical Engineering, 2009



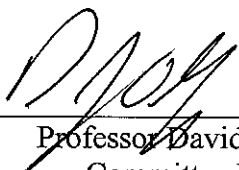
Professor Grétar Tryggvason
Advisor



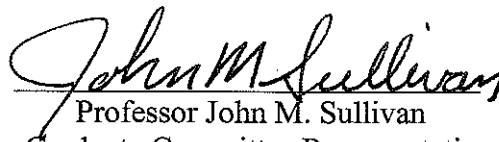
Professor Nikolaos A. Gatsolis
Committee Member



Professor Mayer Humi
Committee Member



Professor David J. Olinger
Committee Member



Professor John M. Sullivan
Graduate Committee Representative

ABSTRACT

Direct numerical simulations, where both the large and small scales in the flow are fully resolved, provide an excellent instrument to validate multiphase flow processes and also further our understanding of it. Three multiphase systems are studied using a finite difference/front-tracking method developed for direct numerical simulations of time-dependent systems. The purpose of these studies is to demonstrate the benefit in developing accurate sub-grid models that can be coupled with the direct numerical simulations to reduce the computational time. The primary reason to use the models is that the systems under consideration are sufficiently large that resolving the smallest scales is impractical. The processes that are examined are: (1) droplet motion and impact (2) nucleate boiling and (3) convective mass transfer.

For droplet impact on solid walls and thin liquid films, the splash characteristics are studied. The collision of a fluid drop with a wall is examined and a multiscale approach is developed to compute the flow in the film between the drop and the wall. By using a semi-analytical model for the flow in the film we capture the evolution of films thinner than the grid spacing reasonably well.

In the nucleate boiling simulations, the growth of a single vapor from a nucleation site and its associated dynamics are studied. The challenge here is the accurate representation of the nucleation site and the small-scale motion near the wall. To capture the evaporation of the microlayer left behind as the base of the bubble expands we use a semi-analytical model that is solved concurrently with the rest of the

simulations. The heat transfer from the heated wall, the evolution of the bubble size and the departure diameter are evaluated and compared with the existing numerical results.

The mass transfer near the interface, without fully resolving the layer by refining the grid is accommodated by using a boundary layer approximation to capture it. The behavior of the concentration profile is taken to be self-similar. A collection of potential profiles is tested and the accuracy of each of these models is compared with the full simulations.

*To Mummy, Daddy & Aju
Without your love and prayers, this would have never been possible.*

ACKNOWLEDGEMENTS

I thank the Lord Almighty for giving me the strength and desire to undertake the enormous task of getting a doctorate. All to Jesus, I surrender.

I would like to thank my parents and my brother for their selfless love, positive reinforcements and constant support at all times. Very few things in life are this reliable.

No amount of words can adequately describe the gratitude that I have for Prof. Grétar Tryggvason for advising me on this dissertation. I thank him for sharing his immense knowledge, patiently enduring my laziness and ineptitude, and generously helping me out in times of need.

I would also like to thank all the fellow members, past and present, of the Multiphase Flow Group at WPI for all the interactions and advice that has helped shape my thinking and understanding of CFD and multiphase flows. Special mention should be made of Prof. Asghar Esmaeeli, Prof. Damir Juric, Prof. Jiakai Lu and Dr. Souvik Biswas for helping me out at various times during my research.

The efficiency and kindness shown to me by the administrative personnel at the Mechanical Engineering Department throughout my studies was singularly exemplary and I will remember it with fondness. The services rendered by Mr. Siamak Najafi and Mr. Randy Robinson in ensuring adequate computational resources for running my

simulations as well as dealing with a number of other technological issues go beyond the call of duty.

I would like to thank all the professors who have taught me over the years. Learning from such dedicated teachers has instilled in me a continuous thirst for knowledge and reverence for the profession of teaching.

I register my deepest thanks to the Worcester Polytechnic Institute for admitting me into the graduate program six years ago. It is a source of immense pride for me to graduate from an institution of glorious academic traditions, highest ethical standards and social responsibility.

Finally, I would like to sincerely thank all my friends and colleagues for their immeasurable help through the years. They have made my graduate experience enriching and fulfilling. Only the restrictions of space and lethargy prevent me from listing each one of them by name. I continue to hold dear their camaraderie and companionship. Last, but not the least, I owe a debt of gratitude to my friends at the MKR Society and the OYC who have always been there for me.

TABLE OF CONTENTS

ABSTRACT.....	ii
ACKNOWLEDGEMENTS.....	v
TABLE OF CONTENTS.....	vii
LIST OF FIGURES.....	x
LIST OF TABLES.....	xvi
CHAPTER 1 - INTRODUCTION.....	1
1.1 Motivation.....	2
1.1.1 Numerical simulations of multiphase flows.....	2
1.1.2 Multiscale modeling of multiphase flows.....	4
1.2 Scope of the present work.....	5
CHAPTER 2 - FORMULATION AND NUMERICAL METHOD.....	8
2.1 The front-tracking method.....	8
2.2 Governing Equations.....	9
2.3 Time Integration.....	12
2.4 Finite Difference Equations and Boundary Conditions.....	14
2.5 The Front-Tracking Method.....	19
2.6 Validation of the front-tracking code.....	21
CHAPTER 3 - ON THE IMPACT OF DROPS ON THIN LIQUID FILMS.....	35
3.1 Introduction.....	35
3.2 Literature Review.....	36
3.3 Problem Statement and Numerical Formulation.....	46
3.3.1 Results and Discussion.....	46
3.3.2 Effect of dissipation on crown height.....	51

3.3.3 Effect of dissipation on crown radius	52
3.3.4 Effect on kinetic energy and surface energy	53
3.4 Conclusions.....	54
CHAPTER 4 - MODELING THIN FILMS NEAR A SOLID WALL	70
4.1 Introduction.....	70
4.2 Problem setup.....	73
4.3 Theory of thin film modeling.....	74
4.4 Results and Discussions.....	78
4.5 Conclusions.....	81
CHAPTER 5 - MICROLAYER MODELING IN NUCLEATE BOILING	98
5.1 Introduction.....	98
5.2 Problem Setup.....	102
5.3 Governing Equations	103
5.4 Microlayer model.....	104
5.5 Results and discussion	106
5.6 Conclusions.....	108
CHAPTER 6 - MASS TRANSFER.....	121
6.1 Introduction.....	121
6.2 Governing Equations	129
6.3 Time evolution of the profiles.....	131
6.3.1 Evolution of the linear profile.....	131
6.3.2 Evolution of the quadratic profile.....	132
6.3.3 Evolution of the bi-linear profile	134
6.3.4 Evolution of the exponential profile	135
6.4 Results and Discussion	138

6.4.1 Linear Model.....	139
6.4.2 Quadratic Model	139
6.4.3 Bi-linear model	139
6.4.4 Exponential model	140
6.4.5 Reducing the Diffusion Coefficient.....	140
6.4.6 Raising the Velocity.....	141
6.5 Conclusions.....	141
CHAPTER 7 - SUMMARY AND FUTURE WORK.....	163
7.1 Summary	163
7.2 Recommendations for future work	165
7.2.1 Droplet Impact	165
7.2.2 Nucleate Boiling	165
7.2.3 Mass Transfer.....	166
BIBLIOGRAPHY	168

LIST OF FIGURES

Figure 2.1: Schematic of the computational domain in axisymmetric coordinates.....	24
Figure 2.2 : The layout of the staggered grid mesh that is used in the computations. The pressure nodes are located at the center of each cell, and the velocity nodes are the cell faces.....	25
Figure 2.3 : Transformation of the grid. r is the coordinate in the physical domain and ξ is the coordinate the computational domain.....	26
Figure 2.4: Sketch of the left boundary under the staggered grid. The left boundary is the axis of symmetry.....	27
Figure 2.5: The grid and the front. The grey points represent the front and the white ones the grid. The front point gets its values from the corner points of the grid cell it is located.....	28
Figure 2.6: Front tracking – interpolating from the grid by area weighting.....	29
Figure 2.7: Front structure is sketched.....	30
Figure 2.8: Volume element in axisymmetric coordinates.....	31
Figure 2.9: The forces acting on the surface element in axisymmetric coordinates.....	32
Figure 2.10: Convergence of calculated rise velocity to the theoretical value.....	33
Figure 2.11: Rise velocity of a bubble in creeping flow. h is the grid size of the computational domain. The terminal velocity approaches the predicted value at a higher grid resolution.....	34
Figure 3.1 Problem setup. The initial diameter of the drop is D and the initial velocity is U . The thickness of the liquid film is H	56
Figure 3.2: Splash Progression at initial velocity $U = 2.0$, $Re = 100$, $We = 32000$. Grid dimensions are 2×1 . The number of grid points in the present case are 256×128 . The grid resolution is non-uniform, with a minimum grid size of 0.005	57
Figure 3.3: Splash Progression at initial velocity $U = 2.0$, $Re = 200$, $We = 32000$. Grid dimensions are 2×1 . The number of grid points in the present case is 256×128 . The grid resolution is non-uniform, with a minimum grid size of 0.005	58

Figure 3.4: Splash Progression at initial velocity $U = 2.0$, $Re = 250$, $We = 32000$. Grid dimensions are 2×1 . The number of grid points in the present case is 256×128 . The grid resolution is non-uniform, with a minimum grid size of 0.005 59

Figure 3.5: Splash Progression for the full-slip wall condition at initial velocity $U = 2.0$, $Re = 250$, $We = 32000$. Grid dimensions are 2×1 . The number of grid points in the present case is 256×128 . The grid resolution is non-uniform, with a minimum grid size of 0.005 60

Figure 3.6: Square of the crown radius versus time under two sets of conditions. The straight line indicates the linear relationship between the crown radius and the square-root of time..... 61

Figure 3.7: The evolution of the height of the crown from the time of impact to the end of the splash. The first figure is with the full-slip wall conditions and the second figure is for the no-slip case. The initial velocity is $U = 2.0$ and Weber Number, $We = 32000$ and Reynolds numbers ranging from 50 to 250. The thickness of the thin film is 0.035 62

Figure 3.8: The evolution of the height of the crown from the time of impact to the end of the splash. The first figure is with the full-slip wall conditions and the second figure is for the no-slip case. The initial velocity is $U = 2.0$ and Reynolds Number, $Re = 200$ and Weber number, $We = 11520, 20400, 32000$. The thickness of the film is 0.035 . .63

Figure 3.9: The progression of the radius of the crown from the time of impact to the end of the splash. The first figure is with the full-slip wall conditions and the second figure is for the no-slip case. The initial velocity is $U = 2.0$ and Weber Number, $We = 32000$ and Reynolds numbers ranging from 50 to 250. The thickness of the thin film is 0.035 64

Figure 3.10: The progression of the radius of the crown from the time of impact to the end of the splash. The first figure is with the full-slip wall conditions and the second figure is for the no-slip case. The initial velocity is $U = 2.0$ and Reynolds Number, $Re = 200$ and Weber number, $We = 11520, 20400, 32000$. The thickness of the film is 0.035 65

Figure 3.11: The kinetic energy of the system from the time of impact to the end of the splash. The first figure is with the full-slip wall conditions and the second figure is for the no-slip case. The initial velocity is $U = 2.0$ and Weber Number, $We = 32000$ and Reynolds numbers, $Re = 100$ and $Re = 250$ 66

Figure 3.12: The surface energy of the system from the time of impact to the end of the splash. The first figure is with the full-slip wall conditions and the second figure is for the no-slip case. The initial velocity is $U = 2.0$ and Weber Number, $We = 32000$ and Reynolds numbers, $Re = 100$ and $Re = 250$ 67

Figure 4.1: The motion of a drop falling down a wall with a 45 degree slope, computed using three different resolutions as described in the text. The thick line is fully converged results computed on two fine stretched grids. The results shown by a thin line are computed on a coarse uniform grid..... 84

Figure 4.2: The flow in the thin film, corresponding to the third frame in figure 1, as computed on the finest grid. The top frame shows the flow near the back of the drop, the middle frame shows the flow in the middle and the bottom frame shows the flow near the front. 85

Figure 4.3: The location of the drop centroid versus time (top) and the minimum thickness of the film (bottom) for the simulations shown in figure 1, computed on two stretched fine grids and a coarse uniform grid..... 86

Figure 4.4: Staggered grid at the bottom wall. The u-velocity at the wall is obtained by the interpolation of the velocities at the ghost point and its corresponding point at the next y-location. 87

Figure 4.5: Sketch of the profile of the thin film model in relation to the front and the staggered grid. The Q and h values are evaluated at the pressure nodes, while uf is calculated at the u-velocity nodes. 88

Figure 4.6: Spreading of the droplet on a solid surface. Time $t^* = 1.0$ is the point at which the drop is at its maximum spread. $Re = 100$, $We = 50$ 89

Figure 4.7: Close-up of the front near the wall during the full simulations at $t^* = 1.0$. The minimum grid size close to the front is 0.001. The X-axis values over the three figures range from 0.06 to 0.38. Note that at the maximum spread position, the velocity vectors are smaller in size, indicating the end of its outward motion. 90

Figure 4.8: Comparison of the shape of the splat at different times ($t^* = 0.2$, $t^* = 0.5$ and $t^* = 1.0$) for the model, coarse grid and full simulations. 91

Figure 4.9: Close-up views of the splat, highlighting the difference between the model and the coarse grid simulations. 92

Figure 4.10: (Top) Drop spread radius comparison for the model, coarse grid and the full simulations. (Bottom) Drop height comparison for the model, coarse grid and the full simulations. 93

Figure 4.11: Comparison of results from simulations on a coarse grid using the wall-film model (dashed line), with direct numerical simulations using the coarse grid without the model (thin line) and the fine stretched grid (thick line) at three times. The coarse grid results with the film model agree reasonably well with the results using the fine grid. 94

Figure 4.12: The location of the centroid of the drop (top) and the minimum thickness of the film near the wall as computed a coarse grid using the wall-film model (dashed line), with direct numerical simulations using the coarse grid without the model (thin line) and the fine stretched grid (thick line) at three times. The coarse grid results with the film model agree reasonably well with the results using the fine grid.95

Figure 4.13: Motion of a drop computed on a course grid with and without the wall-model (top). Location of the centroid of the drop over time (middle). The minimum thickness of the film near the wall (bottom). The thick line denotes results with the wall-model and the thin lines is results without the model.....96

Figure 4.14: Motion of a drop computed on a course grid with and without the wall-model (top). Location of the centroid of the drop over time (middle). The minimum thickness of the film near the wall (bottom). The thick line denotes results with the wall-model and the thin lines is results without the model.....97

Figure 5.1: Setup of the nucleate boiling problem. The temperature at the liquid-vapor interface is the saturation temperature of the liquid..... 110

Figure 5.2: Schematic of microlayer..... 111

Figure 5.3: Modeling of the evaporation of the microlayer left behind as the apparent contact line moves outward. The location of the point where the front meets the wall is found by extrapolating the front to the wall..... 112

Figure 5.4: The growth of a vapor bubble in nucleate boiling. The time interval between two successive frames is 1 sec, starting at time, $t = 0$ 113

Figure 5.5: Close-up of the temperature contours around the vapor bubble at different times. (Top) Time, $t = 4$. (Middle) Time, $t = 8$. (Bottom) Time, $t = 9$ 114

Figure 5.6: Bubble diameter till the departure occurs. The dashed line refers to a wall superheat of 2, while the solid line is for a wall superheat of 1. The end point of each line indicates the point of departure of the bubble..... 115

Figure 5.7: Bubble diameter over time. The solid line denotes bubble diameter for a wall superheat of 2, while dashed line is for a wall superheat of 3, and the circular dots represent the experimental results obtained by Seigel and Keshock (1964). 116

Figure 5.8: Variation of Nusselt Number over time during bubble growth for wall superheat of 1..... 117

Figure 5.9: (Top) Comparison of Nusselt number with the results of Juric et al. (Bottom) Average Nusselt Number from inception to departure for different wall superheats..... 118

Figure 5.10: Comparison of the bubble shapes after the addition of the microlayer at a wall superheat of 2. The blue line shows the bubble shape with the microlayer, while the black line shows the bubble shape without the microlayer. (Top) Bubble shapes at time $t = 4.0$. (Bottom) Bubble shapes at time $t = 5.0$	119
Figure 5.11: (Top). The Nusselt number variation over time at wall superheat of 2. The dashed lines are the simulations with the microlayer included. (Bottom). Nusselt number variation over time at wall superheat of 3.	120
Figure 6.1: Schematic of the linear concentration profile.....	143
Figure 6.2: Schematic of the quadratic profile.....	144
Figure 6.3: Schematic of the bi-linear concentration profile	145
Figure 6.4: Schematic of the exponential profile.....	146
Figure 6.5 Time evolution of the concentration profile using finite difference methods, grid resolution = 1000 pts	147
Figure 6.6: Steady state convergence of the finite difference method in solving the species transport equation	148
Figure 6.7: Steady state comparison of the linear model and the finite difference method.....	149
Figure 6.8: Steady state comparison of the quadratic model and the finite difference method.....	150
Figure 6.9: Steady state comparison of the bi-linear model and the finite difference method.....	151
Figure 6.10: Steady state comparison of the exponential model and the finite difference method	152
Figure 6.11: Comparison of the models with the full simulations if the diffusion coefficient is reduced to 0.01. The models are plotted only at the lowest working resolution. At all resolutions above it, the models are accurate.....	153
Figure 6.12: Comparison of the models with the full simulations if the diffusion coefficient is reduced to 0.005. The models are plotted only at the lowest working resolution. At all resolutions above it, the models are accurate.....	154
Figure 6.13: Comparison of the models with the full simulations if the velocity is doubled to 2. The models are plotted only at the lowest working resolution. At all resolutions above it, the models are accurate.....	155

Figure 6.14: Comparison of the models with the full simulations if the velocity is tripled to 3. The models are plotted only at the lowest working resolution. At all resolutions above it, the models are accurate..... 156

Figure 6.15: Comparison of the models with the full simulations if the velocity is quadrupled to 4. The quadratic model is plotted only at the lowest working resolution. At all resolutions above it, the model is accurate. 157

LIST OF TABLES

Table 3-1 Constant parameters. All dimensions except the non-dimensional film thickness are in computational units.	68
Table 3-2 Simulation parameters. The viscosity values are in computational units.	69
Table 6-1: Grid resolution for the full simulations at $U = 1$, $D = 0.05$	158
Table 6-2: Grid resolution test for the linear model at $U = 1$, $D = 0.05$	159
Table 6-3: Grid resolution test for the quadratic model at $U = 1$, $D = 0.05$	160
Table 6-4: Grid resolution tests for the bi-linear model at $U = 1$, $D = 0.05$	161
Table 6-5: Grid resolution tests for the exponential model. The slope is the inclination in the first grid interval where the exponential model is applied.	162

CHAPTER 1

-

INTRODUCTION

“The purpose of computing is insight.” - R.W. Hamming

Numerical simulations augment our ability to reason. Scarcely an application exists in modern science untouched by the influence of computing. More than just a supplementary tool to theoretical formulations and experimental observations, numerical simulations can be used to gain insight into certain intricate processes and phenomena where the other methodologies might not be able to yield satisfactory explanations.

Numerous examples can be cited where computers help us gain insight by enabling us to include (as well as progressively increase) complexity in models that might have been otherwise unresolved, helping us understand phenomena that is difficult to observe experimentally, and empowering us to test theories at much lesser expense. Buzbee (1984) has illustrated this fact in a brief article citing three very different examples of the insight gained from computing; determining the equation of state of one-component plasma, the impact of potential accidents in a nuclear reactor, and the synergy between analysis and simulations in the advancement of the theory of nonlinear analysis.

1.1 Motivation

1.1.1 Numerical simulations of multiphase flows

Generally, when we speak of multiphase flows in the science and engineering, the reference is to systems where there is a sizeable difference in scale between the entities under consideration like raindrops falling through air into the soil, aerosols dispersed in a surrounding medium, the flow of bubbles in water and many more. Although there are many multiphase fluid systems where the continuum scales are of the same order like jet flows, oceanic currents etc., much of the interest is in the study of systems which have a disparity in the length scales.

Examples of multiphase flows are plentiful. They include atomization and sprays, reactive bubbly flows, boiling, and several other industrial applications and in nature. Today, when energy conservation and sustainable development are not merely buzzwords, multiphase flows have assumed even greater significance. In this thesis, nucleate boiling, impact of drops and convective mass transfer have applications in heat transfer and energy conversion, internal combustion engines and mixing of fuels respectively. Understanding and predicting the behavior of multiphase fluid systems is critical not only because of current applications, but also because of a variety of future technologies.

There are many numerical methods that can be used to simulate multiphase flows accurately and quickly. Many of them have much in common. The two fluids are separated by an interface, with a suitable marker function used to distinguish the

fluids. The governing equations are solved for the entire domain and not separately for each fluid, and the interface jump conditions are implicitly included. The crucial difference in the methods lies in how the interface is moved as time progresses.

One of the earliest numerical studies of multiphase flows was done by Harlow and Welch (1965), who developed the Marker-and-Cell (MAC) method to capture the impact of droplets on thin liquid films and other applications. The lack of computing power in the sixties meant that some of the assumptions made about the fluid flow were inaccurate, but the method that they provided proved to be seminal. The Volume-of-Fluid (VOF) method developed by Hirt and Nichols (1981) is also a fixed grid method like the MAC method and is very popular. Fixed grids are extremely efficient because of their simple structure and with minor modifications, they can adapt to a variety of complex geometries and flow scenarios. The front tracking method introduced by Unverdi and Tryggvason (1992) which is the numerical technique used in this dissertation, uses the MAC method in the grid structure and an explicit method to account for the fluid interface. Other prominent fixed grid methods include the continuous surface force (CSF) method, developed by Brackbill et al. (1992) to compute surface tension in VOF methods, the level set method of Osher and Sethian (1988), Jacqmin's phase field method (1999), and the cubic interpolated pseudo-particle (CIP) method by Takewaki, Nishiguchi and Yabe (1985) for solving hyperbolic-type equations.

Besides fixed grid methods, there are the boundary integral methods that can be used for special types of flows. Those include Lounget-Higgins and Cokelet (1976) for inviscid free surface flows, and by Youngren and Acrivos (1975) for Stokes flow

past a particle. Other approaches include the body-fitted grid method of Ryskin and Leal (1984) for intermediate Reynolds numbers.

1.1.2 Multiscale modeling of multiphase flows

The challenge for the future is to explore more complex physics and to make the computations faster, more efficient and more accurate. Although several examples of multiscale modeling in multiphase flows exist, the focus of this dissertation is narrowed to three wide-ranging applications. The impact of a droplet on a thin liquid film, the effect of the microlayer on nucleate boiling and mass transfer from a rising bubble, all provide the challenge to accurately predict the flow both at the sub-grid level and the large-scale level. We briefly discuss these three phenomena below.

For a wide range of engineering applications, incorporating phase change is essential. Heat transfer by boiling is generally superior to other means of heat transfer because of the latent heat present. A liquid at saturation temperature and pressure can absorb heat from heated wall without a significant rise in temperature, as the heat energy is utilized in the change of phase. A comprehensive understanding of the phase change process is needed. The challenge is to incorporate both the “large-scale” phenomenon of phase change and the “small-scale” effect of the microlayer in nucleate boiling.

The impact of a drop on a thin liquid film presents a unique challenge in tying together the large-scale kinetics of the drop and the small-scale effects of the thin film of liquid or air that is squeezed out when the drops impacts, on the overall splash

morphology. In mass transfer, we investigate how the overall transfer of specie from one fluid to the other is influenced by the sub-grid concentration boundary layer.

1.2 Scope of the present work

As mentioned earlier, the purpose of computing is to gain insight in processes and phenomena where direct observations or established analytical solutions may not be applicable. The focus in the present study is on obtaining a deeper understanding of multiphase flow scenarios where it is vital to capture intricate features or small-scale behavior using direct numerical simulations and such details are not forthcoming experimentally or where the small scales cannot be resolved. The flow situations that we have looked at are droplet impact, nucleate boiling and convective mass transfer. All these flows have multitudes of practical applications. Droplet impact helps us in understanding the erosion of soil during rainfall. Impact of drops has applications industry, namely, in internal combustion engines, spray coating and ink-jet printing. Nucleate boiling has been recognized as a very efficient mode of heat transfer. Hence, it is widely used in cooling of energy generation systems in space-crafts and industries, in electronic cooling, metal processing and several others. The principle of convective mass transfer is the backbone of industrial chemical reactions and also in studying the dispersal of pollutants in the atmosphere etc.

What unites these disparate flows is the indispensable role of thin films in obtaining a complete understanding of the physical phenomenon. For example, when a drop of liquid falls on a solid substance, very close to the wall, a film of vapor or air is pushed outwards at the time of impact. This thin film of air is usually of the order

of a few hundred Angstroms, and is very difficult to observe experimentally. Although the time-scale and the length scale of this phenomenon are very small, the effect of the thin film on the splashing of the droplet cannot be neglected. In the case of nucleate boiling, the greater the amount of saturated liquid present, the greater the amount of heat transfer and hence, greater cooling. The microlayer is a thin film of liquid at the base of a nucleating vapor bubble that cannot be seen or measured easily. Most of the estimates in the literature seem to converge at 1 – 5 microns. The presence of the microlayer augments the heat transfer significantly. Convective mass transfer is the movement of species from one fluid to another. When a gas bubble rises in a liquid moving with a definite velocity, there is mass transference across the liquid-gas interface. Most of this motion of species occurs close to the interface, while far away from the interface the concentration remains unchanged. The thin film region around the interface acts like a boundary layer, where the actual evolution of the concentration takes place. Thus, in all the three applications, the thin film plays a central role in our understanding the physical process.

There are two broad approaches to capture the effect of thin films: One is to refine the computational domain by adding in more grid points, or to use a coarser grid and to replicate the thin film by the means of a suitable model. In certain portions of the flow, to exactly simulate the thin films, the grid has to be resolved to such an extent that is computationally impractical to do it just by direct numerical simulations. So for each application, a sub-grid mathematical model has been developed for the thin films to be coupled with the “large-scale” continuum fluid equations for the rest of the domain to accurately predict the physical phenomenon.

It has been the motivation of this work to show that regardless of the type of flow, or composition of the film, the small-scale behavior is universal in nature and though the formulation might vary slightly, the principles are innate. The goal behind the research is to develop a mathematical framework on which the evolution of thin films in multiphase flows can be described correctly.

CHAPTER 2

-

FORMULATION AND NUMERICAL METHOD

2.1 The front-tracking method

The earliest application to solve multiphase flow problems by using a sharp interface to separate two immiscible fluids was to study the two-fluid Rayleigh-Taylor instability. As mentioned in the previous section, the marker and cell (MAC) method used by Harlow and Welch used a fixed, staggered grid that is still widely used and uniformly distributed marker particles to identify each fluid. The difficulty in advecting the interface separating the two fluids can be resolved by using connected marker particles to mark the fluid interface. The challenges with this approach are two-fold; keep the front resolution uniform and generate a marker function from the front location. The advantages of the method include the ability to track even small interfaces and capture the interface in greater detail. In the front tracking method introduced by Unverdi and Tryggvason (1992), the Navier-Stokes equations are solved by a second-order accurate projection method, using centered-differences on a fixed, staggered grid and the phase boundary is tracked by connected marker points (the "front"). The front points are advected by the flow velocity, interpolated from the fixed grid. As the front deforms, surface elements are dynamically added and deleted. The surface tension is represented by a distribution of singularities (delta-functions) located at the front. The gradients of the density and viscosity become delta-functions

when the change is abrupt across the boundary. At each time step, after the front has been advected, the density and the viscosity fields are reconstructed by integration of the smooth grid-delta function. The surface tension is then added to the nodal values of the discrete Navier-Stokes equations. Finally, an elliptic pressure equation is solved by the successive-over-relaxation (SOR) method, or other more efficient iteration methods described by Greenbaum (1996) in order to impose a divergence-free velocity field. A detailed discussion of the SOR method is provided in the following section.

The front-tracking method has been applied to several multi-fluid problems and tested and validated in a number of ways. Those tests include comparisons with analytical solutions for simple problems, other numerical computations, and experiments. The actual resolution requirement varies with the parameters of the problem. High Reynolds numbers flows, for example, generally require finer resolution than low Reynolds number flows, as in other numerical calculations. However, in all cases the method converges rapidly under grid refinement, and in those cases where we have explicit solutions we have found excellent agreement, even for modest resolutions. A few examples of these validations are provided by Tryggvason et al. (2001), Esmaeeli and Tryggvason (1998 and 1999), Bunner and Tryggvason (2002), and Lu, Fernandez and Tryggvason (2005).

2.2 Governing Equations

Consider a mass of one fluid moving in another quiescent fluid. It could either be a drop of liquid falling in air, or bubble of vapor or air rising in a liquid. In both these

cases, the fluids are taken to be Newtonian fluids, which are denoted by viscosity μ_a for viscosity of air, μ_v for viscosity of vapor and μ_l for liquid. The densities for each phase are ρ_a, ρ_v , and ρ_l for the air bubble, vapor and liquid respectively. The interface separating the two interfaces is characterized by a surface tension σ . The fluids are assumed to be immiscible and free of surface contaminants; hence the surface tension remains constant over time.

Knowing all the fluid properties and including the assumptions made above, the fluid motion can be described by the Navier-Stokes equations. In the conservative form, it can be written as

$$\frac{\partial \rho \mathbf{u}}{\partial t} + \nabla \cdot \rho \mathbf{u} \mathbf{u} = -\nabla p + \rho \mathbf{g} + \nabla \cdot \mu (\nabla \mathbf{u} + \nabla \mathbf{u}^T) + \int_{A(t)} \sigma \kappa \mathbf{n} \delta(\mathbf{x} - \mathbf{x}_f) dA \quad (2.1)$$

This single equation describes the motion of both the fluids under consideration, viz. the fluid inside the bubble/drop and the quiescent fluid outside. Although the viscosity and the density of the gas phase are much smaller than the liquid phase, it cannot be neglected. Thus, in order to understand the flow pattern in the whole domain, the full Navier-Stokes equation must be solved for the flow both outside and inside the drop/bubble.

In the above equation, \mathbf{u} , \mathbf{g} , and \mathbf{x} are the vector quantities, \mathbf{n} is the unit normal vector and p , μ , ρ and σ are the scalar quantities. Now \mathbf{u} is the velocity, $\rho \mathbf{g}$ is the gravity force, \mathbf{x} is the position vector, \mathbf{x}_f is the position of interface, p is the pressure,

ρ is the density, μ is the viscosity, σ is the surface tension, κ is the curvature and δ is a delta function.

One word about the surface tension term. The surface tension force at the interface are treated as a body force acting only on the interface, which is indicated by the integral of a delta function over a surface element, dA .

In addition to the momentum equation (2.1), the fluid properties are described by the equations of state. For the range of motions under considerations, the pressure difference is small enough that the volume of the bubble will not change. The fluids are assumed to be incompressible and also, the fluids are considered to be immiscible, hence the densities and viscosities remain constant with each fluid.

$$\frac{\partial \rho}{\partial t} + \nabla \cdot \mathbf{u} \rho = 0. \quad (2.2)$$

$$\frac{\partial \mu}{\partial t} + \nabla \cdot \mathbf{u} \mu = 0. \quad (2.3)$$

The equation of state for the density reduces the mass conservation equation to

$$\nabla \cdot \mathbf{u} = 0. \quad (2.4)$$

The code developed for the entire set of simulations in this dissertation is an axisymmetric version of the momentum and mass conservations equations. This code runs much faster than the fully three dimensional versions, meaning that more runs and higher resolution can be accomplished. The domain is sketched in Figure 2.1. The domain is axisymmetric and the left boundary is the axis of symmetry. The equation of motion is solved over the entire domain, inside as well as the outside the drop/bubble.

$$\begin{aligned}
\frac{\partial \rho u}{\partial t} + \frac{1}{r} \frac{\partial r \rho u^2}{\partial r} + \frac{\partial \rho v u}{\partial z} &= - \frac{\partial p}{\partial r} \\
+ \frac{\partial}{\partial r} \left(2\mu \frac{\partial u}{\partial r} \right) + 2\mu \frac{\partial}{\partial r} \left(\frac{u}{r} \right) + \frac{\partial}{\partial r} \mu \left(\frac{\partial u}{\partial r} + \frac{\partial u}{\partial z} \right) & \\
- \int_S \sigma \kappa \bar{n} \delta(x - x_f) \cdot \hat{i}_r dS + f_r &
\end{aligned} \tag{2.5}$$

$$\begin{aligned}
\frac{\partial \rho v}{\partial t} + \frac{1}{r} \frac{\partial r \rho v u}{\partial r} + \frac{\partial \rho v^2}{\partial z} &= - \frac{\partial p}{\partial z} \\
+ \frac{1}{r} \frac{\partial}{\partial r} \mu r \left(\frac{\partial v}{\partial r} + \frac{\partial u}{\partial z} \right) + \frac{\partial}{\partial z} \left(2\mu \frac{\partial v}{\partial z} \right) & \\
- \int_S \sigma \kappa \bar{n} \delta(x - x_f) \cdot \hat{i}_z dS + f_z &
\end{aligned} \tag{2.6}$$

Here, u and v are the velocity components in the radial and axial directions respectively, and \hat{i}_r and \hat{i}_z are the radial and axial components of the surface normal pointing outwards from the drop. All the other variables have the same meaning as described in equation (2.1). The mass conservation equation transforms to

$$\frac{1}{r} \frac{\partial r u}{\partial r} + \frac{\partial v}{\partial z} = 0 . \tag{2.7}$$

On combining (2.5), (2.6) and (2.7), we get a Poisson-type equation for the pressure term,

$$\nabla \cdot \left(\frac{1}{\rho} \right) \nabla p = R . \tag{2.8}$$

where R is the divergence of the vector form of the momentum and mass conservation equations, excluding the pressure term and divided by the density.

2.3 Time Integration

The momentum and mass equations at each time step are written as,

$$\frac{\rho^{n+1} \mathbf{u}^{n+1} - \rho^n \mathbf{u}^n}{\Delta t} = -A_h(\mathbf{u}^n, \rho^n, \mu^n) - \nabla_h p. \quad (2.9)$$

$$\nabla_h \cdot \mathbf{u}^{n+1} = 0. \quad (2.70)$$

The subscript h suggests a finite difference approximation and the superscripts n and $n+1$ denotes the current time-step and the next time-step respectively.

The momentum equation is separated into two parts,

$$\frac{\rho^{n+1} \mathbf{u}^* - \rho^n \mathbf{u}^n}{\Delta t} = -A_h(\mathbf{u}^n, \rho^n, \mu^n). \quad (2.11)$$

and

$$\frac{\rho^{n+1} \mathbf{u}^{n+1} - \rho^{n+1} \mathbf{u}^*}{\Delta t} = -\nabla_h p. \quad (2.12)$$

The projected velocity, \mathbf{u}^* calculates the velocity at the next time step without taking into account the effect of the pressure. This projected velocity can be calculated from (2.11) as

$$\mathbf{u}^* = \frac{1}{\rho^{n+1}} \left\{ \rho^n \mathbf{u}^n - \Delta t A_h(\mathbf{u}^n, \rho^n, \mu^n) \right\}. \quad (2.13)$$

We take the divergence of \mathbf{u}^{n+1} , which provide us with the incompressibility condition (2.10). Using (2.10) and (2.12), we get an expression for p

$$\nabla_h \cdot \left(\frac{\nabla_h p}{\rho^{n+1}} \right) = \frac{1}{\Delta t} \nabla_h \cdot \mathbf{u}^*. \quad (2.14)$$

After the pressure is solved for using successive-over-relaxation, the velocity at the next time-step will be,

$$\mathbf{u}^{n+1} = \mathbf{u}^* - \frac{\Delta t}{\rho^{n+1}} \nabla_h p. \quad (2.15)$$

The simple first order, explicit time discretization cannot be used here as the simulations run for a longer time. For our simulations, a much more accurate time integration method is necessary. Here, we use a modified version of the predictor-corrector scheme. Ordinarily, the predictor-corrector method is a two-step method, but the method that we use is a three-step method developed by Han (1998) in this thesis, which is easier to program. For example, if we have an equation to integrate over time,

$$\frac{dy}{dt} = f(t, y). \quad (2.16)$$

An intermediate step is introduced:

$$\tilde{y}^{n+1} = y^n + \Delta t f(t^n, y^n). \quad (2.17)$$

This intermediate value is then used to calculate the predicted value.

$$\hat{y}^{n+1} = \tilde{y}^{n+1} + \Delta t f(t^{n+1}, \tilde{y}^{n+1}). \quad (2.18)$$

The corrected value is then obtained by using the predicted value and the old value at the previous time-step.

$$y^{n+1} = \frac{1}{2}(y^n + \hat{y}^{n+1}). \quad (2.19)$$

This method provides for second-order accuracy in the time integration.

2.4 Finite Difference Equations and Boundary Conditions

The computational grid used in solving the equation is a staggered grid, as sketched in Figure 2.2. The staggered grid is based on the Marker and Cell method of Harlow

and his collaborators at Los Alamos. The primary benefits of the staggered grid are the efficient coupling of the variables, and better stability.

The spacing between the grid points in both the directions is not kept uniform. The reasoning behind it is two-fold. One is that the unequal spacing means the computational resources can be utilized more efficiently by placing more grid points near the region of interest. The second reason is that the accuracy of the computations can be improved by refocusing the distribution of the grid points. A template for the non-uniform grid spacing is shown in Figure 2.3. In our calculations, the physical non-uniform grid coordinates r and z are transformed into the computational uniform grid coordinates ξ and η respectively. The transformations of the derivatives from r to ξ are:

$$\frac{\partial}{\partial r} = \frac{1}{r_\xi} \frac{\partial}{\partial \xi} . \quad (2.20)$$

$$\frac{\partial}{\partial r} f \frac{\partial}{\partial r} = \frac{1}{r_\xi} \frac{\partial}{\partial \xi} \left(f \frac{1}{r_\xi} \frac{\partial}{\partial \xi} \right) . \quad (2.21)$$

where,

$$r_\xi = \frac{\partial r}{\partial \xi} . \quad (2.22)$$

In stretched grids, we have the liberty to set the grid spacing for the transformed coordinates. The grid spacing is set as 1 in the computational domain.

$$\Delta \xi = 1. \quad (2.23)$$

In a similar vein, the transformation from z to η can be achieved. The momentum and mass equations are discretized by a conservative, second order centered

difference scheme, and the time integration is done by the modified predictor-corrector method described earlier.

The discrete forms of the projected velocity equation are:

$$\frac{1}{\Delta t} \left\{ \left(\frac{\rho_{i+1,j}^{n+1} + \rho_{i,j}^{n+1}}{2} \right) u_{i+1/2,j}^* - \left(\frac{\rho_{i+1,j}^n + \rho_{i,j}^n}{2} \right) u_{i+1/2,j}^n \right\} = A_{i+1/2,j}^n \quad (2.24)$$

$$\frac{1}{\Delta t} \left\{ \left(\frac{\rho_{i,j+1}^{n+1} + \rho_{i,j}^{n+1}}{2} \right) v_{i,j+1/2}^* - \left(\frac{\rho_{i,j+1}^n + \rho_{i,j}^n}{2} \right) v_{i,j+1/2}^n \right\} = B_{i,j+1/2}^n \quad (2.25)$$

where

$$\begin{aligned} A_{i+1/2,j}^n = & \frac{-1}{r_{i+1/2} r_{\xi_{i+1/2}}} \left\{ r_{i+1} \rho_{i+1,j}^n \left(\frac{u_{i+3/2,j}^n + u_{i+1/2,j}^n}{2} \right)^2 - r_i \rho_{i,j}^n \left(\frac{u_{i+1/2,j}^n + u_{i-1/2,j}^n}{2} \right)^2 \right\} \\ & - \frac{1}{z_{\eta_j}} \left\{ \left(\frac{\rho_{i+1,j}^n + \rho_{i+1,j+1}^n + \rho_{i,j+1}^n + \rho_{i,j}^n}{4} \right) \left(\frac{u_{i+1/2,j+1}^n + u_{i+1/2,j}^n}{2} \right) \left(\frac{v_{i+1,j+1/2}^n + v_{i,j+1/2}^n}{2} \right) \right. \\ & \left. - \left(\frac{\rho_{i+1,j-1}^n + \rho_{i+1,j}^n + \rho_{i,j}^n + \rho_{i,j-1}^n}{4} \right) \left(\frac{u_{i+1/2,j}^n + u_{i+1/2,j-1}^n}{2} \right) \left(\frac{v_{i+1,j-1/2}^n + v_{i,j-1/2}^n}{2} \right) \right\} \\ & + (f_r)_{i+1/2,j} \\ & + \frac{1}{r_{\xi_{i+1/2}}} \left\{ 2\mu_{i+1,j}^n \left(\frac{u_{i+3/2,j}^n - u_{i+1/2,j}^n}{r_{\xi_{i+1}}} \right) - 2\mu_{i,j}^n \left(\frac{u_{i+1/2,j}^n - u_{i-1/2,j}^n}{r_{\xi_i}} \right) \right\} \\ & + 2 \left(\frac{\mu_{i+1,j}^n + \mu_{i,j}^n}{2} \right) \frac{1}{r_{\xi_{i+1/2}}} \left\{ \left(\frac{u_{i+3/2,j}^n - u_{i+1/2,j}^n}{2r_{i+1}} \right) - \left(\frac{u_{i+1/2,j}^n - u_{i-1/2,j}^n}{2r_i} \right) \right\} \\ & \left\{ \left(\frac{\mu_{i+1,j}^n + \mu_{i+1,j+1}^n + \mu_{i,j}^n + \mu_{i,j+1}^n}{4} \right) \left(\frac{u_{i+1/2,j+1}^n - u_{i+1/2,j}^n}{z_{\eta_{j+1/2}}} + \frac{v_{i+1,j+1/2}^n - v_{i,j+1/2}^n}{r_{\xi_{i+1/2}}} \right) \right. \\ & \left. - \left(\frac{\mu_{i+1,j-1}^n + \mu_{i+1,j}^n + \mu_{i,j-1}^n + \mu_{i,j}^n}{4} \right) \left(\frac{u_{i+1/2,j}^n - u_{i+1/2,j-1}^n}{z_{\eta_{j-1/2}}} + \frac{v_{i+1,j-1/2}^n - v_{i,j-1/2}^n}{r_{\xi_{i+1/2}}} \right) \right\} \end{aligned} \quad (2.26)$$

and ,

$$\begin{aligned}
B_{i+,j+1/2}^n = & \frac{-1}{r_i r_{\xi_i}^{\xi_i}} \left\{ \begin{aligned} & r_{i+1/2} \left(\frac{\rho_{i+1,j}^n + \rho_{i+1,j+1}^n + \rho_{i,j+1}^n + \rho_{i,j}^n}{4} \right) \left(\frac{u_{i+1/2,j+1}^n + u_{i+1/2,j}^n}{2} \right) \left(\frac{v_{i+1,j+1/2}^n + v_{i,j+1/2}^n}{2} \right) \\ & - r_{i-1/2} \left(\frac{\rho_{i,j}^n + \rho_{i,j+1}^n + \rho_{i-1,j+1}^n + \rho_{i-1,j}^n}{4} \right) \left(\frac{u_{i-1/2,j}^n + u_{i-1/2,j+1}^n}{2} \right) \left(\frac{v_{i,j+1/2}^n + v_{i-1,j+1/2}^n}{2} \right) \end{aligned} \right\} \\
& - \frac{1}{z_{\eta_{j+1/2}}} \left\{ \rho_{j+1}^n \left(\frac{v_{i,j+3/2}^n + v_{i,j+1/2}^n}{2} \right)^2 - \rho_j^n \left(\frac{v_{i,j+1/2}^n + v_{i,j-1/2}^n}{2} \right)^2 \right\} \\
& + (f_z)_{i,j+1/2} \\
& + \frac{1}{r_i r_{\xi_{i+1/2}}^{\xi_{i+1/2}}} \left\{ \begin{aligned} & \left(\frac{\mu_{i+1,j}^n + \mu_{i+1,j+1}^n + \mu_{i,j}^n + \mu_{i,j+1}^n}{4} \right) r_{i+1/2} \\ & \left(\frac{u_{i+1/2,j+1}^n - u_{i+1/2,j}^n}{z_{\eta_{j+1/2}}} + \frac{v_{i+1,j+1/2}^n - v_{i,j+1/2}^n}{r_{\xi_{i+1/2}}^{\xi_{i+1/2}}} \right) \\ & - \left(\frac{\mu_{i,j}^n + \mu_{i,j+1}^n + \mu_{i-1,j}^n + \mu_{i-1,j+1}^n}{4} \right) r_{i-1/2} \\ & \left(\frac{u_{i-1/2,j+1}^n - u_{i-1/2,j}^n}{z_{\eta_{j+1/2}}} + \frac{v_{i,j+1/2}^n - v_{i-1,j+1/2}^n}{r_{\xi_{i+1/2}}^{\xi_{i+1/2}}} \right) \end{aligned} \right\} \\
& + \frac{1}{z_{\eta_{j+1/2}}} \left\{ 2\mu_{i,j+1}^n \left(\frac{v_{i,j+3/2}^n - v_{i,j+1/2}^n}{z_{\eta_{j+1}}} \right) - 2\mu_{i,j}^n \left(\frac{v_{i,j+1/2}^n - v_{i,j-1/2}^n}{z_{\eta_j}} \right) \right\}
\end{aligned} \tag{2.27}$$

The mass conservation equation written at (2.12) will be,

$$\frac{1}{r_i r_{\xi_i}^{\xi_i}} \left(r_{i+1/2} u_{i+1/2,j}^{n+1} - r_{i-1/2} u_{i-1/2,j}^{n+1} \right) + \frac{1}{z_{\eta_j}} \left(v_{i,j+1/2}^{n+1} - v_{i,j-1/2}^{n+1} \right) = 0 . \tag{2.8}$$

Using the relationship established in (2.29), the pressure is solved with the equation:

$$\begin{aligned}
& \frac{1}{r_i r_{\xi_i}} \left(\frac{r_{i+1/2} P_{i+1,j}^{n+1}}{\rho_{i+1/2,j}^{n+1} r_{\xi_{i+1/2}}} + \frac{r_{i-1/2} P_{i-1,j}^{n+1}}{\rho_{i-1/2,j}^{n+1} r_{\xi_{i-1/2}}} \right) + \frac{1}{z_{\eta_j}} \left(\frac{P_{i,j+1}^{n+1}}{\rho_{i,j+1/2}^{n+1} z_{\eta_{j+1/2}}} + \frac{P_{i,j-1}^{n+1}}{\rho_{i,j-1/2}^{n+1} z_{\eta_{j-1/2}}} \right) \\
& - \left\{ \frac{1}{r_i r_{\xi_i}} \left(\frac{r_{i+1/2}}{\rho_{i+1/2,j}^{n+1} r_{\xi_{i+1/2}}} + \frac{r_{i-1/2}}{\rho_{i-1/2,j}^{n+1} r_{\xi_{i-1/2}}} \right) + \frac{1}{z_{\eta_j}} \left(\frac{1}{\rho_{i,j+1/2}^{n+1} z_{\eta_{j+1/2}}} + \frac{1}{\rho_{i,j-1/2}^{n+1} z_{\eta_{j-1/2}}} \right) \right\} P_{i,j}^{n+1} \\
& = \frac{1}{\Delta t} \left\{ \frac{1}{r_i r_{\xi_i}} (r_{i+1/2} u_{i+1/2,j}^* - r_{i-1/2} u_{i-1/2,j}^*) + \frac{1}{z_{\eta_j}} (v_{i,j+1/2}^* - v_{i,j-1/2}^*) \right\}
\end{aligned} \tag{2.30}$$

The pressure equation is solved by SOR and then the velocities are updated by:

$$u_{i+1/2,j}^{n+1} = u_{i+1/2,j}^* - \frac{\Delta t}{\rho_{i+1/2,j}^{n+1} r_{\xi_{i+1/2}}} \frac{1}{r_{\xi_i}} (p_{i+1,j}^{n+1} - p_{i,j}^{n+1}). \tag{2.31}$$

$$v_{i,j+1/2}^{n+1} = v_{i,j+1/2}^* - \frac{\Delta t}{\rho_{i,j+1/2}^{n+1} z_{\eta_{j+1/2}}} \frac{1}{z_{\eta_j}} (p_{i,j+1}^{n+1} - p_{i,j}^{n+1}). \tag{2.32}$$

In order that the computations run smoothly over long periods, the time step should be selected judiciously so that it meets the stability limits. There are two limits that determine the maximum time step. First is the viscous or diffusive time step:

$$\frac{s_{\max} \Delta t}{h_{\min}^2} \leq \frac{1}{4} \tag{2.33}$$

where

s_{\max} is the largest value of the diffusion coefficient $\nu = \mu / \rho$, and h_{\min} is the smallest grid size in either axes. The second is the advection time step:

$$\frac{\left(|u|^2 + |v|^2 \right)_{\max} \Delta t}{s_{\min}} \leq 2, \tag{2.34}$$

where s_{\min} is the largest value of the diffusion coefficient $\nu = \mu / \rho$.

The equations mentioned above undergo a modification when we deal with the boundaries. At the left boundary as shown in Figure 2.4, it is clear that the horizontal velocity is zero.

$$u_{i-1/2,j} = 0. \quad (2.35)$$

The staggered mesh simplifies the treatment of the pressure boundary condition; the velocity boundary condition becomes slightly complicated, depending on the wall conditions. If the boundary is full slip, the velocity at the boundary becomes,

$$v_{i-1,j+1/2} = v_{i,j+1/2}. \quad (2.9)$$

If the boundary is non-slip, the condition is,

$$v_{i-1,j+1/2} = -v_{i,j+1/2}. \quad (2.37)$$

2.5 The Front-Tracking Method

The density field separates the two fluids, and the equation for updating the density field over time is given by,

$$\frac{\partial \rho}{\partial t} + \nabla \cdot \mathbf{u} \rho = 0. \quad (2.38)$$

The density field is discontinuous at the interface, and the discontinuity is maintained by the presence of the separate computational points. These points combining to form the “front” represent the interface. The front is advected at every time step based on the velocity field on the grid, and based on the position of the front, the density field is constructed. In our code, the velocity from the grid is transferred to a point on the front through a method called area-weighting. From

Figure 2.5, it can be seen that the velocity of a front is obtained from interpolating the velocities from the corner points of the grid cell. The formula for interpolating from the grid to the front takes the form of,

$$\phi_p = \sum \phi_{ij} w_{ij} \quad (2.39)$$

where ϕ_p is the value of a variable on the front, ϕ_{ij} is the value of a variable on the grid and w_{ij} is the weighting function. The weighting function is the product of two delta functions in the case of two-dimensional scenarios.

$$w_{ij}(x_p) = d(x_p - ih) d(y_p - jh) \quad (2.40)$$

In area weighting the delta function is,

$$d(r) = \begin{cases} (r - ih)/h & 0 < r < h \\ (h - (r - ih))/h & -h < r < 0 \\ 0 & |r| \geq h \end{cases} \quad (2.41)$$

Utilizing (2.40), (2.41) and (2.42), the expression for the interpolated front value is,

$$\phi_p = A_1 \phi_{i,j} + A_2 \phi_{i+1,j} + A_3 \phi_{i+1,j+1} + A_4 \phi_{i,j+1} \quad (2.42)$$

where A_1 , A_2 , A_3 , and A_4 are explained in Figure 2.6.

The points on the front are connected by means of elements. Each element has two points, one at each end and two neighboring elements. As shown in Figure 2.7, the element B has two end points, points 2 and 3. The element B is between elements A and C. The points (1, 2, 3 and 4) are moved at every time step according to the velocity field in the grid by using the equation (2.42). In a programming sense, we keep an account of the elements, their neighboring elements, the points at ends of each element as well as location of each point on the grid.

A vital parameter to compute accurately in our code is the surface tension over the axisymmetric curvature. From Figure 2.8, the volume of an element in axisymmetric curvature is,

$$\Delta V = \Delta z \Delta r r \Delta \theta \quad (2.43)$$

To substitute suitably in the momentum equations (2.5) and (2.6), the quantity needed is the surface tension force per unit volume, i.e. $\Delta F / \Delta V$. To compute the force on the surface element as shown in Figure 2.9, a relationship developed by Weatherburn (1927) is used. The tangent vector \bar{t} is calculated at the end points of each element, as shown in Figure 2.7.

$$\Delta F = \oint \sigma \bar{m} ds \quad (2.44)$$

where \bar{m} is in the surface parallel to the boundary curve. Equation (2.44) can be simplified to

$$\oint \sigma \bar{m} ds \approx \Delta \theta [\Delta(r\sigma\bar{t}) - \sigma\Delta s\bar{t}_r] \quad (2.45)$$

The surface tension force per unit volume can be evaluated as:

$$\frac{\Delta F}{\Delta V} = \frac{\Delta(r\sigma\bar{t}) - \sigma\Delta s\bar{t}_r}{r \Delta z \Delta r} \quad (2.46)$$

For a more detailed discussion on the method, see the paper by Unverdi and Tryggvason (1992).

2.6 Validation of the front-tracking code

Well-tested solutions of the front-tracking code abound in literature. Some of the more prominent ones are mentioned in Chapter 1. Here, the validation of the axisymmetric formulation of the code is presented. In order to check the veracity of our code, a number of tests have been done. The purpose of the tests is to check the

accuracy of the mathematical formulations and numerical implementations. The aim is to test the fluid solver, and the implementation of the interface terms, like surface tension.

Here we test the code by considering the slow viscous flow past a fluid sphere. The system under consideration is a fluid spherical particle of diameter d_e moving relative to a fluid of infinite extent with a steady terminal velocity, U . The Reynolds number is low enough that there is no wake at the rear of the particle. Here, a fluid sphere is considered with its interface taken to be completely devoid of surface contaminants, so that the interfacial tension is held constant. According to Clift, Weber and Grace (1978), for bubbles and drops rising or falling freely in infinite media it is possible to prepare a generalized graphical correlation in terms of the Eötvös Number, Eo ; Morton Number, Mo ; and Reynolds Number Re :

$$Eo = \frac{g \Delta\rho d_e^2}{\sigma}, \quad (2.47)$$

$$M = \frac{g \mu^4 \Delta\rho}{\rho^2 \sigma^3}, \quad (2.48)$$

$$Re = \frac{\rho d_e U}{\mu}. \quad (2.49)$$

where g is the acceleration due to gravity, $\Delta\rho$ is the difference in the density between the fluid particle and the ambient fluid, d_e is the diameter of the fluid particle, σ is the surface tension, μ is the viscosity of the ambient fluid, ρ is density of the ambient fluid and U is the terminal velocity of the fluid particle. For any general case, as can be seen from Figure 2.10, it takes a certain amount of time for the bubble to reach its terminal velocity.

The test case that we have chosen to run is the analytical solution of a particle moving in creeping flow. The solution is called the Hadamard-Rybczynski solution. According to Clift, Weber and Grace (1978), the theoretical terminal velocity, U_T reached by a particle is

$$U_T = \frac{2}{3} \frac{g a^2 \Delta \rho}{\mu} \left(\frac{1 + \kappa}{2 + 3\kappa} \right), \quad (2.50)$$

where a is the radius of the particle, and κ is the ratio of the particle viscosity to the viscosity of the ambient fluid.

We shall consider the case of a lower density particle rising in a higher density fluid. The initial conditions for the flow are: $g = 1.0$, $a = 0.25$, $\Delta \rho = 0.9$, $\mu = 0.063$, and $\kappa = 0.135$. The analytical terminal velocity is calculated to be 0.1984. The rise velocity of the bubble obtained from our code is plotted in Figure 2.11 for two different grid resolutions. The grid spacing for the simulations are $h = 0.0078125$, and 0.0039063 . The steady state rise velocity of our simulations is 0.1962, which is off from the predicted value by about 1.18%. The plot also shows that the grid convergence indicating that a single terminal velocity is approached as the grid size is decreased.

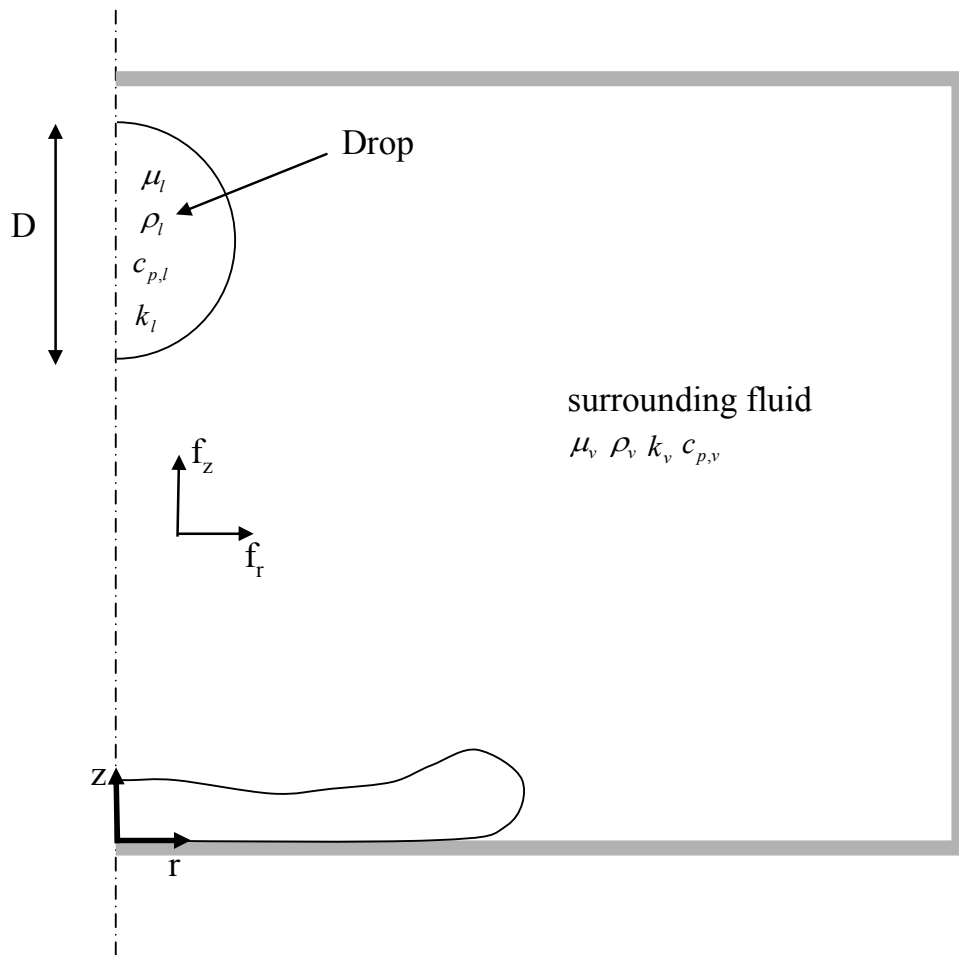


Figure 2.1: Schematic of the computational domain in axisymmetric coordinates.

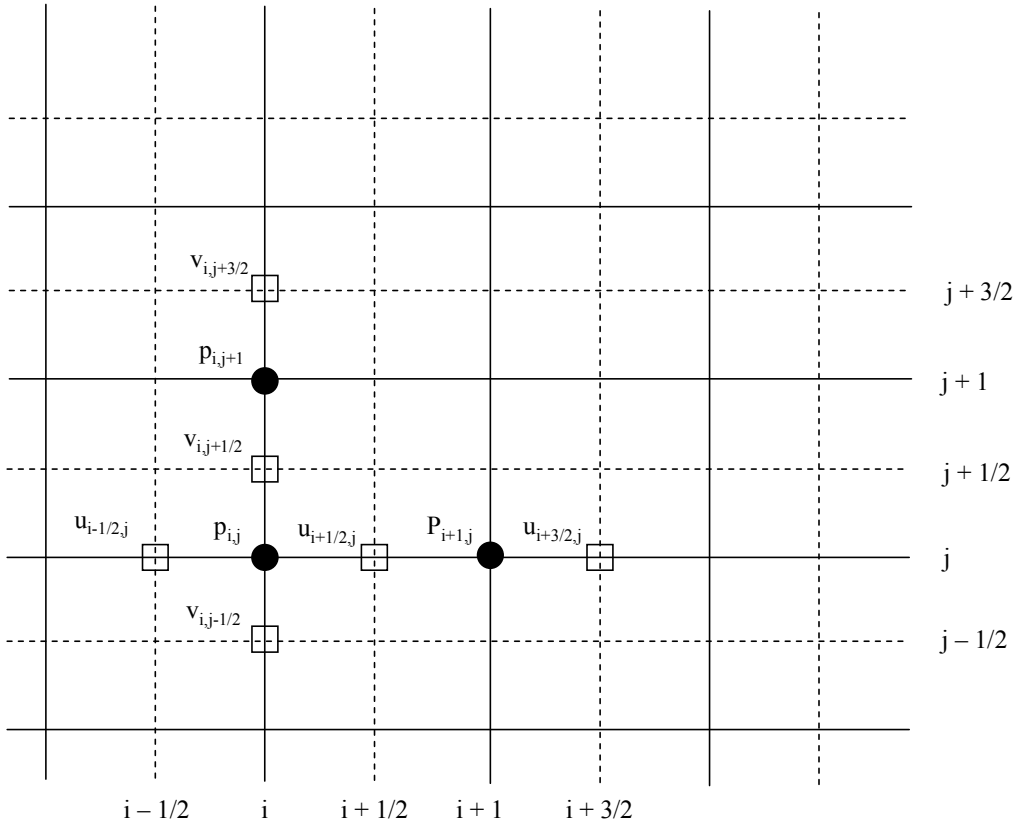


Figure 2.2 : The layout of the staggered grid mesh that is used in the computations. The pressure nodes are located at the center of each cell, and the velocity nodes are the cell faces.

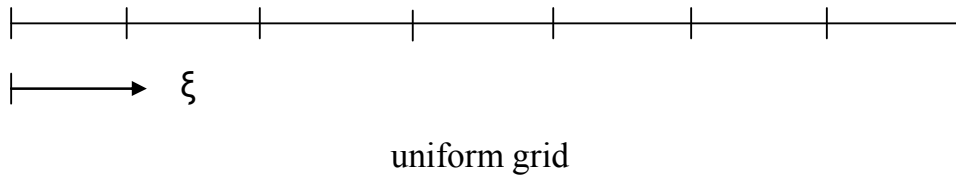
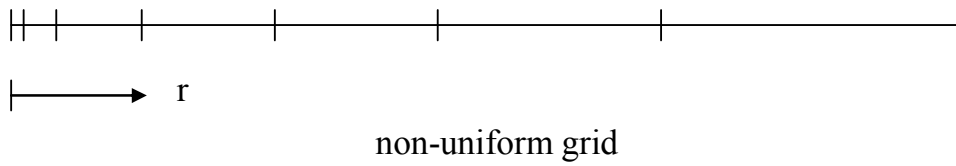


Figure 2.3 : Transformation of the grid. r is the coordinate in the physical domain and ξ is the coordinate the computational domain.

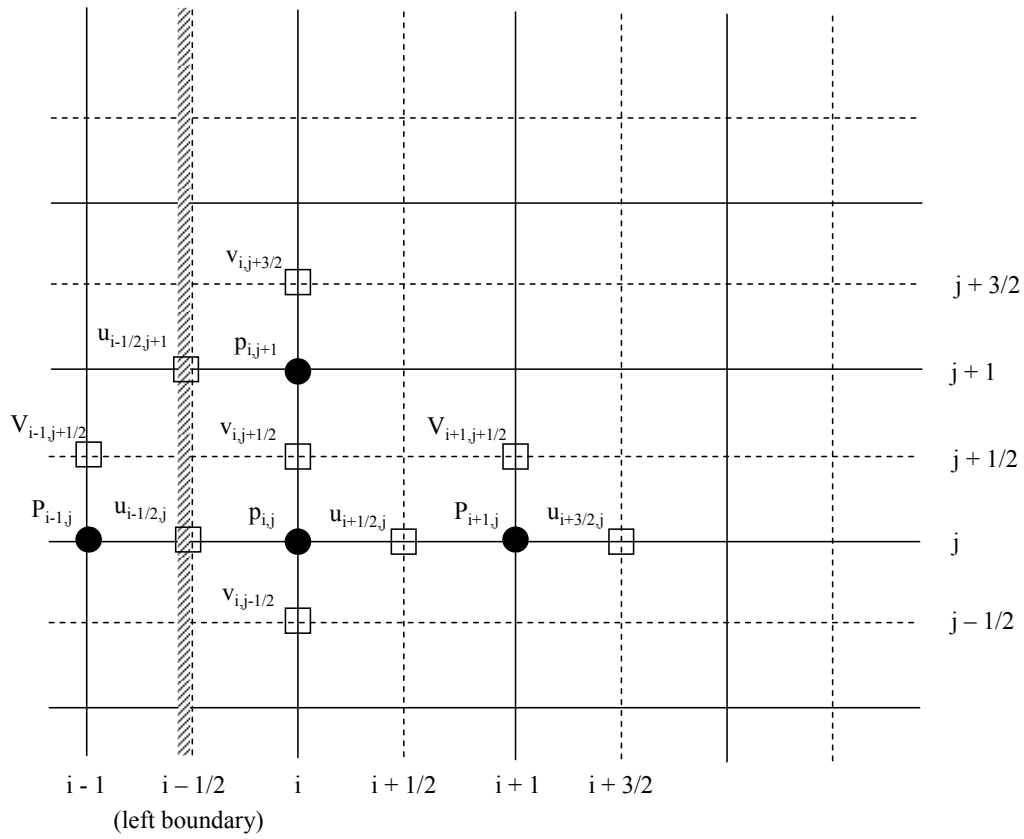


Figure 2.4: Sketch of the left boundary under the staggered grid. The left boundary is the axis of symmetry.

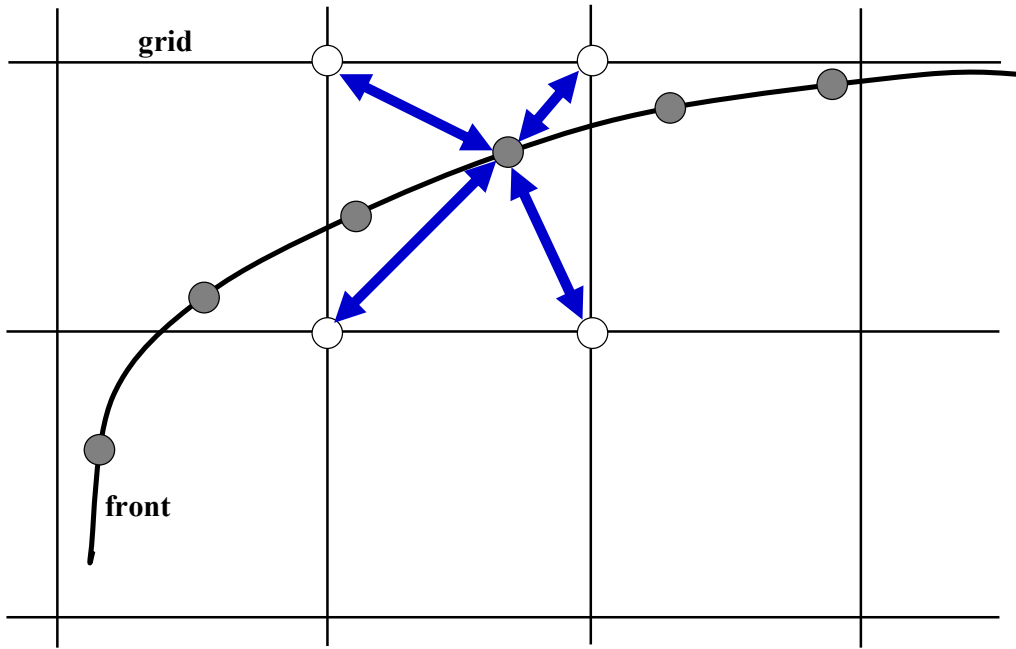


Figure 2.5: The grid and the front. The grey points represent the front and the white ones the grid. The front point gets its values from the corner points of the grid cell it is located.

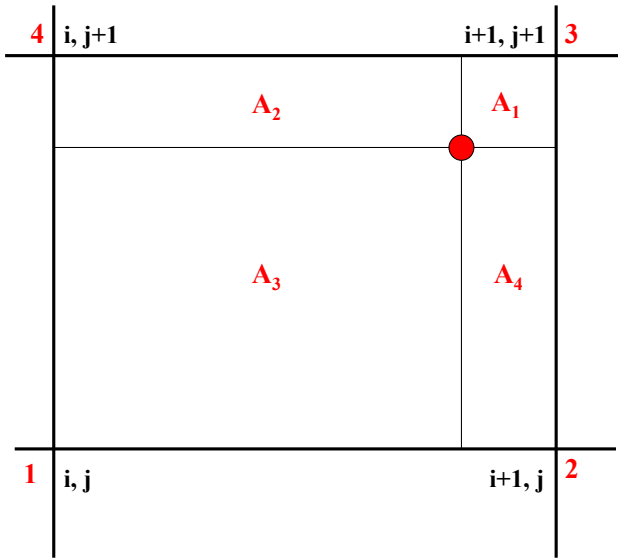


Figure 2.6: Front tracking – interpolating from the grid by area weighting.

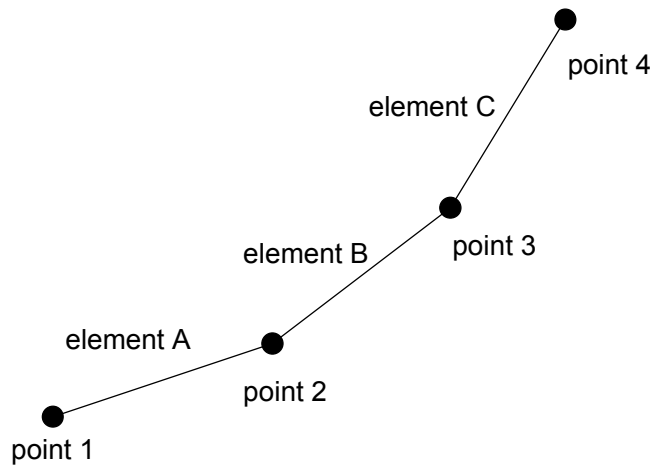


Figure 2.7: Front structure is sketched.

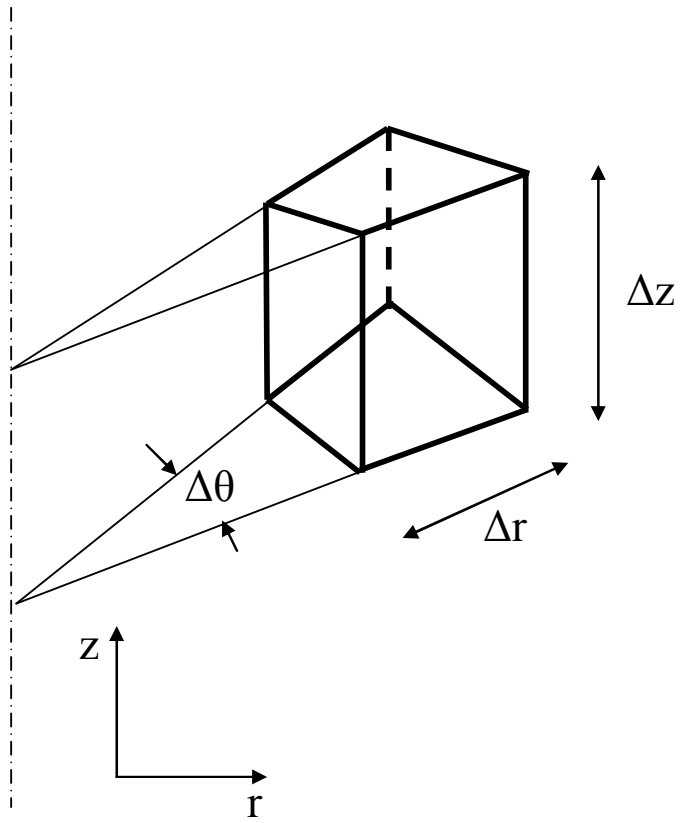


Figure 2.8: Volume element in axisymmetric coordinates.

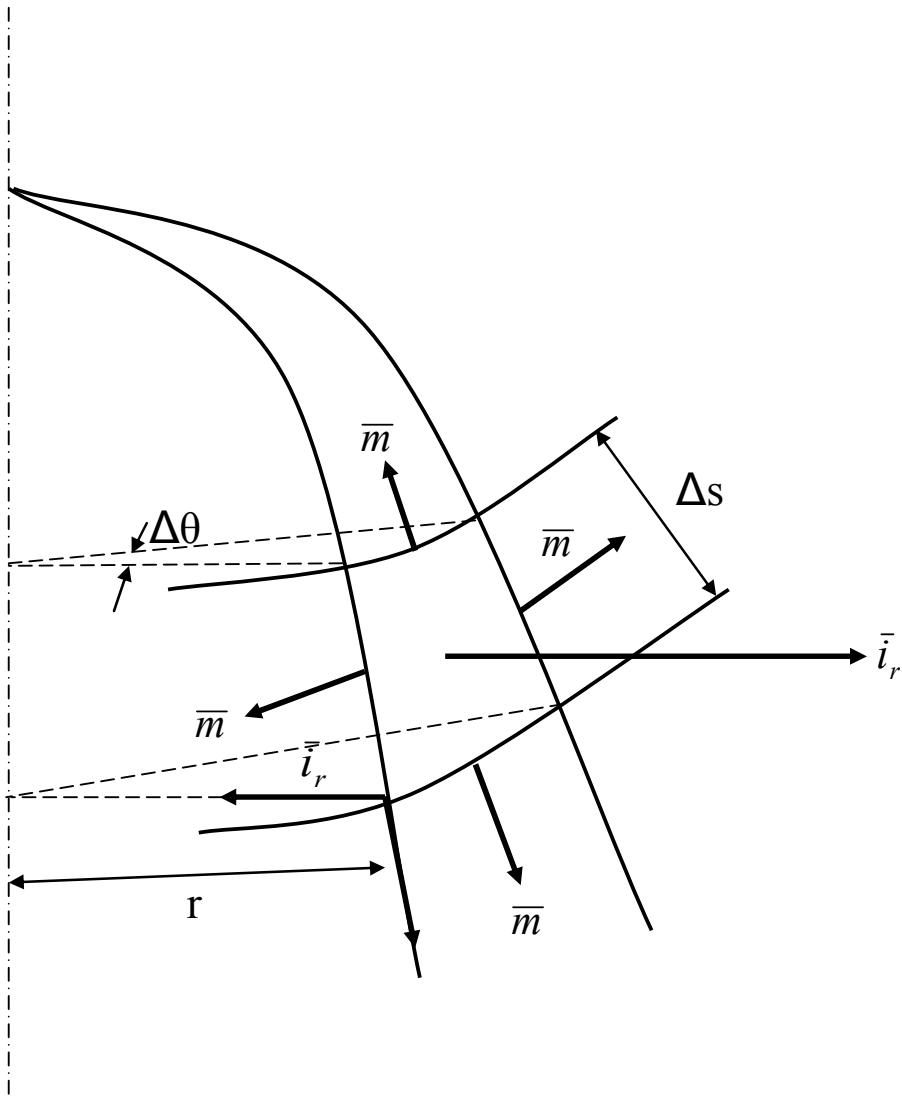


Figure 2.9: The forces acting on the surface element in axisymmetric coordinates.

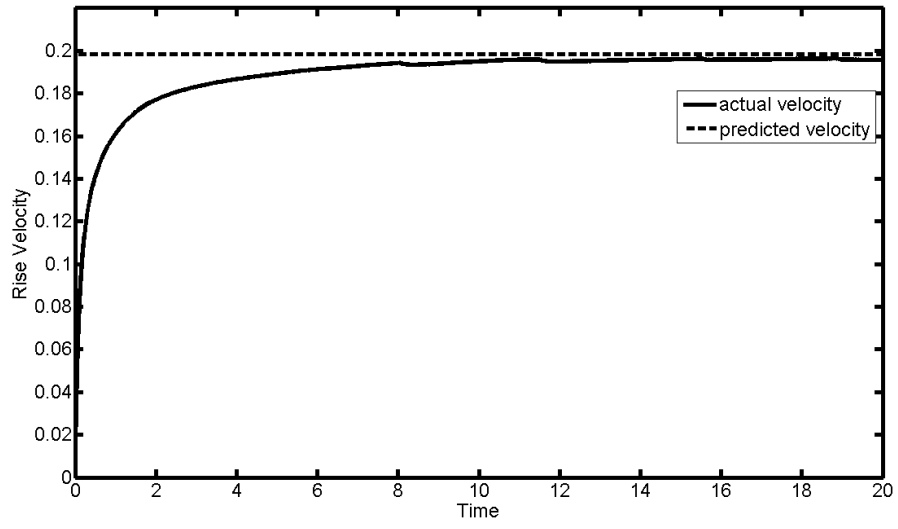


Figure 2.10: Convergence of calculated rise velocity to the theoretical value

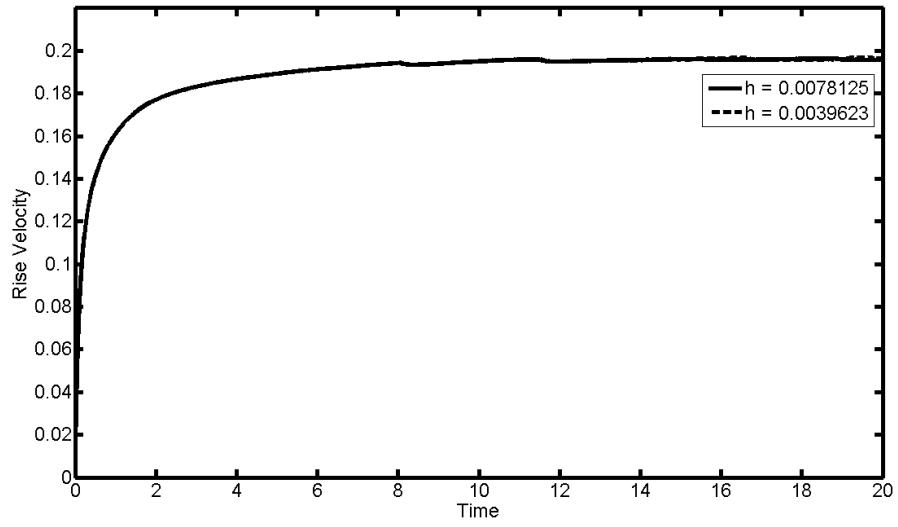


Figure 2.11: Rise velocity of a bubble in creeping flow. h is the grid size of the computational domain. The terminal velocity approaches the predicted value of 0.1984 and converges to the same value even as the grid spacing is lowered.

CHAPTER 3

-

ON THE IMPACT OF DROPS ON THIN LIQUID FILMS

3.1 Introduction

The dynamics of drop impact on a surface has interested researchers over the last hundred years. As with many phenomena, impact of liquid drops has both negative and positive aspects. The same mechanism that can damage an aircraft can be used to erode and cut materials, like glass, paper etc. Besides the most natural phenomenon of a rain drop impinging on the earth, there are countless practical applications. Industrial applications utilizing the drop dynamics include fuel injectors in internal combustion engines, ink-jet printing, spray coatings etc. The following is a review of the numerical and experimental studies that have been carried out in order to explain and recreate the dynamics of impact of liquid drops on liquid surfaces. Numerical simulations are vital in explaining physical occurrences, like various processes whose timescales are so short that they cannot be effectively captured using experimental techniques. Experiments need to be performed in cases where the length scales are extremely small, like the formation of secondary droplets during jetting.

This chapter is divided into three sections: literature review of droplet impacts in general, droplet impact on thin liquid films and the modeling of droplet impact on solid walls

3.2 Literature Review

The drop is a homogenous liquid, which can be described by its thermodynamic state and by its material properties like surface tension, viscosity and compressibility. The initial shape of the drop is usually taken to be spherical so that there are no drop oscillations to be considered, which render the shape of the drop to be time-dependent. A single drop is often the focus of the study, though in some rare cases a droplet stream is used. The interface between the drop and the target liquid is assumed to be a gas.

The impact velocity is a parameter that can be easily changed. The impact velocity is generally sufficiently small so the flow can be considered incompressible. Lesser (1995) mentions that if the impact is supersonic, the dynamics of the impact changes due to the presence of shocks. The passage of a shock causes the drop to shatter, if the distance between the drop and the surface is not extremely small. The target liquid is at rest and the surface is plane. The depth of the target liquid is of importance and its effects are described later on. The target liquid and the drop may not necessarily be the same. The differences in the target liquids cause a variation in the type of response to an impact.

The impact of a drop on a liquid surface may result in floating, bouncing, coalescence or splashing. Even a very thin film of liquid in the pool is enough to

interact appreciably with the lateral sheet to produce an upward motion. This means that the liquid film is necessary to produce an upward jet or a crown formation. For a solid surface, splashing, bouncing or absorption of the drop by the surface occurs.

Spreading and splashing are the two phenomena of interest. In the former case the drop disappears quickly in the target liquid, forming a small crater and virtually no secondary droplets are formed. A vortex ring is also formed below the surface of the liquid film if it is thick enough. Splashing can be characterized by the presence of a liquid column, or a central jet that rises out of the center of the crater formed by the impact. The central jet rises above the original undisturbed surface of the target liquid. Here the target surface is greatly deformed as observed by Rodriguez and Mesler (1985) and Rein (1993).

Early experiments by Rodriguez and Mesler (1985) on the transition from coalescence/spreading to splashing indicated that the transition is governed by Reynolds Number, Re , $DU\rho/\mu$ and Froude Number, Fr , $(U/gD)^{1/2}$, where U is the droplet impact velocity, D is the droplet diameter, ρ is the liquid density, and μ the liquid viscosity. For a Reynolds number larger than 3,000 and for a Froude number between 6 and 18, an impact of a water droplet on a water pool will result in a splash. However, subsequent experiments by Rein and others have established that the impact Weber Number, $We = \rho U^2 D / \sigma$ where σ is the surface tension, of the impacting drop is the important parameter. Froude Number was found to influence transition but its effect is lesser than the Weber Number. When the Weber Number is below the critical limit, We_{cr} , coalescence occurs and when We is above the We_{cr} , splashing occurs. Crucially though, there is no fixed critical number at which the transition

occurs. The boundary between coalescence and splashing is not sharp. An increase either in the impact velocity or the drop radius can lead to splashing. Computationally, a Weber Number of above 100 is accepted as the limit beyond which splashing can occur.

Bouncing is a phenomenon wherein the drop of liquid rebounds from the surface of the target. There is no crater formation. The reflected drop is likely to be smaller than the incident one. Hence, bouncing with slight pinch-off is also referred to as partial coalescence. Bouncing is observed to occur generally for droplet streams. This seems to suggest that disturbance on the target liquid surface produced by the preceding drops are important for bouncing to occur, because with single drops most of the impact energy is lost in forming a crater and the remaining energy is not sufficient for rebound. Thus, if the radius and impact velocity are low enough, bouncing can occur even on single droplets. Bouncing occurs at low Weber numbers, much like coalescence. The transition from bouncing to coalescence begins with partial coalescence. The impact angle is an important parameter for the transition. For large drops, $R = 15$ mm or greater, increasing the impact angle can mean transition from bouncing to coalescence. .

The impact velocity for coalescence is usually higher than that for bouncing. When the drop impacts on the liquid surface, the droplet material is deposited onto the bottom and the sides of a crater, the bulk of the material lying near the bottom. As the cavity sides collapse, the bottom simultaneously tends to rise back towards the original surface level. For coalescence to occur the crater should be shallow and the droplet rebounds to the surface before the sides collapses. The droplet is ensconced

in the target fluid itself. There are two physical phenomena associated with drop coalescence, i.e. vortex ring formation and the entrainment of the gas bubble. Both are discussed below.

When a drop impacts a layer of lower density it will sink and a vortex may be produced. The study of these vortex rings may be useful in identifying adulterations of oils. The phenomenon of the formation and the penetration of vortex rings into the target liquid are not very well understood. Early researchers observed that certain heights produce the most penetrating vortex rings. Also, there is an effect of the drop shape on the vortex ring formation, which is mediated by the crater dynamics. After its formation, the vortex ring expands and eventually becomes unstable. Essentially, the formation of vortex rings is low-velocity phenomenon. Increasing the impact velocity tends to suppress the vortex rings and causes a change in the crater dynamics. At higher velocities, the drop liquid does not mix with the target liquid and is found at the tip of the upward jet.

It has been noted that if the drop's energy on impact is sufficiently large, the thin-walled liquid cylinder created due to the impact closes at the top and forms a bubble that floats for a moment and then vanishes. The process is said to be governed by surface tension forces, and the duration is too short for gravity to take effect. As the canopy closes, the motion must stop abruptly and the inward-directed momentum generates a sharp pressure rise, that results in two nearly symmetrical jets, one directed upward and the other one downward into the cavity. It is the second jet that entrains the air bubble upon striking the water surface. The deeper craters associated with the higher energy impact collapse in a way that leads to the formation of an air

bubble that detaches from the crater floor. This is regular entrainment. It has also been observed that the formation of such bubbles is accompanied by the formation of thin, rapidly rising vertical jets that reach a maximum height of many drop diameters. Although the existence of capillary waves are a necessary condition for bubble entrapment, bubbles will only occur when the wave speed and maximum crater size is such that the wave reaches the bottom of the crater before the collapse has resulted in the formation of a thick Rayleigh jet. Bubble entrainment usually takes place for deep liquid layers only.

Prosperetti and Oguz (1993) devised a power law of the form, $We = k \cdot Fr^\alpha$ to determine the region of regular bubble entrainment. The region is located between the upper entrainment boundary and the lower entrainment boundary. Here, k is a constant equal to 0.25 for the upper line and 0.20 for the lower line, and $\alpha = 0.247$ and 0.179 respectively. It has been claimed that the region below the lower boundary defines the conditions for the vortex ring formation, the region within the boundaries give the conditions for bubble entrapment, those above the region correspond to the formation of thick Rayleigh jets. Vortex rings can also be present in the splashing region. The region above the upper boundary gives the conditions for the same. However, numerical results of Morton (2000) and others suggest that vortex ring formation is not restricted to impact conditions below the entrainment region and that a single impact can lead to the formation of multiple vortices. Results from simulations run at higher Weber Number predict the formation of a single, small vortex ring, along with the thick Rayleigh jet.

The main features of splashing are the crown formation and the rise of the liquid jet at the middle of the crater. The appearance of the crown is characteristic of splashing in its fully developed form. When a drop impacts on a liquid film with sufficiently high velocity (large Weber number), a liquid sheet is ejected upwards and almost normal to the film from the periphery of the drop. In the target liquid, a cavity is formed, which is initially cylindrical in shape and then it becomes a crater in the shape of a hemisphere. Small jets form and breakup into secondary droplets at the top of the ejected sheet, giving it a crown-like appearance. The crown propagated radially outwards from the center of impact. Much of the original drop material well below the surface and the crown is composed mainly of the target liquid. In the later stages, the crown thickens and the crater begins to collapse. This leads to the formation of the central jet that carries the drop liquid at its top.

Along with these, there is another phenomenon which occurs at the early instances of the drop impact. It is known as neck jetting, or the formation of the ejecta sheet. Neck jetting is disk-like jet formed at the neck between the drop and the target liquid, if the impact Weber Number is high enough. Thoroddsen (2002) was the first to observe the phenomenon using a drop mixture of water and glycerin. Later on, Davidson (2002) confirmed the neck jetting numerically by the VOF method and also mentioned that at low Weber number, the ejecta sheet cannot be seen.

Crown formation typically sets in at Weber Number equal to 100. According to experimental observations, the critical We for crown formation is of the order of 100, while that for jetting is about 40. Thus, the parameter ranges producing a transition regime are rather close to each other. As a result, a flow producing jetting at the very

beginning will then result in crown formation. For very thin films, the crown mainly consists of the liquid from the drop. At later times, an increase in the crown volume is more due to the accumulation of the liquid scraped from the film in front of the crown and sucked from the film behind it.

Yarin and Weiss (1995) theorized that the crown did not expand linearly in time, but that the crown radius varied to the square-root of the time. The relationship is of the form,

$$R = c t^{0.5} \tag{3.1}$$

where, R is the crown radius, and c is a constant. This dependence was further confirmed by Davidson (2002) with VOF, and Xie (2004) used moving-particle semi-implicit method (MPS) to do the same.

When the drop impacts on the free surface, there is an almost step-like jump in velocity. In an incompressible liquid with a free surface, the faster liquid particle push the slower ones, which inevitably results in a liquid sheet outflowing normally to the free surface, provided the velocity jump is large enough to allow the inertial forces to overcome the surface tension. This fact is general and independent of any specific shape of the liquid domain, generally resulting in the formation of free liquid jet with a high velocity. The central jet velocity can be as large as four times the impact velocity of the drop.

Jetting crucially depends on the impact velocity. It does not set in when the latter is low enough. When the velocity is low, the whole neck region moves outwards under the action of surface tension, and capillary waves begin to propagate outwards.

Also, for thin liquid films, $H/R < 0.25$, where H is the liquid depth and R is the drop radius, the central jetting does not take place. Viscosity is shown to play a major part in the region by deciding the width of the jet. Surface tension determines whether the jet is formed or not. Shin and McMahon (1989) observed that the high-speed central jet can be seen only for H/R greater or equal to 4.0. Manzello and Yang (2002) stated that reducing the Weber number can suppress the central jet even if the other conditions are favorable.

Rein (1996) further separated the jetting region into several sub-categories. At a Weber number just above the transition to jetting, a thick jet was observed to rise above the free surface with no secondary jet formation. Subsequent increase in Weber number resulted in thin high-rising jets with several tiny droplets ejected from the jet. Increasing the Weber number yet further, beyond the region of regular entrainment, resulted in thick jets with large droplets breaking off from the jet.

Central jetting caused by the inertial forces without any compressibility effects involved, and results in a free radial jet. By contrast, the neck jetting occurs due to the compressibility effects at the drop bottom, and results in a wall jet leading to a formation of the contact area. Also, the neck jetting only occurs at very high Weber numbers, $We = 2000$ and above.

This jet can pinch off a torus-shaped liquid volume at its tip or reconnect with pre-existing liquid film, thus entraining a torus-shaped bubble. The sheet originates from the liquid layer. The shape of the ejecta sheet is initially horizontal, then pulled by the crown formation. The ejecta sheets represent a new mechanism for generating

secondary droplets and suggest a repeatable way of studying dynamics of rapidly stretching thin liquid films subjected to surface tension and viscous forces.

The impact of the thickness of the liquid layers on the impact phenomena varies. The bottom layer depth ratio, H/R was varied from 1.7 to 0.5, the results were indistinguishable. One concludes that these ejecta sheets were not driven by the presence of the solid boundary. It is observed that when the depth of the liquid layer is lesser than the crater radius, there is no jetting. The height of the rebounding jet reaches a maximum for a certain pool depth. For very shallow pools, the height of the jet is limited by the fact that not enough liquid is readily available to feed it. For deep pools, a substantial amount of liquid flows into the jet which is therefore thicker and is limited by gravity in its ascent. For shallow liquids, jet formation is unlikely, instead a crown is formed. Also, for shallow liquids, especially with high velocities, the author is not aware of any description of bubble entrainment in literature.

Viscosity has a strong effect on the capillary waves. Highly viscous liquids damp out the capillary waves and the splashed rim of the crown distorts weakly and is not prominent. Also, the ejecta sheet from the neck region emerges earlier for lower viscosities, converges to fixed value for smallest viscosities. The less viscous impacts, ie high Reynolds number, result often in splashing or its allied phenomena. The less viscous the fluid, the thinner the corolla and the larger the angle between the liquid sheet and the liquid layer. For the highest Reynolds number the impact is rapidly followed by secondary droplet break-up.

High surface tension, i.e. low Weber number, suppresses the crown formation. At high surface tension, instead of the jet, the neck of the drop moves outwards. At low

surface tension, the damping of the secondary droplets does not take place resulting in the crown formation. For lower surface tension, the central jet is thinner and faster. At intermediate values of surface tension, an intermediate scenario between the motion of the whole neck region and formation of a jet occurs; jetting proceeds against the background of the developing motion of the whole neck.

When the drops impact solid walls, they generally spread. Rein (1993) indicates that the kinetic energy of the drop is not high enough to induce splashing and the nature of the spreading is influenced by intermolecular forces. The spreading rim is unstable and does not come to rest immediately. The drop spreads to a maximum radius and recoils back, creating an oscillatory effect. This may sometimes lead to the rebounding of the drop from the surface itself. The contact angle between the liquid drop and the solid surface plays a part in the rebounding of the drop. Given the initial conditions are conducive for rebounding, the higher the contact angle, the greater is the height to which it rebounds, Gunjal et. al (2005).

Studies on drop impact have been done in great detail, and the references discussed here are only a fraction of the relevant literature. Numerical simulations of the drop impact on a solid surface have been done by Pasandideh-Fard et al. (1996), Mao et al. (1997), Bussman (1999) and other researchers. For impacts on liquid films, additional sources include Josserand and Zaleski (2003), Weiss and Yarin (1999) and Federochenko and Wang (2000).

Summarizing, the Weber Number is probably the single most important parameter in determining the aftereffects of a drop impact on a surface. The Weber number

alone is not enough, the Reynolds Number and Froude Number are necessary factors too, but predicting the nature of the impacted flow would be very difficult without it. The other vital parameter required is the liquid depth, since a number of phenomena like jet formation and bubble entrainment cannot happen if the fluid depth is very low. There is no strict limit on the depth, but it is generally accepted that $H/R > 0.5$ to capture jet formation and bubble entrainment.

3.3 Problem Statement and Numerical Formulation

A droplet of diameter D and composed of fluid of higher density is moving with an initial velocity U , in a fluid of lower density. The initial velocity is in the downward direction. The domain is sketched in Figure 3.1. The bottom wall is assumed to be rigid, covered with a thin film of the same fluid as the droplet. Table 3-1 provides the list of the parameters and their values. The parameters that are varied include the drop velocity and the viscosities of the liquid and gas. The variations of these quantities and the non-dimensional numbers are included in Table 3-2.

The governing equations and the numerical methods used to track the splat of the droplet is the same as discussed in Chapter 2.

3.3.1 Results and Discussion

The purpose of this section is to understand the effect of the various parameters that describe the drop impact on a thin liquid film. The simulations were run using a

drop having the same diameter D , in all cases. Other parameters held constant include the film thickness, surface tension, density ratio etc. From Figure 3.3, we can see the progress of the drop as it impacts the liquid layer. Here, $Re = 200$, $We = 32000$, $\rho_L / \rho_G = 100$, and $\mu_L / \mu_G = 100$. While selecting the parameters to study the flow, care was taken that the crown did not touch the top or side walls.

Due to the initial velocity of the drop, a narrow jet of the liquid is ejected out. This is the genesis of the splash process. As the drop falls deeper into the liquid film, the mass of the ejected jet grows and moves radially outwards. From this jet a lamella forms and propagates as a crown. The crown is mostly composed of the target liquid, but some of the drop liquid is also found in it. After the crown is formed, it increases in diameter and in height for some time. In the later stages in some cases, the crown may stop growing and start to bend inwards towards the center.

In the initial stages, the impact velocity is the most important parameter. The effects of the liquid viscosity come into picture after crown formation and propagation. The viscous effects are felt close to the bottom wall. The reason is that the film thickness is very small in this region and thus has less inertia, making it more affected by viscous forces. However, this is valid only in case of no-slip boundary conditions.

At time $t^* = 0$, where t^* is the non-dimensional time and is given by $t^* = \frac{Ut}{D}$, the entire drop is moving with a uniform velocity, which has induced an internal circulation. In the next frame in Figure 3.3, the ejected jet is observed. In the next frames, the crown moves ahead in the radial direction. A small amount of circulation

also develops subsequently near the center axis. The velocity of propagation of the crown is not as high as the initial jet.

With higher viscosity liquids, secondary droplets can be seen detaching from the crown after it is fully developed, as seen in the model developed by Trujilo and Lee (2001). But these effects are essentially three dimensional in nature, and therefore not captured accurately in our axisymmetric formulations. In some of our simulations, rollups of the crown was observed. In our study, we are concentrating on the early times after the impact, therefore the phenomenon of crown rollup and inward bending were not given due attention. The presence of surface tension in the calculations has an effect on the crown formation. High surface tension, i.e. low Weber Number, suppresses the crown formation. At low Weber Numbers, instead of the jet, the neck of the drop moves outwards. At higher Weber Numbers, crown formation results.

All the cases in the present study are run with the density ratio, $\rho_L/\rho_G = 100$. Our axisymmetric study can handle density ratios of up to about 500. But if we consider density ratios in the excess of 1000, we experience numerical instabilities at the interface. The interface is not smooth. Therefore, the time taken to solve the equations at this high density ratio is prohibitively larger.

Figures 3.2 and 3.4 show the progression of the splashes at $Re = 100$ and 250 respectively. In the case with the lower energy of impact, the splash is less pronounced as compared to Figure 3.3. Also, the splash subsides sooner and also does not go as far. For the higher Re in Figure 3.4, the maximum of height of the splash as well as the spread is larger than in Figure 3.3.

Figure 3.5 displays the splash under the full-slip boundary condition. The parameters of Figures 3.3 and 3.5 are similar to each other except for the boundary condition.

Looking at the first few frames of 3.3, it is exactly as described earlier in this section. But as time progresses, the rate of crown propagation as well as crown growth lessens. As time proceeds, the crown propagation ceases. Then, the crown collapses losing its height. The direction of this collapse is radially inwards. The speed at which the crown collapses is much lesser than the speed of crown propagation. According to Rein (1996), if the impact energy is high enough, the crown on its inward collapse will form a central jet around the axis at the origin. In our case, the crown does not have sufficient energy, plus the liquid layer is very thin. So, the collapsing crown meanders towards the central axis at a very slow speed.

For the full-slip condition, at very short time, the splash looks almost like the no-slip case. But as we march ahead in time, differences appear. Comparing the crowns, we can see that the lamella in the no-slip condition is thinner. Also the angle between the lamella and the liquid layer is larger in the no-slip case, whereas in the full-slip condition, there is practically no vertical angular displacement of the crown. The crown in the full-slip condition, though it slows down in time, never reaches standstill. The crown continues to move radially outwards. But like in the no-slip case, the crown height reaches a maximum and then it collapses.

In the full-slip condition, the energy of the moving splash is larger. The splash carries much more target liquid along with it than in the no-slip case. If we compare the thickness of the liquid films near the central axis under both conditions, we can see that there is hardly any liquid film in the full-slip case.

This difference in energy can be explained by the fact that in the no-slip condition, energy is dissipated in order to overcome the viscosity in the boundary layer. The excess energy is manifested in the full-slip condition by a larger crown radius and crown height. The energy dissipated during drop impact is given by the equation,

$$\text{Diss}_{a-b} \approx \Phi V t_c \quad (3.2)$$

where, Φ is the dissipation function, V is the volume and t_c is the time taken. The dissipation function is given by,

$$\Phi = \mu \left(\frac{\partial u}{\partial z} + \frac{1}{r} \frac{\partial rv}{\partial r} \right) \frac{\partial u}{\partial z} \quad (3.3)$$

Now Φ can be scaled as,

$$\Phi \approx \mu \left(\frac{\partial u}{\partial z} \right)^2 \approx \mu \left(\frac{U}{H} \right)^2 \quad (3.4)$$

where U and H are constants for a given case. Therefore, the dissipation function and the dissipated energy depend on the value of μ . Thus, as μ decreases, the dissipated energy decreases. We can conclude that as we approach the inviscid limit $\mu \rightarrow 0$, the no-slip condition approaches the full-slip condition. This will be quantified further in the studies that follow.

From (3.1), the relationship between the crown radius and time is established. We shall first check whether this dependence holds good. A couple of tests were run at

the same Re ($= 167$), but at different We ($= 1667, 2500$). The results can be seen in Figure 3.6. The y-axis is the square of the non-dimensional crown radius and the x-axis is the non-dimensional time. The equation for the straight line is

$$R^2 = 0.391t^* + 0.1576 \quad (3.5)$$

where R is the ratio of the crown radius to the initial drop diameter.

In the following sections, we consider the comparative effects of full-slip and no-slip boundary conditions on crown radius and crown height based on Reynolds number and Weber number variations, and the evolutions of kinetic and surface energies.

3.3.2 Effect of dissipation on crown height

The variation of the crown height at different Re ($Re = 50$ to $Re = 250$), keeping We constant ($We = 32000$) is shown in Figure 3.7. The crown height curves for both full-slip and no-slip walls exhibit similar characteristics in the sense that they reach a maximum height and gradually decrease. The rate of increase in the crown height leading up to the maximum is much higher than the rate of decrease from the maximum. Predictably, at larger Re , the crown height curves are higher. At any given time, the crown height increases with an increase in Re . On comparing the full-slip and no-slip curves at the same Re , the crown height is higher in the full-slip case. This difference in heights is more marked at $Re = 250$ than at $Re = 100$. The viscous dissipation at the solid wall suppresses the crown height.

The effect of We is displayed in Figure 3.8. The Reynolds number is kept at 200. Under both conditions, the curves are remarkably similar to each other. For all the

curves shown, the onset of the maximum height is almost at the same time, as compared to those in Figure 3.7. Thus, Re influences the time taken by the crown to attain its highest point. Here, too there is a significant difference in the full-slip and no-slip cases, suggesting that the presence of the boundary layer influences the crown height.

3.3.3 Effect of dissipation on crown radius

The definition of crown radius can be slightly tricky at times, because the crown is not always cylindrical. Cossali et al. (2004) have defined two crown diameters to account for the uncertainty. One is the upper external diameter measured at the base of the rim, and the other is the lower external diameter measured at the crown base. For our simulations, we take only one crown diameter (or radius). The crown radius is defined as the distance from the center axis to the crown base.

Figure 3.9 shows the variation of crown radius with respect to time for the full-slip and the no-slip conditions. Looking at the plot, we see that the no-slip curve reaches close to a maximum value and then “plateaus” out, while the full-slip curve is still growing, even though the rate of growth is slowing down. The no-slip curve seems to have hit a constant value and looks poised to collapse inwards. We have considered only the progress of the splash in our investigations. The full-slip curve quantifies the motion of the front as seen in Figure 3.5 and is quite close to the side wall. These differences in the crown radii over time for the no-slip and full-slip cases demonstrate the effect of dissipation on the crown motion. Keeping all the other variables constant, we varied the viscosity to obtain four values of Reynolds Numbers ($Re = 50, 100, 200, 250$ and 333). At any given time, it can be observed that at higher

Reynolds Number the crown radius is greater. At higher Re , the curves are bunched closer under both the boundary conditions. It can be inferred that there exists a viscosity limit, meaning that reducing the viscosity below a certain value will not induce any significant increase in the crown radius. This effect is also visible when we change the impact velocity and keep other parameters constant (Figure 3.10).

On varying We , for no-slip case, the curves overlap each other after a short time (Figure 3.10). The full-slip curves are uniformly spaced and follow a similar trend to each other. There is a significant distinction between the no-slip and full-slip curves and it grows larger as We goes higher.

3.3.4 Effect on kinetic energy and surface energy

The kinetic energy (E_k) and surface energy (E_s) of the drop on a liquid film are given by,

$$\begin{aligned}
 E_k &= \int_A \rho_L \pi (v_r^2 + v_z^2) dA \\
 E_s &= \sigma S_d
 \end{aligned}
 \tag{3.6}$$

where A is the cross-sectional area of the drop in the r - z plane, S_d is the surface area of the drop and the film. From the equation of kinetic energy it is clear that the resultant velocity is the crucial parameter in determining the kinetic energy of the system. From the spread velocity profile, it is clear that the resultant velocity of the splash decreases as time goes on. The initial kinetic energy is utilized in overcoming the viscosity and in increasing the surface energy of the splash. The kinetic energy curves in Figure 3.11 show that there is a sudden and dramatic drop after a short period of time. This is valid for both the cases. The kinetic energy values at the early times are almost the same for both. But the velocity effectively hit zero for the no-

slip case after some time, $t^* = 4$. In the full-slip case though, the energy never hits zero during our window of observation, but it is on its way down. At later times, $t^* > 4$, the two velocity curves are almost the same. On plotting the values of kinetic energy against time in Figure 3.11, we see that the kinetic energy also nearly touches the zero axis, meaning that almost the entire kinetic energy is spent.

The surface energy is plotted for different values of Re , keeping the impact velocity the same, in Figure 3.12. The trend here is that as Re increases, the surface energy at any given time increases. This is because the viscosity is reduced to get higher Re , which means that lesser kinetic energy needs to be utilized in overcoming viscous forces. Therefore, more energy is available to increase the surface energy. This implies that the surface area increases as the surface tension over the liquid-gas interface is held constant. The surface energy for the no-slip condition actually falls at later times, implying that dissipation takes a toll on the surface energy as the kinetic energy is nearly zero at that moment.

3.4 Conclusions

The tests are run at relatively low Re but at high We to promote splashing. The main splashing characteristics, the initial jetting and the crown formation and propagation are observed. The presence of secondary droplets at the edge of the rim could not be discerned due to the dimensional limitations in the axisymmetric code.

The kinetic energy of the drop dissipated with a short time, irrespective of the wall boundary condition. The point of the distinction between the wall conditions was the

presence of a small velocity in the full-slip condition. Part of the dissipated kinetic energy is consumed in order to increase the surface energy. The surface energy (or surface area) is seen to increase if the Reynolds number is increased or the impact velocity is increased with the Reynolds number kept constant.

The no-slip boundary condition approaches the full-slip boundary conditions in cases where the viscosity approaches the inviscid limit. It is clear that the viscous dissipation at the solid wall is significant. High impact energy is needed to overcome it and this result in the suppression of the splash characteristics, such as crown height, crown radius and the surface energies.

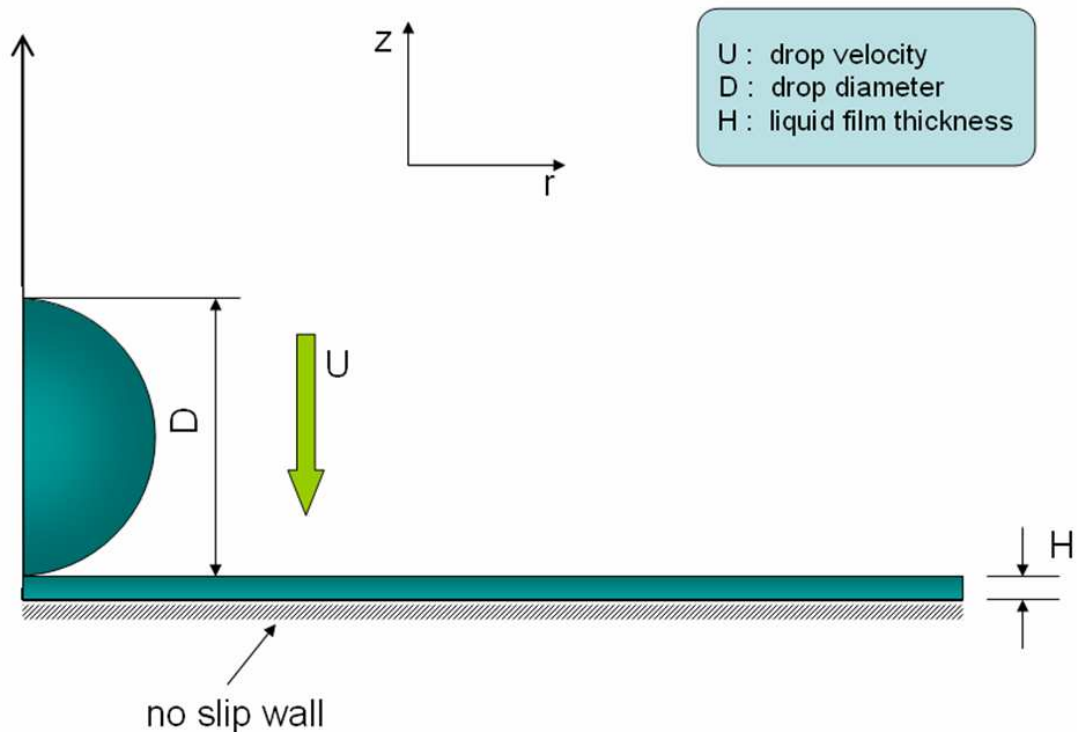


Figure 3.1 Problem setup. The initial diameter of the drop is D and the initial velocity is U . The thickness of the liquid film is H .

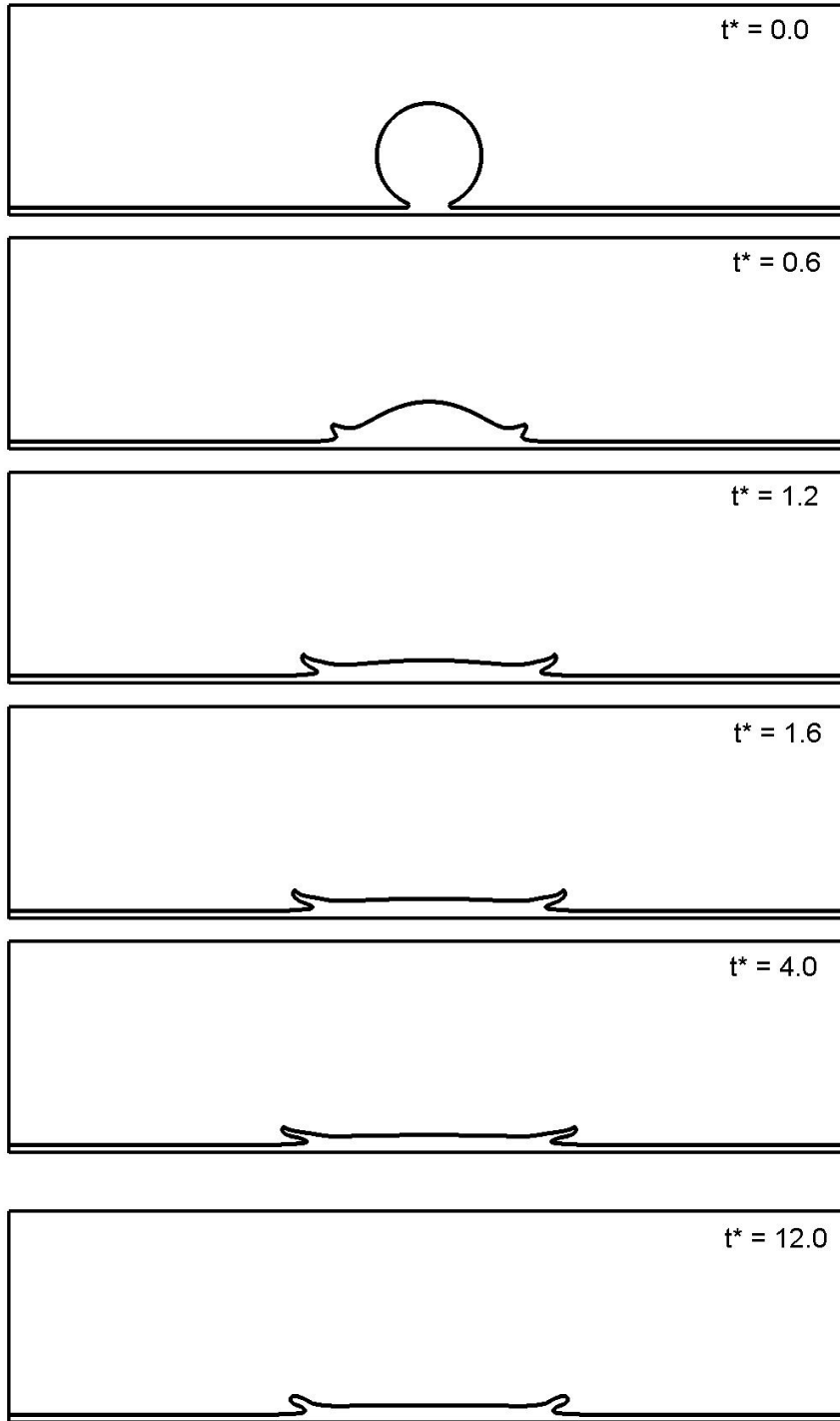


Figure 3.2: Splash Progression at initial velocity $U = 2.0$, $Re = 100$, $We = 32000$. Grid dimensions are 2×1 . The number of grid points in the present case are 256×128 . The grid resolution is non-uniform, with a minimum grid size of 0.005 .

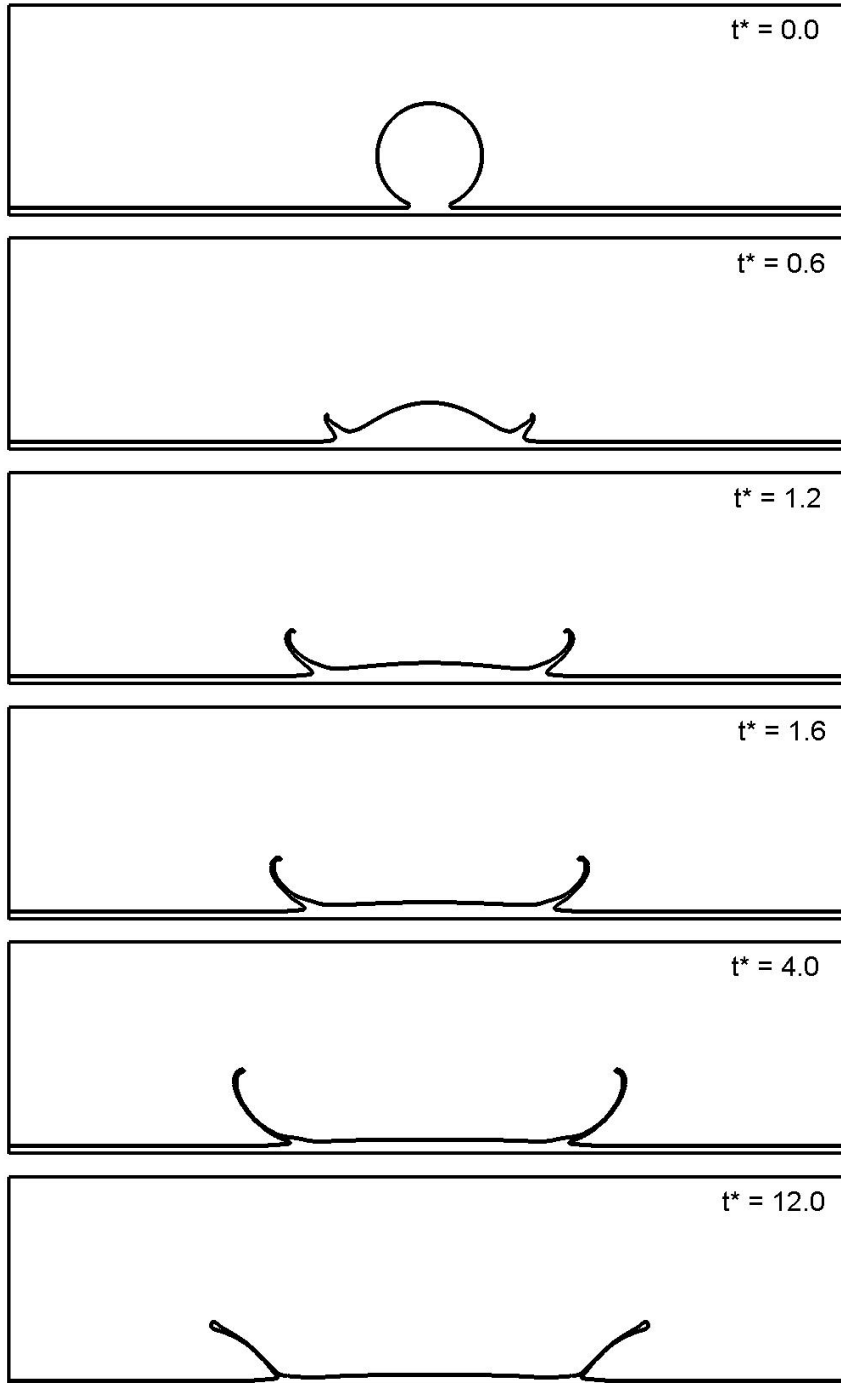


Figure 3.3: Splash Progression at initial velocity $U = 2.0$, $Re = 200$, $We = 32000$. Grid dimensions are 2×1 . The number of grid points in the present case is 256×128 . The grid resolution is non-uniform, with a minimum grid size of 0.005 .

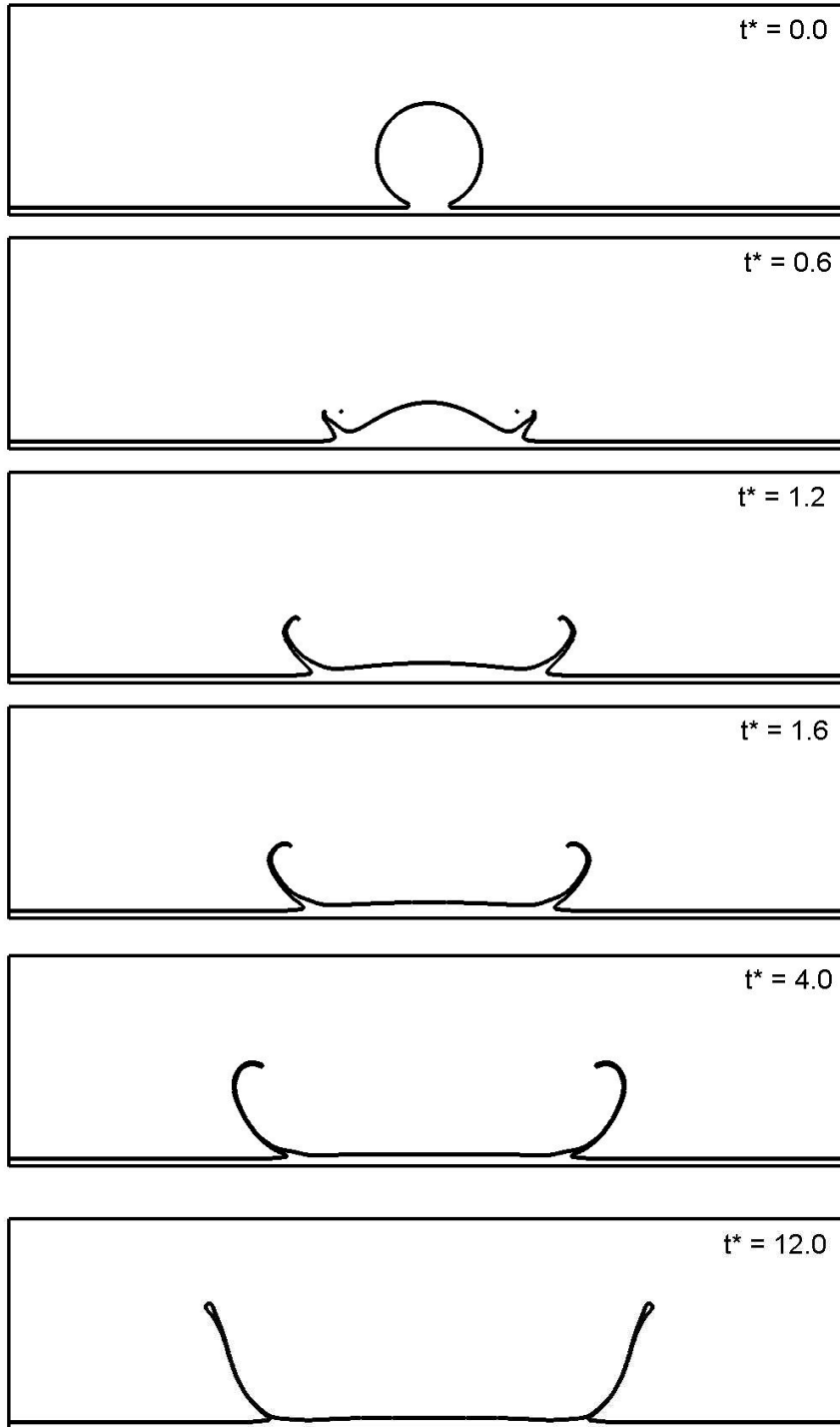


Figure 3.4: Splash Progression at initial velocity $U = 2.0$, $Re = 250$, $We = 32000$. Grid dimensions are 2×1 . The number of grid points in the present case is 256×128 . The grid resolution is non-uniform, with a minimum grid size of 0.005 .

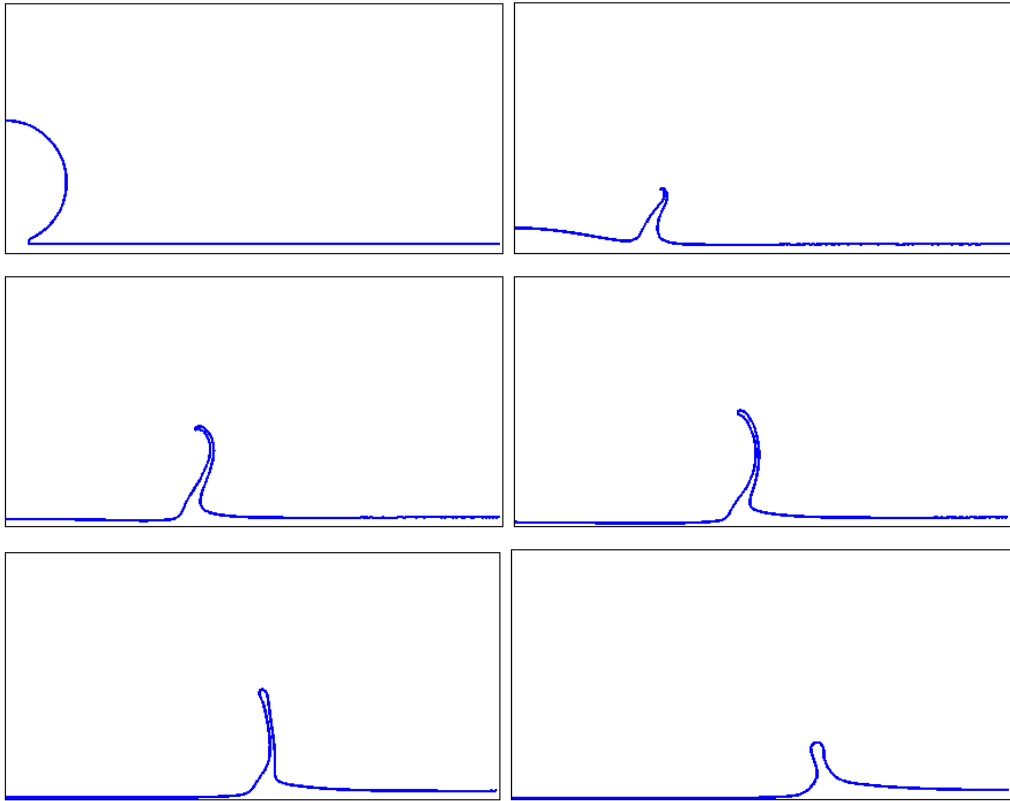


Figure 3.5: Splash Progression for the full-slip wall condition at initial velocity $U = 2.0$, $Re = 250$, $We = 32000$. Grid dimensions are 2×1 . The number of grid points in the present case is 256×128 . The grid resolution is non-uniform, with a minimum grid size of 0.005 .

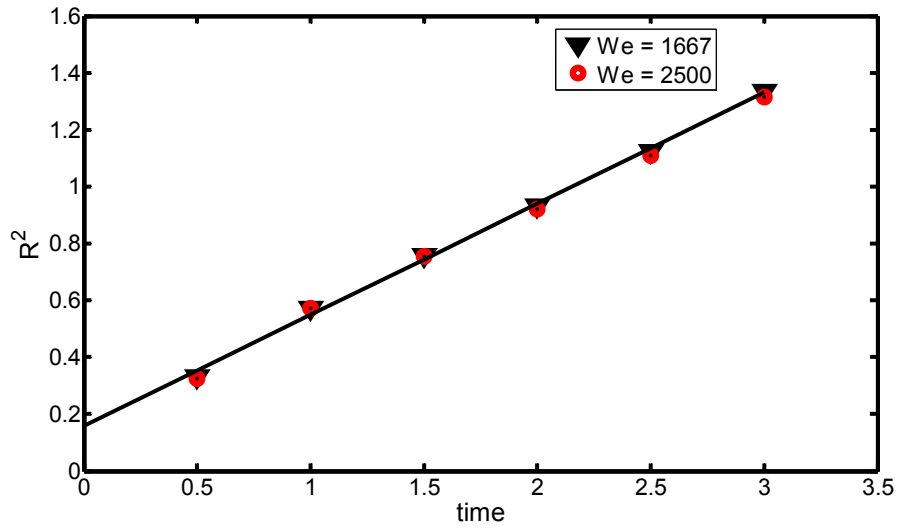


Figure 3.6: Square of the crown radius versus time under two sets of conditions. The straight line indicates the linear relationship between the crown radius and the square-root of time.

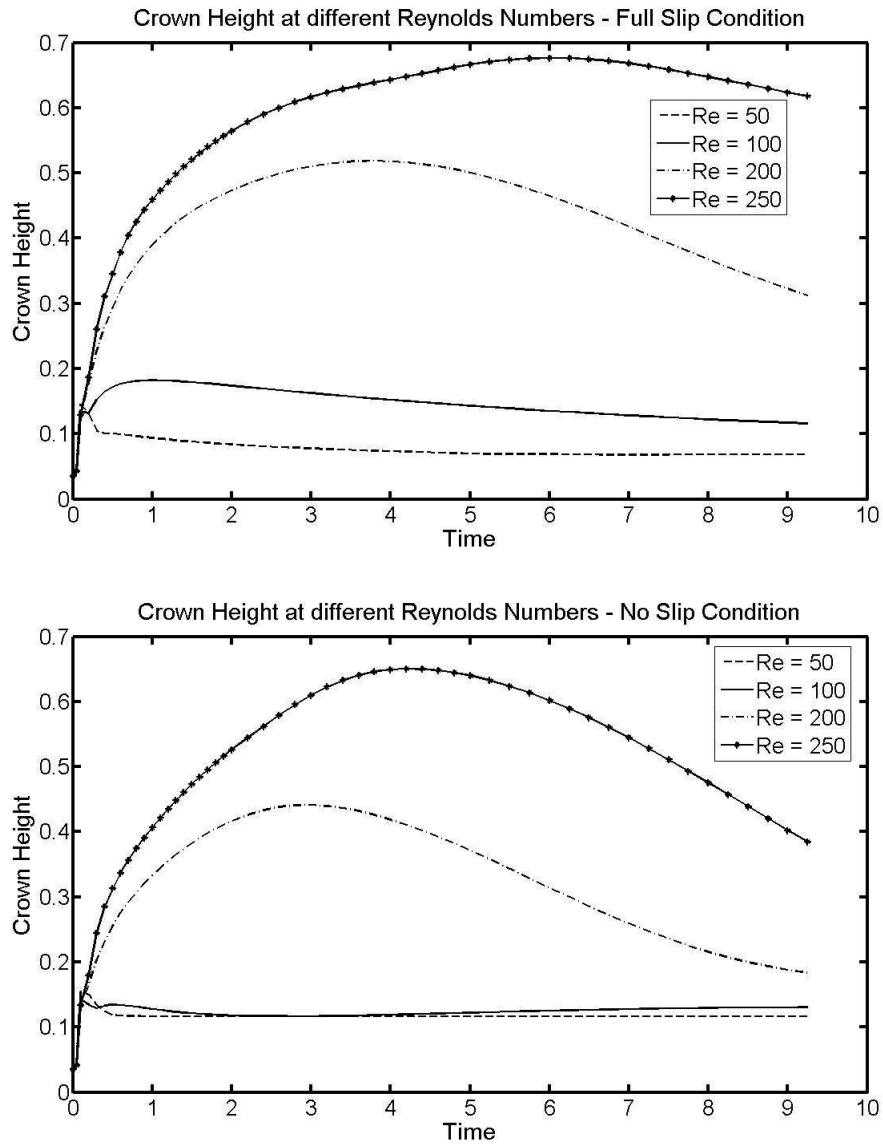


Figure 3.7: The evolution of the height of the crown from the time of impact to the end of the splash. The first figure is with the full-slip wall conditions and the second figure is for the no-slip case. The initial velocity is $U = 2.0$ and Weber Number, $We = 32000$ and Reynolds numbers ranging from 50 to 250. The thickness of the thin film is 0.035.

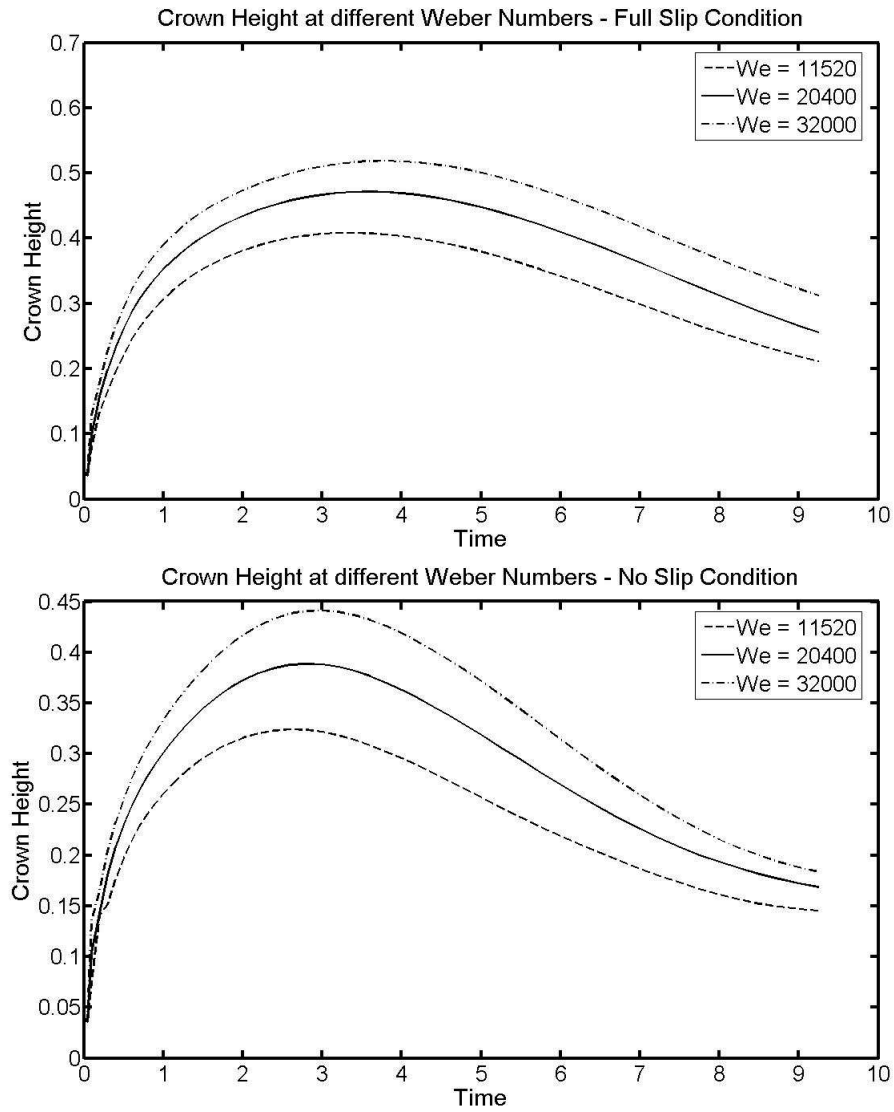


Figure 3.8: The evolution of the height of the crown from the time of impact to the end of the splash. The first figure is with the full-slip wall conditions and the second figure is for the no-slip case. The initial velocity is $U = 2.0$ and Reynolds Number, $Re = 200$ and Weber number, $We = 11520, 20400, 32000$. The thickness of the film is 0.035 .

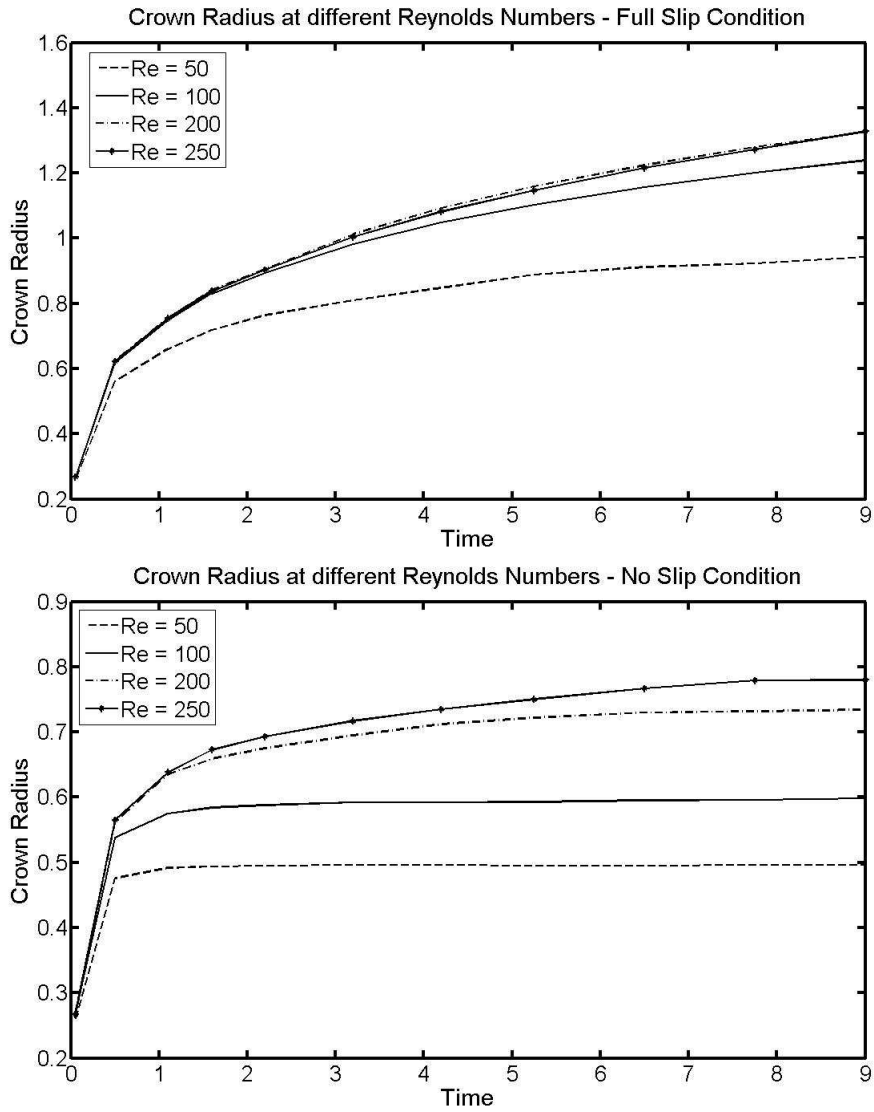


Figure 3.9: The progression of the radius of the crown from the time of impact to the end of the splash. The first figure is with the full-slip wall conditions and the second figure is for the no-slip case. The initial velocity is $U = 2.0$ and Weber Number, $We = 32000$ and Reynolds numbers ranging from 50 to 250. The thickness of the thin film is 0.035.

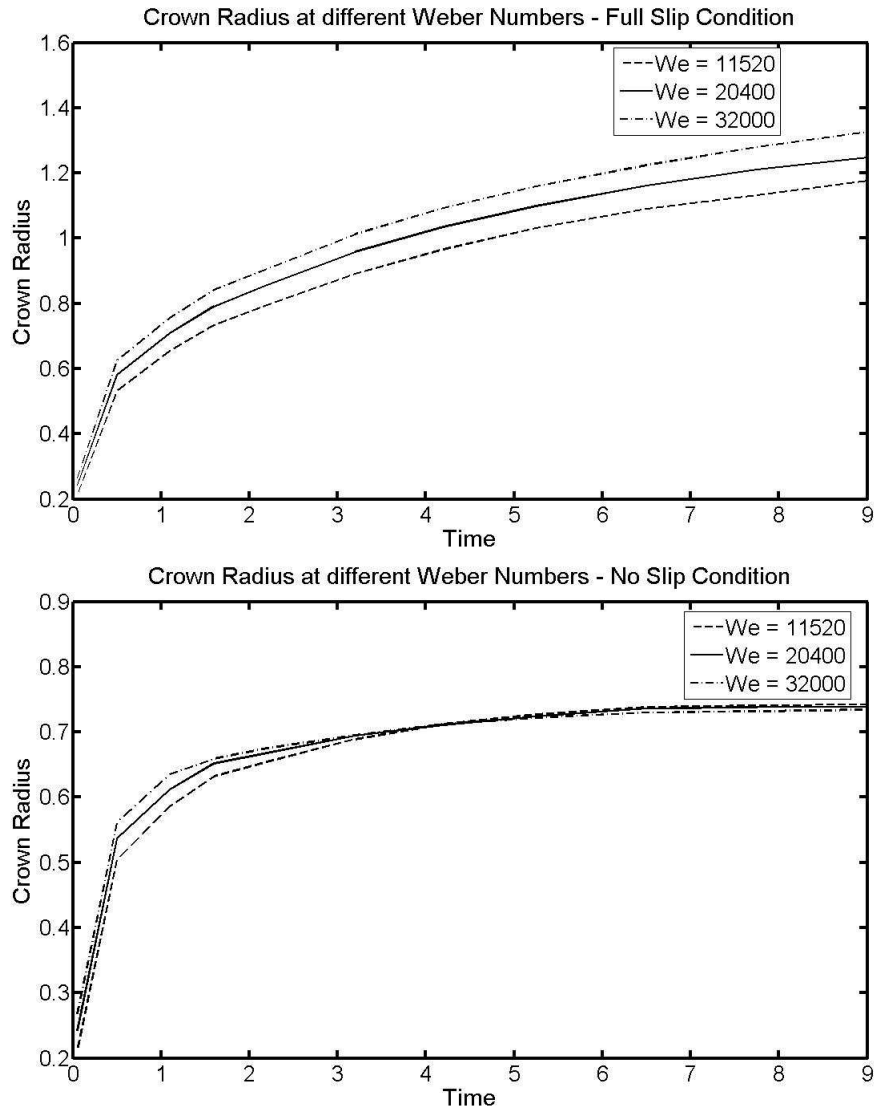


Figure 3.10: The progression of the radius of the crown from the time of impact to the end of the splash. The first figure is with the full-slip wall conditions and the second figure is for the no-slip case. The initial velocity is $U = 2.0$ and Reynolds Number, $Re = 200$ and Weber number, $We = 11520, 20400, 32000$. The thickness of the film is 0.035 .

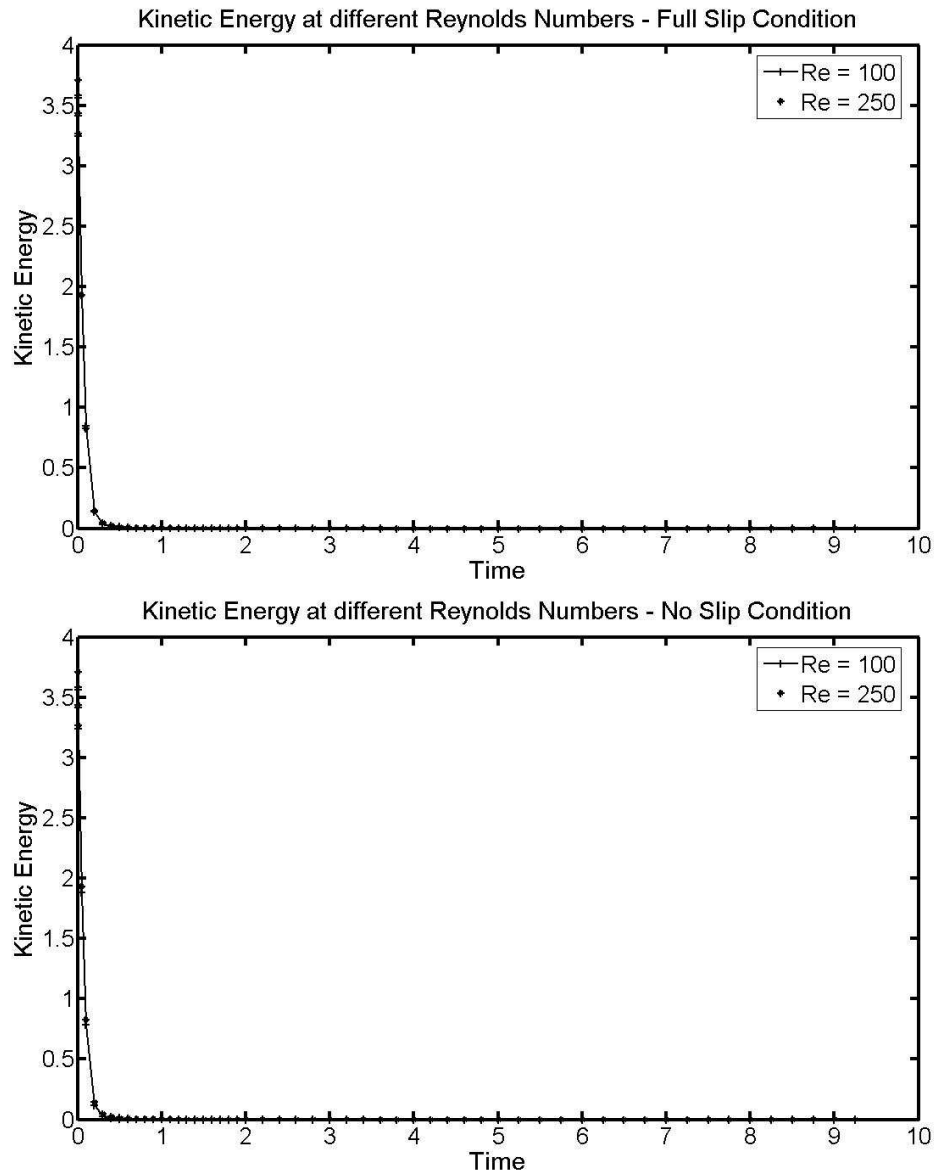


Figure 3.11: The kinetic energy of the system from the time of impact to the end of the splash. The first figure is with the full-slip wall conditions and the second figure is for the no-slip case. The initial velocity is $U = 2.0$ and Weber Number, $We = 32000$ and Reynolds numbers, $Re = 100$ and $Re = 250$.

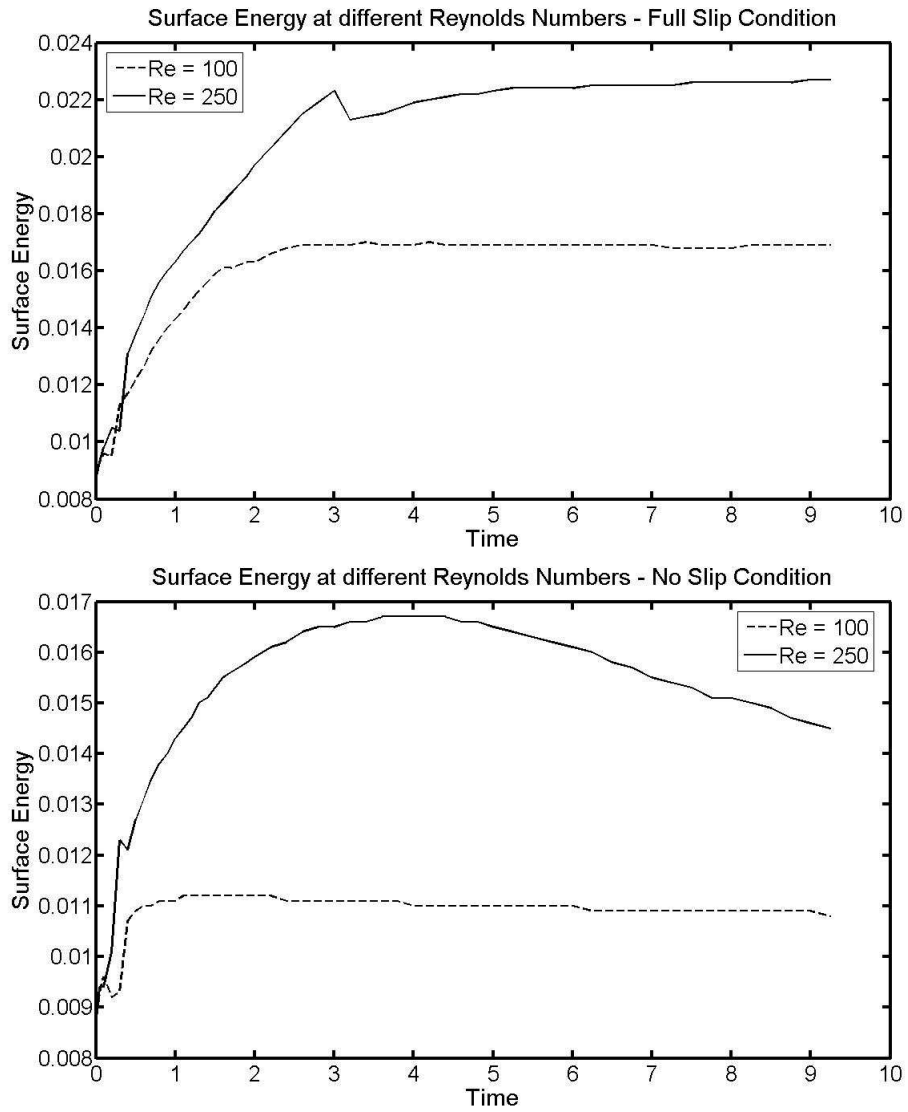


Figure 3.12: The surface energy of the system from the time of impact to the end of the splash. The first figure is with the full-slip wall conditions and the second figure is for the no-slip case. The initial velocity is $U = 2.0$ and Weber Number, $We = 32000$ and Reynolds numbers, $Re = 100$ and $Re = 250$.

Parameters	Value
Density Ratio : Fluid/Gas	10/0.1
Diameter of the drop	0.5
Liquid film thickness	0.035
Non-dimensional film thickness	0.07
Surface Tension	6.25e-4
Domain size	2.0 x 1.0

Table 3-1 Constant parameters. All dimensions except the non-dimensional film thickness are in computational units.

At $We = 32000$

Parameters	Case 1	Case 2	Case 3	Case 4	Case 5
Viscosity Ratio : Liquid/Gas	0.2/0.002	0.1/0.001	0.05/0.0005	0.04/0.0004	0.03/0.0003
Reynolds Number	50	100	200	250	333
Ohnesorge Number	3.578	1.789	0.8944	0.7156	0.3578

At $Re = 200$

Parameters	Case 1	Case 2	Case 3
Viscosity Ratio : Liquid /Gas	0.05/0.0005	0.04/0.0004	0.03/0.0003
Weber Number	32000	20480	11520
Ohnesorge Number	0.8944	0.7156	0.5367

Table 3-2 Simulation parameters. The viscosity values are in computational units.

CHAPTER 4

-

MODELING THIN FILMS NEAR A SOLID WALL

4.1 Introduction

In the case of a droplet impacting a liquid film, the droplet does not come in actual contact with the solid wall. The liquid film underneath gets squeezed out. The scenario is however different when there is no liquid film. When a liquid drop approaches a wall, the air/vapor film blanketing the wall can become much thinner than the grid spacing near the wall. It is unlikely that the film will disappear. The falling drop will squeeze out the thin film of air as it approaches the wall. This thin film velocity has an effect on the dynamics of the drop. To get a more accurate representation of the drop impact on a solid wall, it is vital to incorporate this phenomenon in the numerical simulations. There are two ways to go about it: one is to reduce the grid size of the entire domain to a point where it is possible to resolve the evolution of the thin film by solving the mass and momentum conservation equations, and the second is to solve the equations at a coarser grid and add in a model that will replicate the thin air film on the drop shape and motion.

To capture the evolution of the film thickness, we use a “thin film” model. In doing so, we assume that all variations along the wall are slow compared to changes taking place across the film and solve the governing equations in integral form for a control volume spanning the thickness of the film. Finer grid would, however, result

in smaller time steps for explicit codes, which would be detrimental to the purpose of producing fast and accurate solutions. This, coupled with the simplicity of the flow in the film suggest that there is an opportunity to capture the behavior near the wall using a wall layer modeled using thin-layer or lubrication theory. The effect of the layer, as obtained in that way, would be feed into the computations of the rest of the motion as a modified boundary condition on the bottom wall.

The use of lubrication theory to model thin layers is quite old and well-documented. Chief sources are Batchelor (1967), Panton (1996) and, Oron, Davis and Bankoff (1997). We will therefore not attempt to review the general thin film literature any further, but instead focus on efforts to use thin films as sub-grid models in numerical simulations.

To emphasize the need for a “thin film” model, the following set of numerical experiments is presented. Figure 4.1 shows a simulation of a drop immersed in a less viscous fluid, released above a sloping wall. The gravity is both perpendicular and parallel to the wall are equal, corresponding to a wall whose slope is 45 degrees. The properties of the fluids and the numerical details are given in the figure caption. The figure shows five frames from the simulation, starting with the initial conditions; two shortly after the drop has impacted the wall; and then two at later times. The drop falls onto the wall and then slides along it, riding on a thin lubricating layer of the ambient fluid. The drop motion has been computed using three different grid resolutions, with 64, 128, and 192 grid points across the vertical dimension of the domain. The 64 grid has evenly spaced grid points, but for the finer grids the points are unevenly spaced in the vertical direction in such a way that the resolution near the wall is almost six times

as fine as near the top of the domain. The results from the two finest resolutions are identical, suggesting that both the drop and the lubrication film are fully resolved. Details of the flow in the film are shown in Figure 4.2, where the velocity in a small section of the film is shown at the same time as in frame three in Figure 4.1. The results are from the computation using the finest grid and there are about eight grid points across the film, showing the linear velocity profile clearly. For the drop resolved on the coarsest grid there is less than one grid point in the thin film. The grid spacing used to resolve the flow in the thin film is much higher than what is needed to resolve the drop itself. We have repeated this simulation using a full slip wall, where resolving the film fully is not critical, and find that the drop motion is essentially fully converged on a grid with only half the number of points used for the coarsest grid. For a solid, no-slip wall, the outcome of a simulation with too few grid points in the film is very different as Figure 4.1 shows. Not only is the drop shape different, but the poorly resolved drop lags behind the fully resolved one. In Figure 4.3 we plot the location of the drop centroid versus time (top) and the minimum thickness of the film (bottom). The drop initially is at rest so it takes it a little while to accelerate but then it slides down the wall with a nearly constant velocity, although there is a slight change in the velocity around time 2.5, presumably corresponding to the change in shape seen between frame three and four in Figure 4.1. The drop with the poorly resolved film moves significantly slower than the better resolved ones, as was already seen in Figure 4.1. The minimum thickness of the film (bottom frame in Figure 4.3) is well predicted by the finer stretched grids. The thickness is reduced as the drop falls to the wall, then it rebounds slightly around time 2 and then the film thickness becomes approximately constant. On the coarse uniform grid, however, the film behaves differently. It does not become as thin as on the finer grids and thus does not rebound

nor reach the correct thickness at later times. We have also run the simulation on a 64 stretched grid, with results similar to those on the finer grids and on a 32 uniform grid where the differences with the fully resolve solution become even greater than on the 64 uniform grid.

Those results suggest that it would be possible to obtain the correct results using relatively coarse grids by refining them near the wall only. Finer grid would, however, result in smaller time steps for explicit codes. This, coupled with the simplicity of the flow in the film, suggest that there is an opportunity to capture the behavior near the wall using a wall layer modeled based on thin-layer or lubrication theories. The effect of the layer, as obtained in that way, should be feed into the computations of the rest of the motion as a modified boundary condition on the bottom wall. In the section 4.3 we derive such a model.

4.2 Problem setup

For the situation simulated here, shown in Figure 4.1, the governing non-dimensional numbers are the Eötvös number $Eo = \Delta\rho g D^2 / \sigma$, the Ohnesorge number $Oh = \mu_f / \sqrt{\rho_f D \sigma}$ and the ratios of the densities $r = \rho_f / \rho_a$ and the viscosities $m = \mu_f / \mu_a$. Here the subscript f refers to the drop and a to the ambient fluid, g is the gravity acceleration, ρ is the density, μ the viscosity and σ the surface tension. The computational domain has a full-slip top and is periodic in the wall-direction. Its height is two drop-diameters and the length is seven drop-diameters.

However, we assume that the height of the domain and its length has only minor influence on the drop dynamics.

4.3 Theory of thin film modeling

The solution strategy, including the thin layer near the wall is this: When the film of air is thick and well resolved the no-slip boundary conditions are used for the air velocity at the wall. When the film becomes too thin to be well resolved by the grid, an equation for the film thickness is solved at the appropriate grid points and the liquid is assumed to reach all the way to the wall. The wall shear is computed from the thickness of the film and the liquid velocity at the wall and used as boundary condition for the liquid. The film thickness is assumed to be so small that it can be ignored for the computation of the liquid motion. However, since the air film provides a lubricating layer for the liquid, the no-slip boundary condition for the liquid that is separated from the wall by a thin air film must be replaced by the condition that the stresses across the liquid-air interface must be continuous.

At every time step, it is checked whether the drop goes below the grid resolution at the wall. The staggered grid at the bottom wall is shown in Figure 4.4. The difference between the $j + 1/2$ and $j + 3/2$ nodes gives the grid resolution at the wall. Once the front (or the drop) is below the $j + 3/2$ node, the model is activated.

Figure 4.5 shows a schematic of the position of the thin layer in the model with respect to the grid and actual position of the front. It may be worth repeating that, as the position of the front is in the sub-grid level, the velocity obtained from the model will not be used to explicitly track the front.

The mass conservation equation for the thin layer, in axisymmetric flow is,

$$\frac{\partial h}{\partial t} + \frac{1}{r} \frac{\partial}{\partial r}(F) = 0 \quad (4.1)$$

where, h is the thickness of the thin film, and

$$F(x) = \int_0^{h(x)} u(y) dy \quad (4.2)$$

$F(x)$ is the net volume flux in the film at location x . To determine the velocity profile in the film it is, in principle, necessary to solve the momentum in the film. Here, however, we avoid doing so by explicitly assuming that the shear across the film is constant. This is equivalent to assuming that the velocity profile is linear.

For a linear velocity profile, the mass flux can be written as,

$$F = \int_0^{h(x)} u(y) dy = \frac{1}{2} U_f h \quad (4.3)$$

where, U_f is the velocity at the interface of the drop of fluid and the surrounding air.

The mass conservation will now be

$$\frac{\partial h}{\partial t} + \frac{1}{2r} \frac{\partial}{\partial r}(hU_f r) = 0 \quad (4.4)$$

The momentum equation for the flow in the thin film is given by

$$\rho_a \frac{\partial u}{\partial t} + \rho_a \frac{1}{r} \frac{\partial}{\partial r}(u^2) = -\frac{dp}{dx} + \mu \frac{\partial^2 u}{\partial x^2} \quad (4.5)$$

The above equation is in axisymmetric formulation and the surface tension term is ignored. Integrating the above equation over the film results in :

$$\rho_a \frac{1}{2} \frac{\partial}{\partial t} (h U_f) + \rho_a \frac{1}{3r} \frac{\partial}{\partial r} (r h U_f^2) = - h \left(\frac{1}{r} \frac{\partial}{\partial r} (r p) \right)_f \quad (4.6)$$

The pressure gradient above is given by the pressure in the fluid. Let us define q which is,

$$q = U_f h \quad (4.7)$$

In terms of q and h , we can rewrite the (1) and (6) as

$$\frac{\partial h}{\partial t} = - \frac{1}{2r} \frac{\partial}{\partial r} (r q) \quad (4.8)$$

$$\frac{\partial q}{\partial t} = - \frac{2}{3r} \frac{\partial}{\partial r} \left(\frac{r}{h} q^2 \right) - \frac{2h}{\rho_a r} \left(\frac{\partial}{\partial r} (r p) \right)_f \quad (4.9)$$

Approximating the advection terms using upwind and assuming positive flow, we can write (4.8) and (4.9) in the finite difference formulation as,

$$h_i^{n+1} = h_i^n - \frac{\Delta t}{2 r_i r_{\xi_i}} (r_{i+1/2} q_i - r_{i-1/2} q_{i-1}) \quad (4.10)$$

$$\begin{aligned} q_i^{n+1} = & q_i^n - \frac{2}{3} \frac{\Delta t}{r_{i+1/2} r_{\xi_i}} \left(\frac{r_{i+1/2} q_i^2}{h_i} - \frac{r_{i-1/2} q_{i-1}^2}{h_{i-1}} \right) \\ & - \frac{\Delta t}{r_i r_{\xi_{i+1/2}}} \frac{h_i}{\rho_a} (r_{i+1} p_{i+1,2} - r_{i-1} p_{i-1,2}) \end{aligned} \quad (4.11)$$

From the value of q_i^{n+1} obtained from the above equation, the velocity in the film will be,

$$U_{f_i}^{n+1} = \frac{q_i^{n+1}}{h_i^{n+1}} \quad (4.12)$$

The shear stress in the film is

$$\tau_w = \mu_a \left. \frac{\partial u}{\partial y} \right|_a \quad (4.13)$$

By assuming that the film is thin enough that the velocity profile is linear, we get the shear stress

$$\tau_w = \mu_a \frac{U_f}{h} \quad (4.14)$$

This shear stress in the film is equal to the equal to shear stress close to wall without the presence of the film.

$$\tau_w = \mu_a \left. \frac{\partial u}{\partial y} \right|_a = \mu_f \left. \frac{\partial u}{\partial y} \right|_f \quad (4.15)$$

On rearranging the terms,

$$\left. \frac{\partial u}{\partial y} \right|_f = \frac{\mu_a}{\mu_f} \left. \frac{\partial u}{\partial y} \right|_a \quad (4.16)$$

Just as a note, if $\frac{\mu_a}{\mu_f} \rightarrow 0$, then the wall condition would then be full slip. The

expression for shear stress in the liquid close to the wall can be expanded as,

$$\tau_w = \mu_f \frac{U_f - U_g}{h} \quad (4.17)$$

where U_g is the ghost velocity in the staggered mesh at the lower boundary. The staggered mesh at the bottom wall (or boundary) is shown in Figure 4.4.

From (4.13) and (4.17), the ghost velocity is

$$U_g = -\frac{h \tau_w}{\mu_f} + U_f \quad (4.18)$$

The ghost velocity obtained from the model is then used in solving the momentum equation at the next time step. The computational procedure can be summarized as:

1. Given h and U_f , the wall shear stress, τ_w can be found and subsequently the ghost velocities can be set by (4.18). For the points outside the film, the no-slip conditions hold true.
2. Solve the Navier-Stokes equations for the velocity and pressure at the next time step using the ghost velocities set above.
3. Integrate equations (4.11) using the pressure from the wall obtained from the Navier-Stokes solution.
4. Go to step 1.

The linear velocity profile that we have used works well for clean fluid interfaces where the drop surface is mobile. For more complex problems, such as contaminated surfaces or surfaces where thermocapillary effects are important, a more complex velocity profile is needed.

4.4 Results and Discussions

Before extending the model to the more complex sliding wall, it is tested for a drop impact on a horizontal solid wall. A drop of diameter $D = 0.5$ (in computational units) is moving with an initial downward velocity, $U = 1.0$, and from a height of a tenth of the drop diameter. The non-dimensional numbers are $Re = 100$ and $We = 50$. Under these conditions, we observe spreading and then oscillations of the drop. For our study, only the portion till the maximum spread of the splat is considered. The progress of the drop is shown in Figure 4.6. At time $t^* = 1.0$ the maximum spread is reached, where $t^* = \frac{t}{UD}$.

The full simulation of the drop is run at a minimum uniform grid resolution of 0.001. The velocities in the thin air film are captured in detail and the velocity profiles are well-resolved. The velocity profiles close to the wall at time $t^* = 1.0$ is displayed in Figure 4.7. The velocity profiles consistently show a linear profile, which justify its usage in the numerical formulation. The simulations are run at a grid resolution of 32×32 with a minimum grid size of 0.0325. Then, the model is incorporated at this coarse grid and then the results are compared with the full simulations at the highest resolution discussed above. The drop shapes are compared at three times, $t^* = 0.2, 0.5$ and 1.0 (Figure 4.8). It can be clearly seen that there is a difference in the morphology of the drop at different grid resolutions. Also, the model is remarkably close to the full simulations. A close-up view of the drop shape can be seen in Figure 4.9. This illustrates the accuracy of the model in estimating the velocity in the thin film of air.

The drop shape is irregular, so quantifying the effectiveness of the model over the coarse grid simulations is tricky. Figure 4.10 (Top) shows the comparison of the spread radius of the drop for the three cases against time. The model shows almost complete agreement with the full simulations over the entire time period. Figure 4.10 (Bottom) is the plot of drop height over time, and the values concur. The purpose of adding in the model is to reduce the computational time required for the simulations. The model at the coarsest resolution runs more than 70 times faster than the highest resolution full simulations.

To reiterate how well the theory outlined above works in practice, we also apply it to the case shown in Figures 4.1-4.3, where we have selected the governing

parameters in such a way that it is possible to resolve the flow in the film on a grid that is reasonably fine, with only modest computational effort. In computational units, we use $\rho_f = 2.5$, $\rho_a = 0.25$, $\mu_f = 0.05$, $\mu_a = 0.005$, $g_x = g_y = 1.0$ and $D = 0.5$, resulting in $EO = 7.955$, $Oh = 0.1414$ and $r = m = 10$. Figure 4.11 shows the drop at the last three times from Figure 4.1 when there is a significant difference between the drop resolved on the fine and the coarse grids. We show the fully converged solution from the stretched finest grid, the results from the coarse uniform grid and then the results from the coarse uniform grid, but with the model described in the last section used to compute the flow in the film. Although the model results are not identical to the fully converged solution, it is clear that the results are much closer to those, than to the original coarse grid results. This improvement is also seen in Figure 4.12, where we plot the location of the centroid (top) and the minimum film thickness (bottom). Here the model results are essentially identical to the fully converged results and much better than the original results from the coarse grid.

The conditions for the simulation in Figures 4.1-4.3 and 4.11-4.12 were selected such that the film between the drop and the wall was relatively thick, and we could therefore fully resolve it on a fine enough grid. The real need for the model is, however, for films that are much thinner. The film will generally become thinner for both less and more deformable drops. For less deformable drops less air is trapped between the drop and wall and for more deformable drops the film will have more time to drain. In Figures 4.13 and 4.14, we have increased the gravity acceleration perpendicular to the wall by a factor of four so that the slope of the wall is about 14 degrees. The viscosity has also been reduced by twenty percent. Figure 4.13 shows result using the model for a case where the drop is deformable ($\sigma = 0.2$) and in Figure

4.14 we simulate a drop with ten times higher surface tension that remains nearly spherical. In frames (a) we compare the drop shape as computed on a 64 uniform grid, with and without the model. In (b) we plot the location of the centroid versus time and in (c) the evolution of the minimum film thickness is plotted. In both cases we see that there is a significant difference between the results with and without the model. The drop without the model moves significantly slower than when the model is used (b) and the film becomes thinner when the model is used (c). Notice that the film becomes considerable thinner than the minimum grid spacing ($\Delta y = 0.0156$), even when the model is not used. Since the film thickness now becomes much thinner than in the case shown in Figures 4.1-4.3, we have not attempted to do a grid refinement to obtain a fully converged solution and the purpose of this test is only to show the influence of using the model. However, given the results of the original test case, we expect that using the model will get us much closer to the fully converged solution.

Here, we are working exclusively with physical systems described by the Navier-Stokes equations. We therefore take a fully converged numerical solution to be the “truth” and validate the thin film model by comparison with a fully converged solution.

4.5 Conclusions

A method is introduced to account for thin films trapped between a drop and a solid wall in front tracking simulations, without the need for local adaptive grid refinement. It is based on solving an equation for the evolution of the film in parallel with computing the large-scale evolution. The equation governing the evolution of the

film is based on standard assumptions used for thin film modeling and uses information from the large-scale simulations to drive the film flow. The results from the thin film are, in turn, used to modify the wall-boundary conditions for the large-scale flow. The model is designed to “kick-in” only when needed (when the film thickness becomes smaller than single grid spacing) and a refinement of the grid used for the large-scale solution will either delete or eliminate the use of the thin film model automatically. Since the model is activated once the film is thin enough it is, however, possible that too poor of a large scale resolution will result in the film never becoming thin enough to activate the model.

For the particular cases examined here, drops moving next to a wall, we expect the importance of modeling the thin film to depend strongly on the specifics of the situation. For a bubble sliding along the wall, for example, where the film is essentially stationary, we would expect the effect to be small. Although we have derived and tested the thin film model here for a very specific situation, we expect that the approach is more general and that it can be extended to other situations where thin films form.

As we go to smaller and smaller scales, we eventually reach a point where it is no longer fully justified to assume that the usual continuum hypothesis is accurate. It is then necessary to either change the modeling approach completely by, for example, using molecular simulations or possibly something like the dissipative particle dynamics approach, or work with modified continuum formulations designed to account for small scale effects. See Koumoutsakos (2005) and Nie, Chen, and

Robbins (2004) for recent attempts to couple molecular dynamics with continuum simulations.

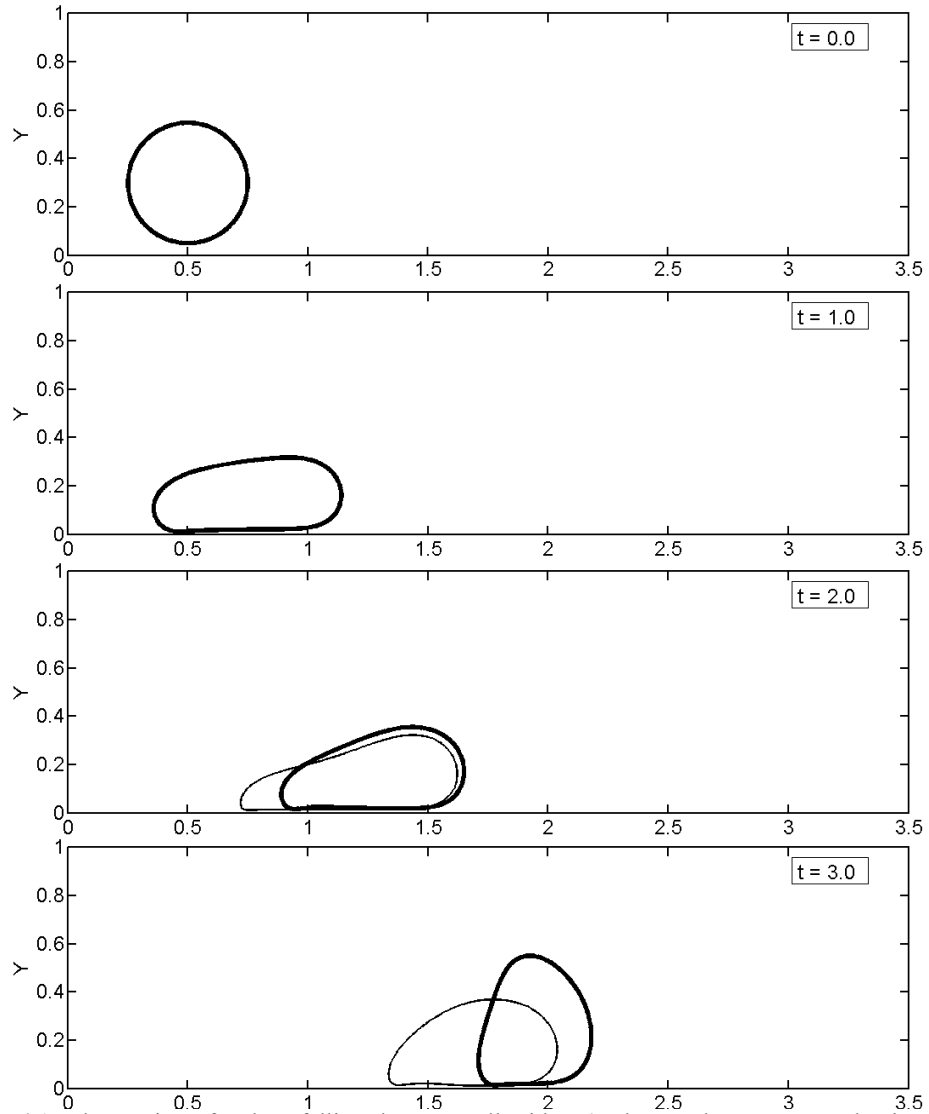


Figure 4.1: The motion of a drop falling down a wall with a 45 degree slope, computed using three different resolutions as described in the text. The thick line is fully converged results computed on two fine stretched grids. The results shown by a thin line are computed on a coarse uniform grid.

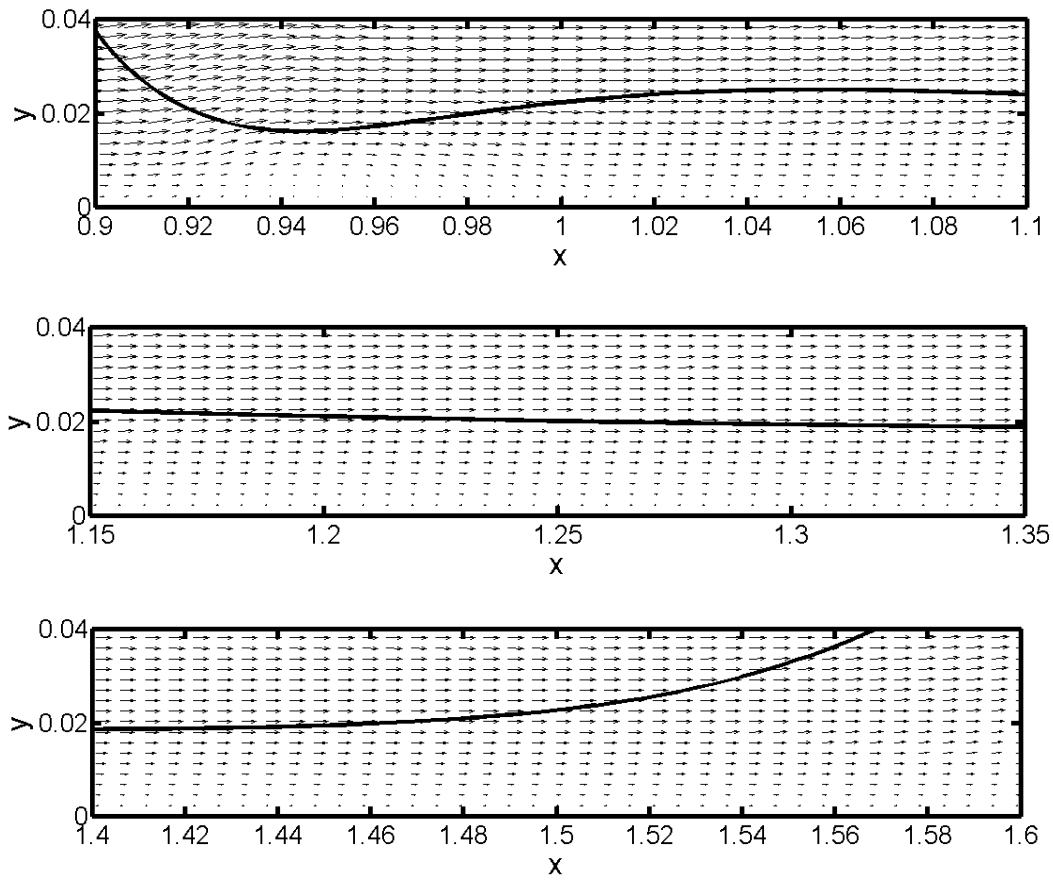


Figure 4.2: The flow in the thin film, corresponding to the third frame in figure 1, as computed on the finest grid. The top frame shows the flow near the back of the drop, the middle frame shows the flow in the middle and the bottom frame shows the flow near the front.

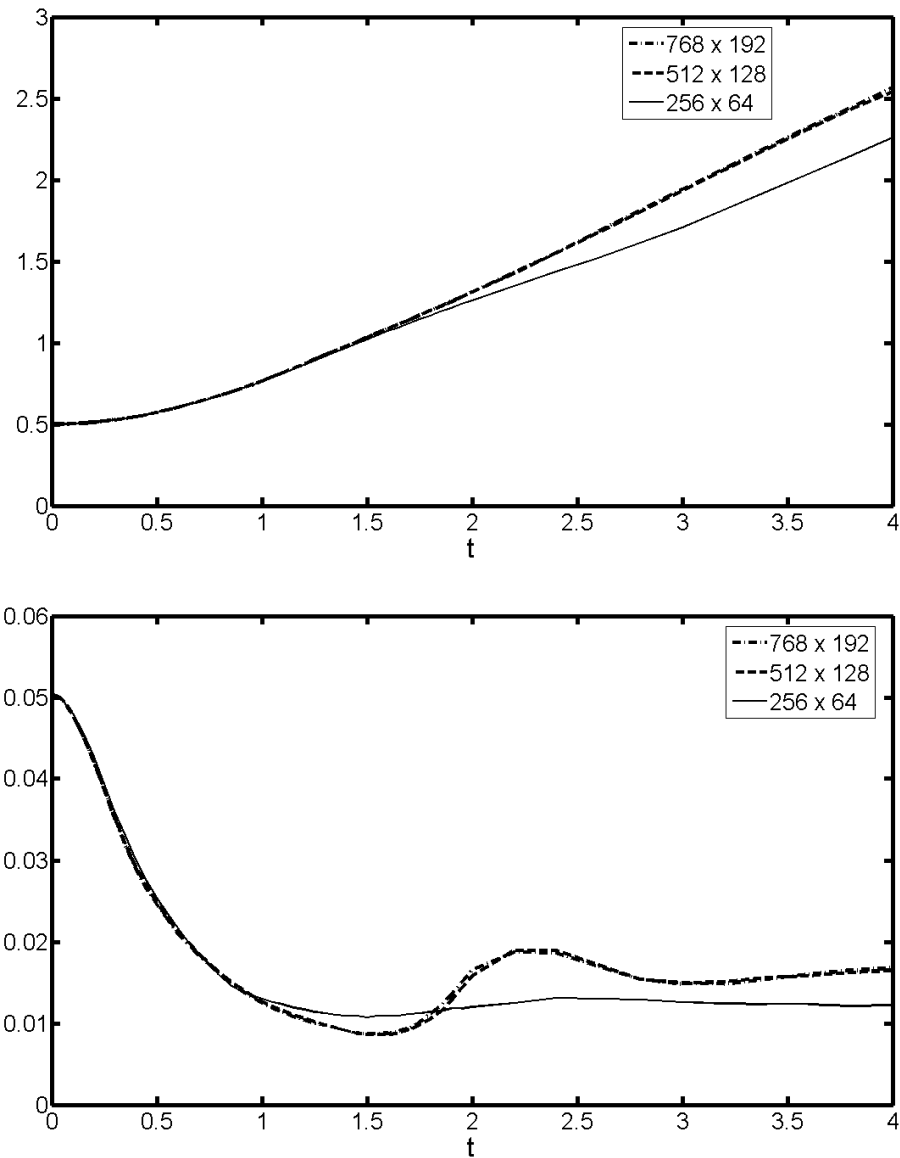


Figure 4.3: The location of the drop centroid versus time (top) and the minimum thickness of the film (bottom) for the simulations shown in figure 1, computed on two stretched fine grids and a coarse uniform grid.

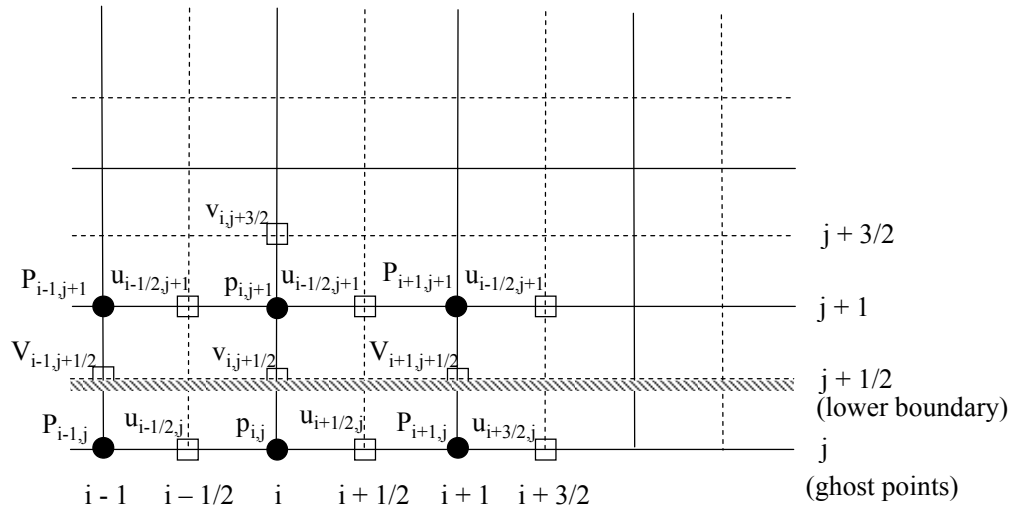


Figure 4.4: Staggered grid at the bottom wall. The u -velocity at the wall is obtained by the interpolation of the velocities at the ghost point and its corresponding point at the next y -location.

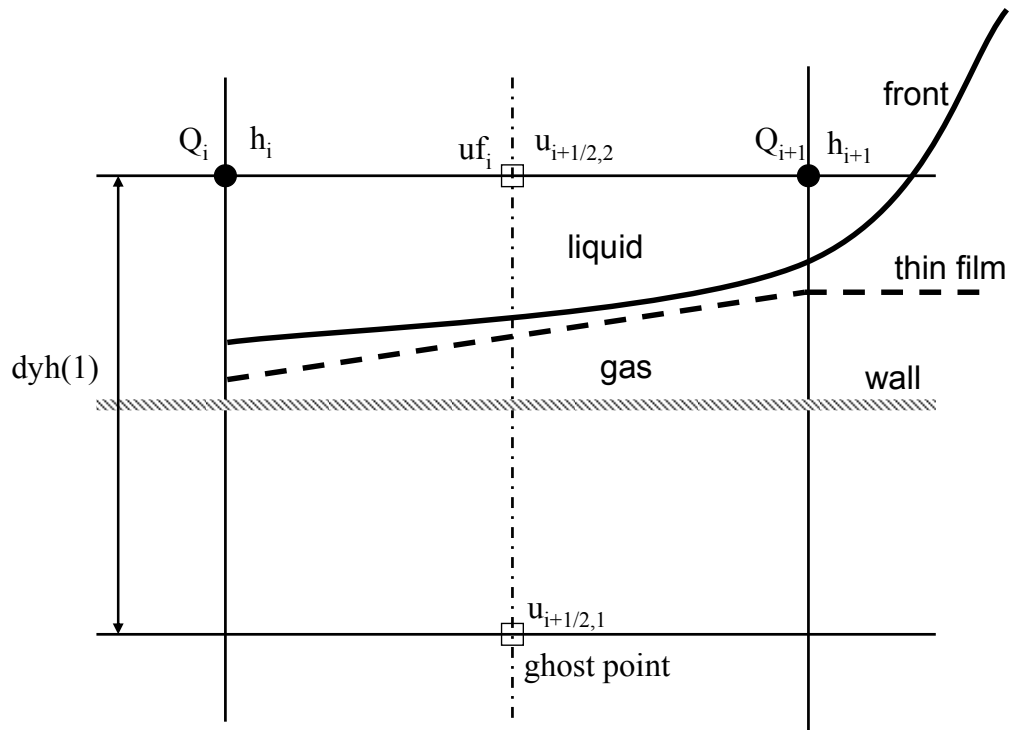


Figure 4.5: Sketch of the profile of the thin film model in relation to the front and the staggered grid. The Q and h values are evaluated at the pressure nodes, while u_f is calculated at the u -velocity nodes.

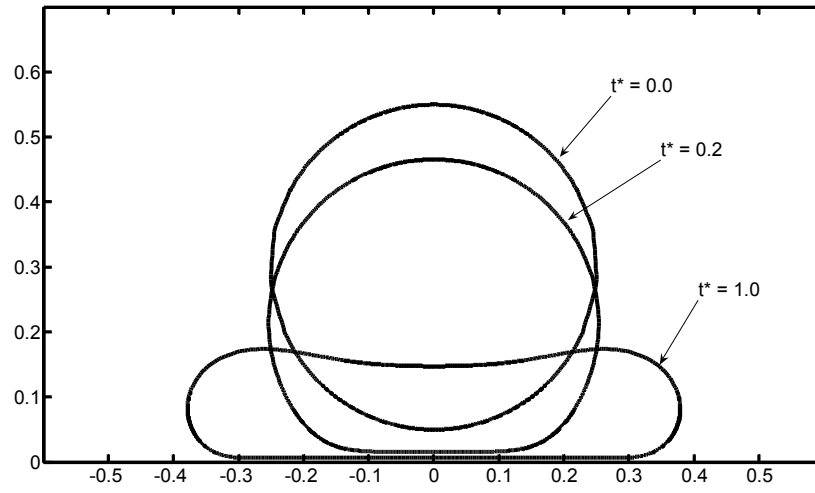


Figure 4.6: Spreading of the droplet on a solid surface. Time $t^* = 1.0$ is the point at which the drop is at its maximum spread. $Re = 100$, $We = 50$.

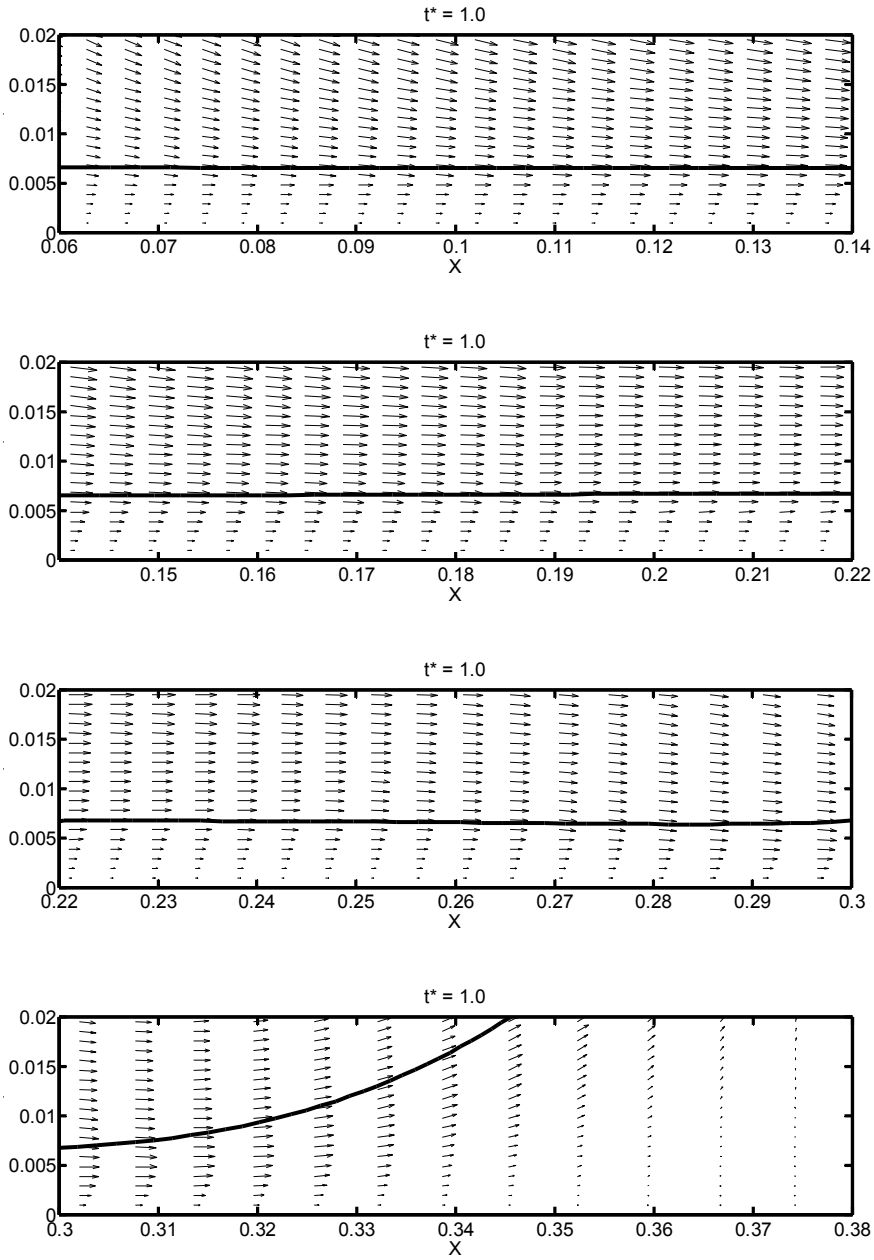


Figure 4.7: Close-up of the front near the wall during the full simulations at $t^* = 1.0$. The minimum grid size close to the front is 0.001. The X-axis values over the three figures range from 0.06 to 0.38. Note that at the maximum spread position, the velocity vectors are smaller in size, indicating the end of its outward motion.

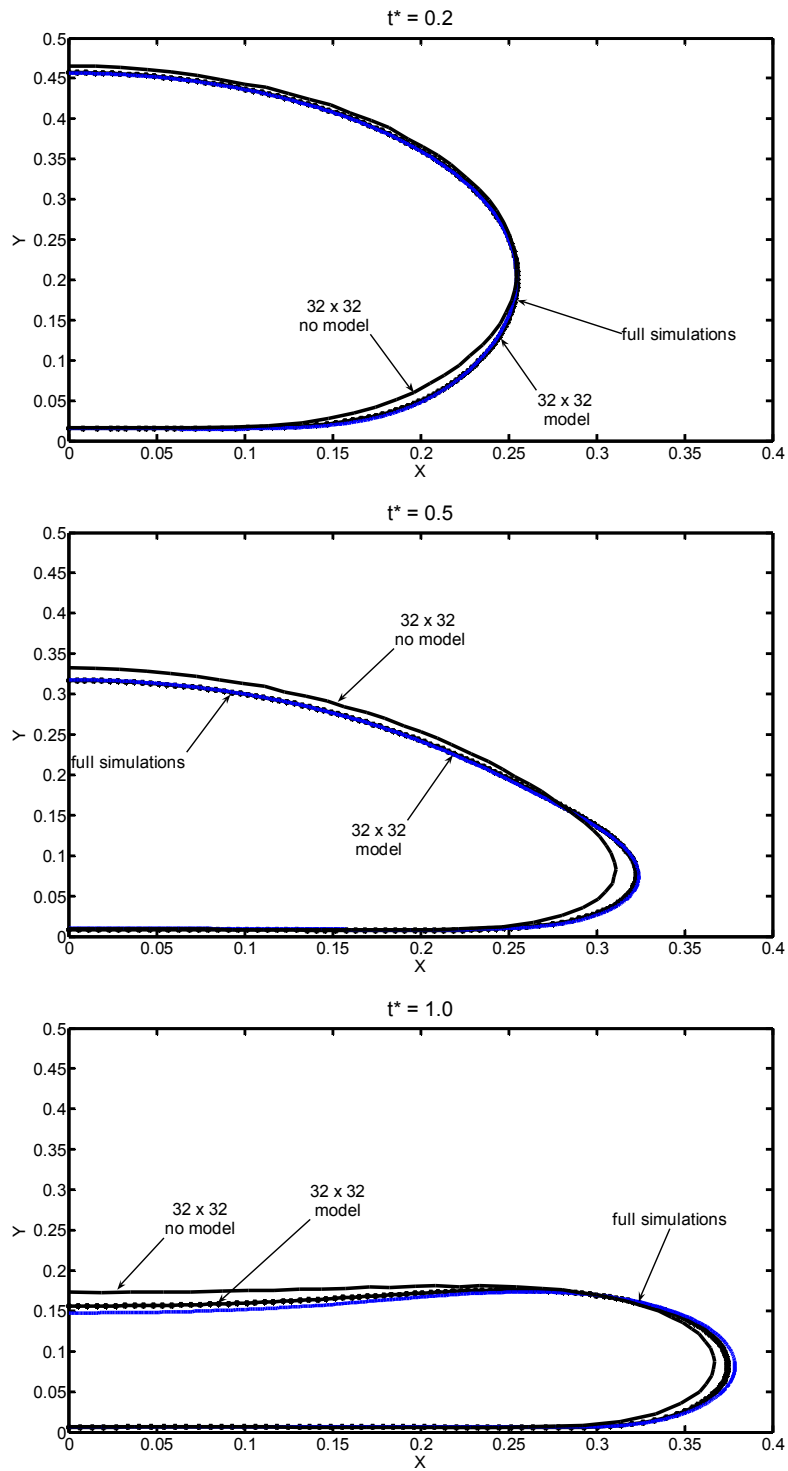


Figure 4.8: Comparison of the shape of the splat at different times ($t^* = 0.2$, $t^* = 0.5$ and $t^* = 1.0$) for the model, coarse grid and full simulations.

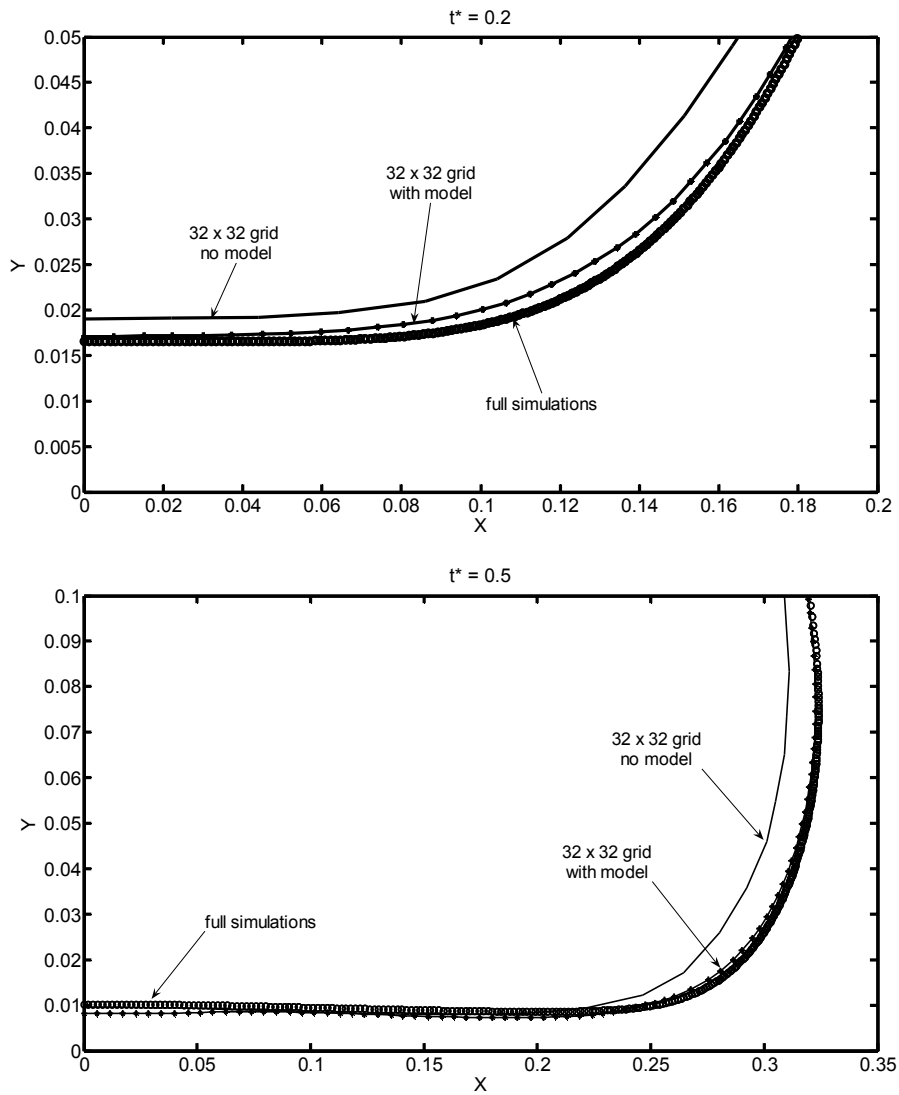


Figure 4.9: Close-up views of the splat, highlighting the difference between the model and the coarse grid simulations.

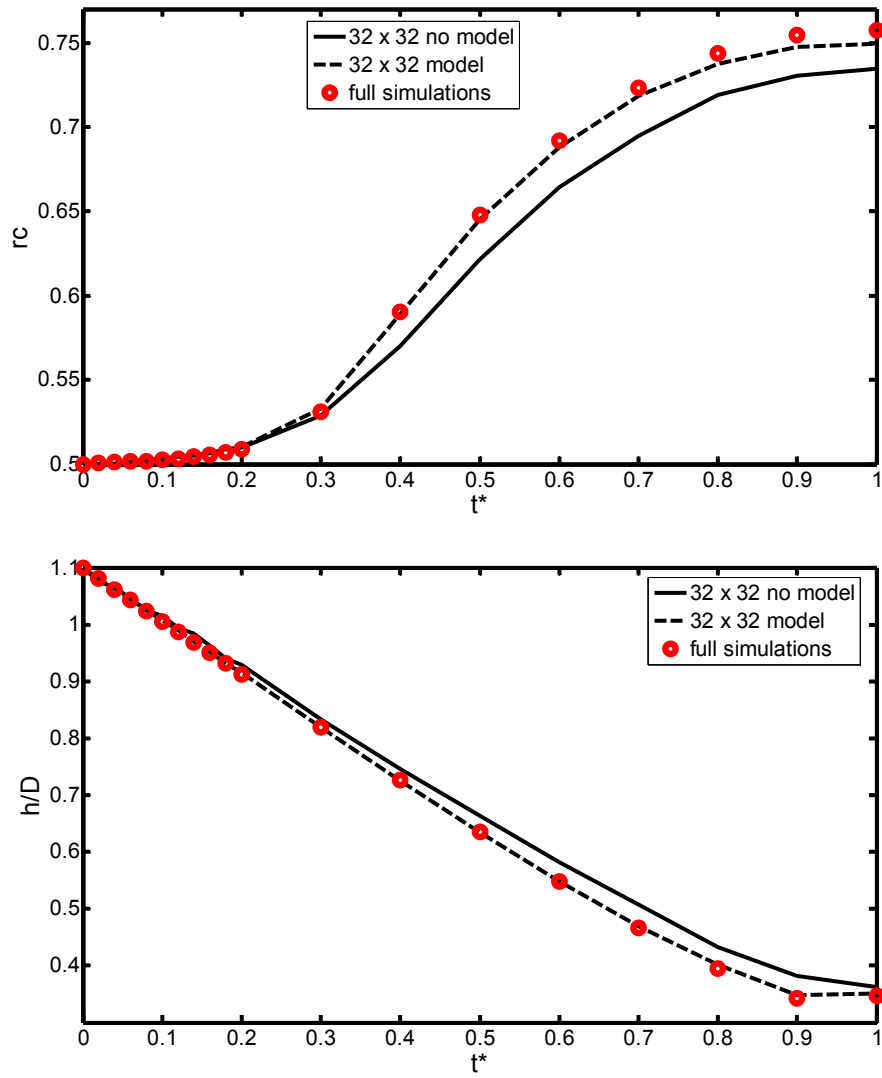


Figure 4.10: (Top) Drop spread radius comparison for the model, coarse grid and the full simulations. (Bottom) Drop height comparison for the model, coarse grid and the full simulations.

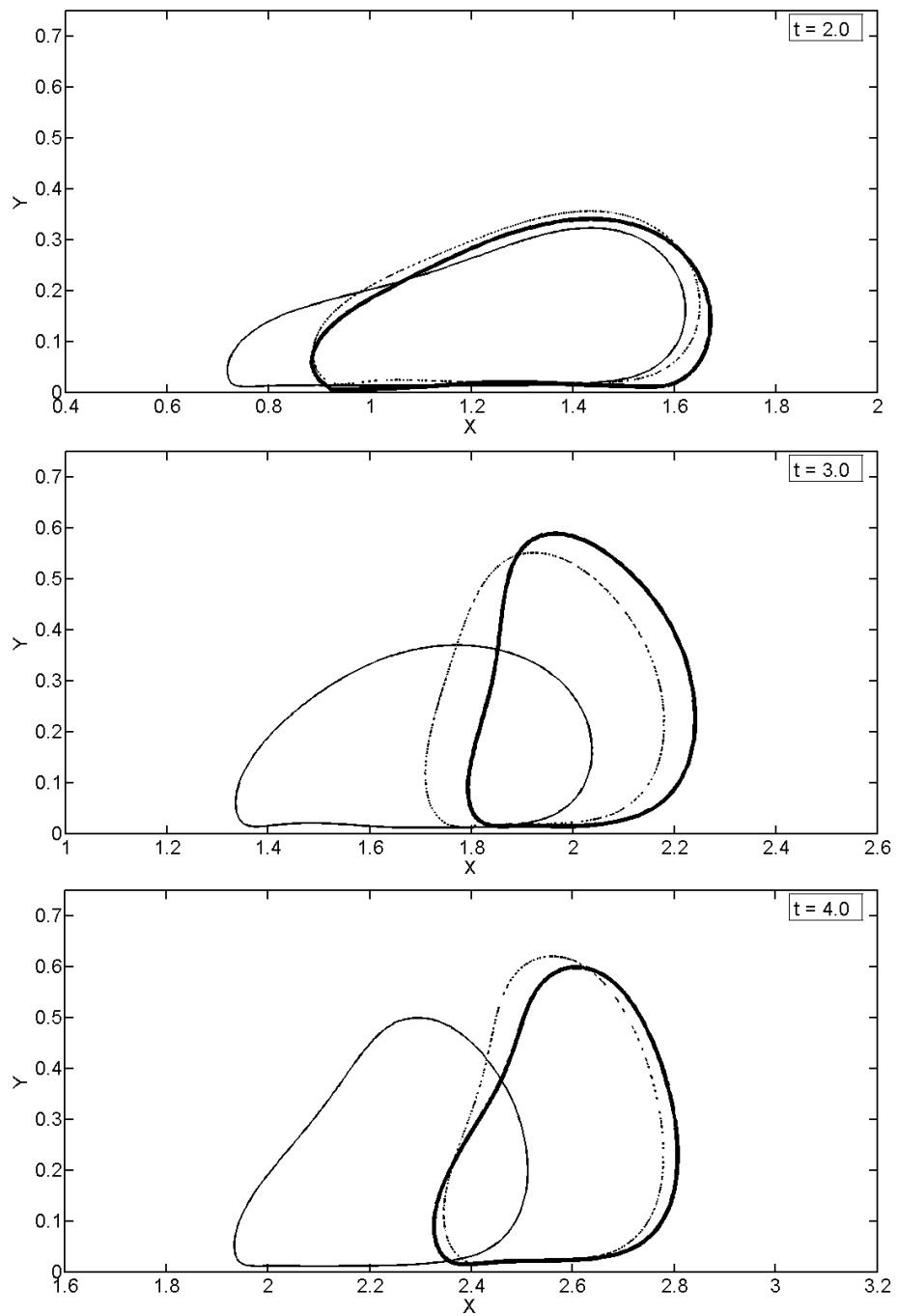


Figure 4.11: Comparison of results from simulations on a coarse grid using the wall-film model (dashed line), with direct numerical simulations using the coarse grid without the model (thin line) and the fine stretched grid (thick line) at three times. The coarse grid results with the film model agree reasonably well with the results using the fine grid.

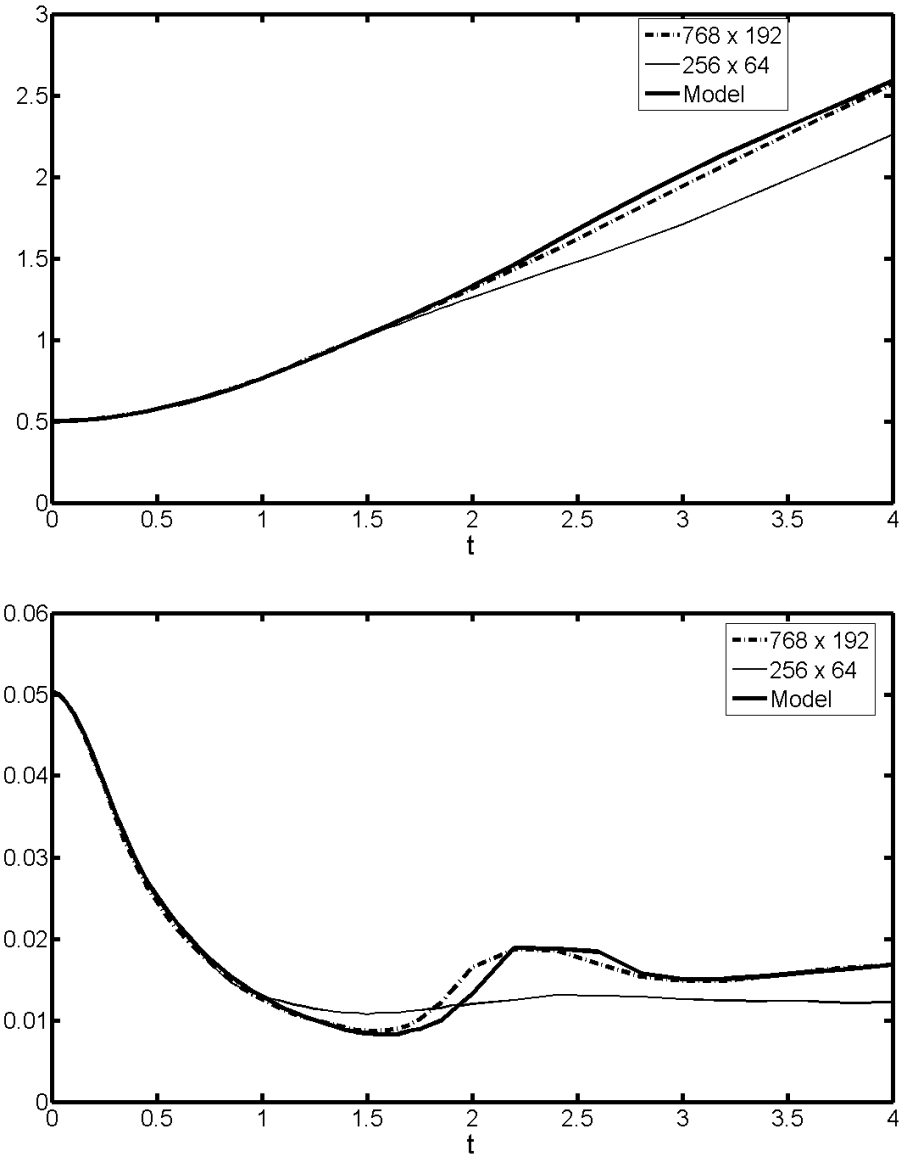


Figure 4.12: The location of the centroid of the drop (top) and the minimum thickness of the film near the wall as computed a coarse grid using the wall-film model (dashed line), with direct numerical simulations using the coarse grid without the model (thin line) and the fine stretched grid (thick line) at three times. The coarse grid results with the film model agree reasonably well with the results using the fine grid.

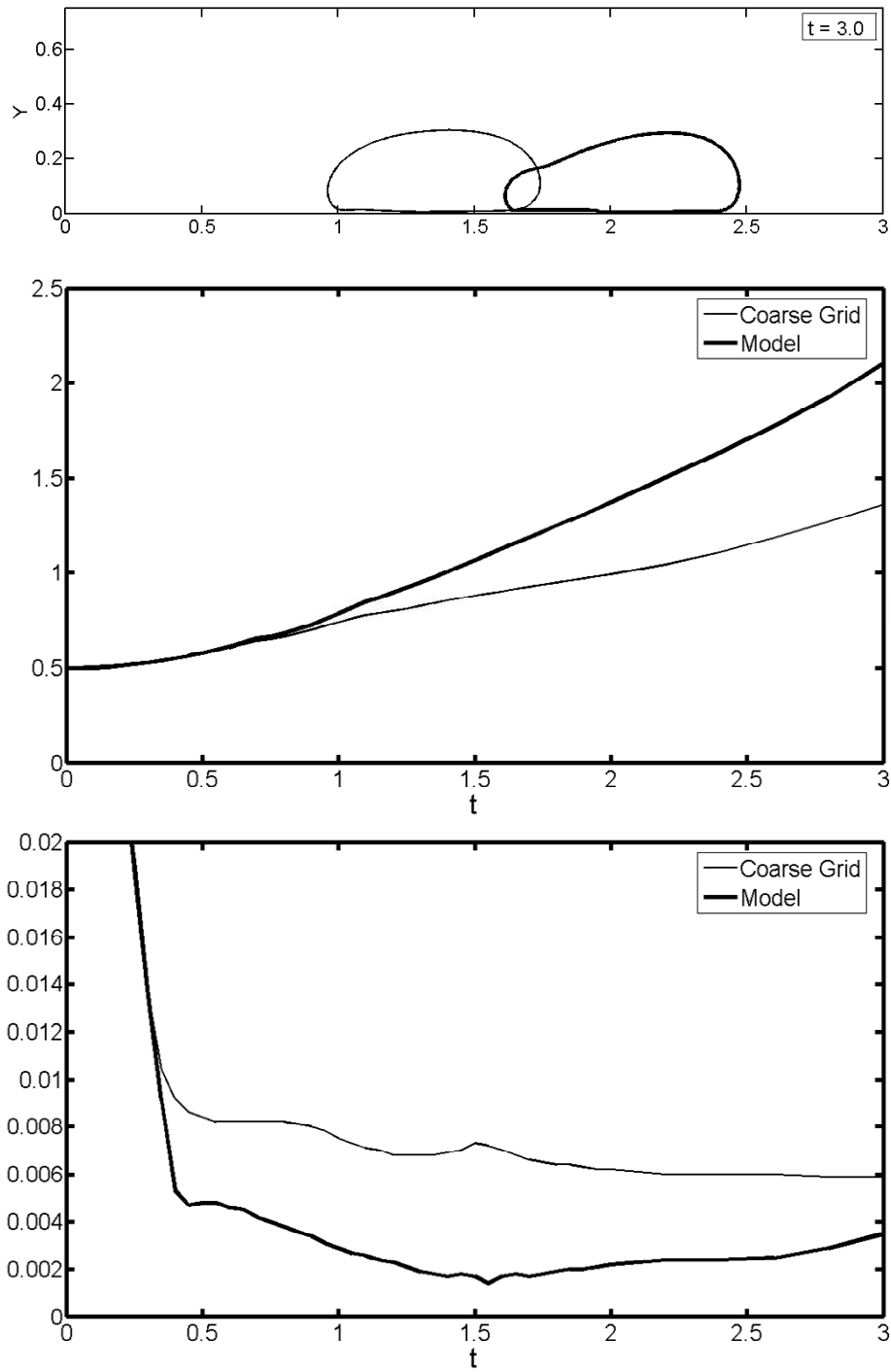


Figure 4.13: Motion of a drop computed on a coarse grid with and without the wall-model (top). Location of the centroid of the drop over time (middle). The minimum thickness of the film near the wall (bottom). The thick line denotes results with the wall-model and the thin lines is results without the model.

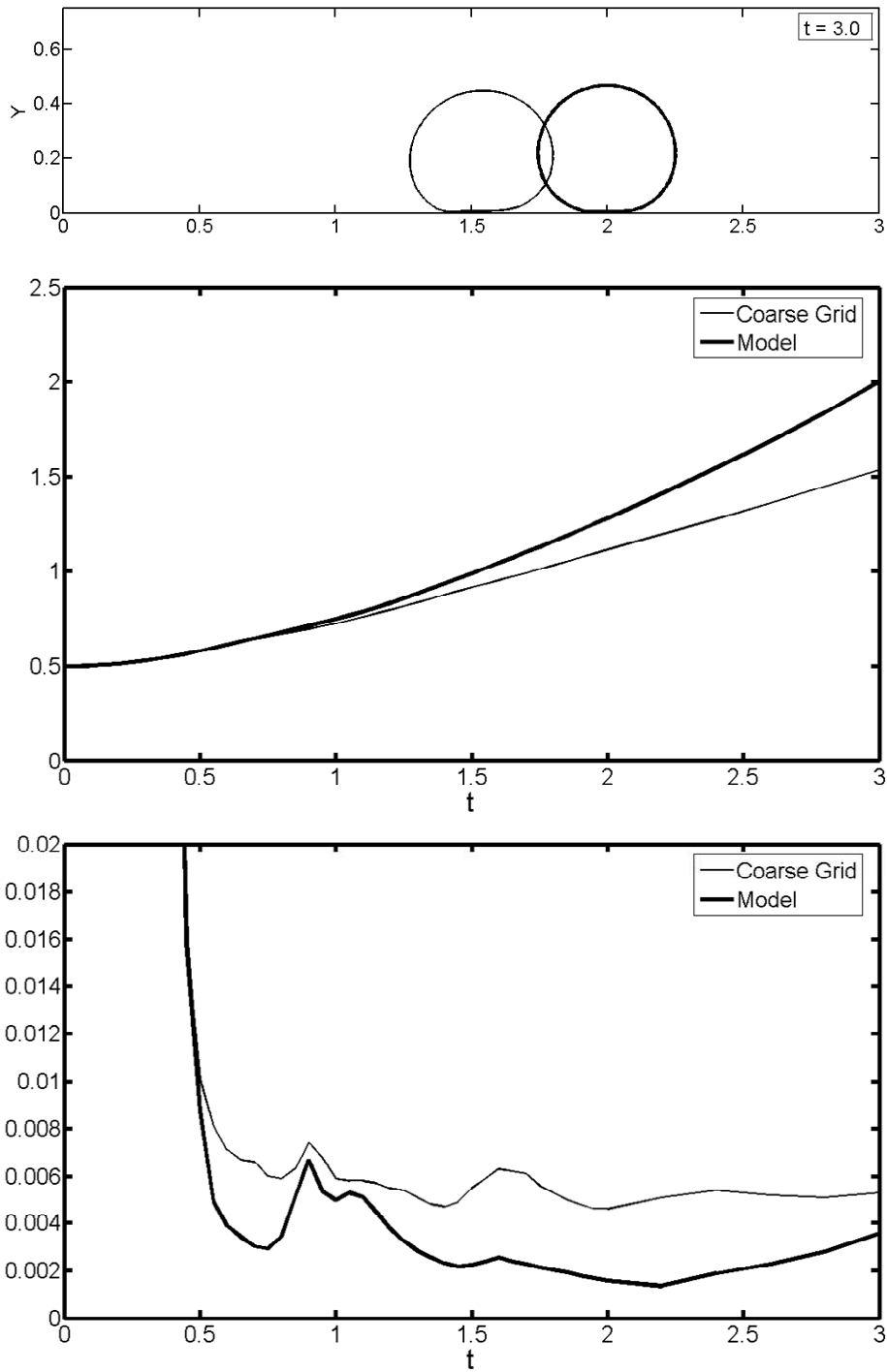


Figure 4.14: Motion of a drop computed on a coarse grid with and without the wall-model (top). Location of the centroid of the drop over time (middle). The minimum thickness of the film near the wall (bottom). The thick line denotes results with the wall-model and the thin lines is results without the model.

CHAPTER 5

-

MICROLAYER MODELING IN NUCLEATE BOILING

5.1 Introduction

Boiling is a phase transformation process where the vapor bubbles form and grow in a liquid usually at its saturation temperature. It is an efficient form of heat transfer as the energy absorbed by the liquid is utilized for the change of phase to vapor. Pool boiling refers to the boiling at the surface of a body immersed in a large pool of liquid, when the liquid is not moving initially. As the vapor bubble grows, the liquid is set into motion. The driving force behind the liquid motion is due to the buoyancy effects. The quenching process in metallurgy, tube-and-shell evaporators, cooling of electronic components and boiling of water are examples of pool boiling. Nucleate boiling is a region in the pool boiling regime characterized by high heat fluxes and low temperature differences.

The incipience of nucleate boiling is indicated by the presence of a vapor bubble at a nucleation site in a pool of quiescent liquid. The bottom wall is at a higher temperature than the liquid and due to the transfer of heat, the vapor bubble grows in size. Once it reaches a size that is unstable, it detaches and rises to the top. The position of the departing bubble is usually occupied by a smaller, nucleating bubble. The microlayer is a thin, small region of liquid that is present under a growing vapor

bubble. The microlayer cannot be observed directly, as it is present at the base of the vapor bubble.

Early studies on boiling concentrated on simulating film boiling. For several practical applications, it is necessary to follow the nucleate boiling from a nucleation site for a sufficiently long time so that meaningful average behavior can be found. The main challenge for such simulations is to be able to capture the evaporation of the microlayer left behind on the wall as the vapor bubbles grow. To capture the evaporation of the microlayer left behind as the base of the bubble expands we use a semi-analytical model that is solved concurrently with the rest of the simulations. The aim of this study is to present a simplified model of the microlayer that will add to the heat transfer. The fluid flow within and around the vapor bubble is simulated in detail and its effect on the heat transfer is examined.

Nukiyama (1966) first developed the basic understanding of the physical processes that occurs during boiling by heating a nichrome wire in a saturated pool of water. He organized the regimes of pool boiling into recognizable categories like partial nucleate boiling, fully developed nucleate boiling, transition boiling and film boiling. As mentioned earlier, fully developed nucleate boiling exhibits a very high rate of heat transfer, which is very suitable for a large number of industrial processes. In this research, only pool boiling is considered. Pool boiling, as opposed to flow boiling occurs in initially stagnant liquid. The fluid flow that occurs later on is due to the growth the vapor bubble. According to Tong et al. (1965), the life of a single bubble can be divided into these phases: nucleation, initial growth, intermediate growth, asymptotic growth and possible collapse. Rohsenow (1962) proposed a

physical model of nucleate boiling as well as a theoretical expression of the heat transfer coefficient.

Cooper and Lloyd (1969) were the first to detect the presence of the microlayer below the vapor bubble by observing the fluctuations in the heater surface temperature. Using the lubrication theory for thin films, they calculated the thickness of the microlayer to be $\delta = 0.8\sqrt{\nu_l t}$. They also deduced analytically the maximum departure diameter of the vapor bubble using a number of assumptions, including a hemispherical shape of the bubble throughout its growth, radius of the bubble and the temperature distribution on the heater surface. Gaertner (1965) and Judd and Hwang (1976) concluded that in the transition regime from partial nucleate boiling to fully developed nucleate boiling, the heat transfer is dominated by evaporation and in partial nucleate boiling, the geometry of the heater. Ohta (1999) provided an estimate for the microlayer thickness by measuring instantaneously the electrical resistance of the liquid film. Lay and Dhir (1995) distinguished between the microlayer and the macro-region by observing the liquid evaporating near the stems of vapor bubble during fully developed nucleate boiling.

Cooper (1969) solved the Rayleigh's equation to obtain a model for the evaporation of the microlayer, by assuming that for most of the growth phase for the toluene bubbles, the rate of growth of a bubble is not very different from the rate of evaporation of the microlayer, provided the bulk liquid is nearly at saturation temperature. By using the equation for heat conduction through the microlayer, and neglecting the thermal capacity of the microlayer, it was also found that the growth of the microlayer predominates the evaporation of the curved surface of the bubble. The

model did not always work for smaller sized bubbles and also did not account for the change in shape and the temperature distribution during growth.

Wayner (1992) found very high values of conduction across thin films. He recognized the long-range intermolecular forces that existed in thin films and built a rigorous analytical contact-line model for phase change. These long-range force equations were immensely useful in developing later models for the microlayer. Prominent among those is the level-set approach taken by Son, Dhir and Ramanujapu (1999), who use an iterative method to solve simultaneously the macro- and micro-regions. The model set forth the theory that the high heat fluxes during nucleate boiling was partially due to the evaporation of the microlayer. In this method too, the contact angle is taken to be static. However, recent numerical studies of the dynamic contact angle by Mukherjee and Kandlikar (2007) have shown that the model of the dynamic contact angle at the bubble base has little effect on the vapor volume growth rate. Mann, Stephan and Stephan (2000) utilized Wayner's theory to study the influence of liquid properties on the heat transfer.

Earlier methods, including Cooper (1969) and Plesset and Zwick (1954) had assumed that the shape of the bubble remains hemispherical, which is not correct. Takata et al. (1998) used the Volume-Of-Fluid (VOF) method to trace the shape of the bubble during its growth and found qualitative agreement with the experimental results. Tryggvason and Esmaeeli (2003 and 2004) employed the front-tracking method to perform computations of explosive boiling and film boiling. Welch and Wilson (2000), with the help of a revised version of the VOF method captured the bubble shape and void fractions for film boiling simulations. Yoon et al. (2001) used

a mesh-free method, the MPS-MAFL (moving particle semi-implicit – meshless advection flow-directed local grid) method to simulate boiling that matched reasonably with the empirical correlations. Other methods to study boiling include: VOF with interface tracking for film boiling by Lakehal et al. (2002); the level-set approach by Juric and Shin (2002, 2005) to simulate nucleate boiling; Tu and Yeoh (2002) used a commercial code, CFX to study subcooled flow boiling (where the liquid temperature is less than the saturation temperature).

Zhao et al. (2002) found through their microlayer model that as the wall superheat (the difference between the wall temperature and the liquid temperature) increases, the local evaporation of the microlayer increases. Das et al. (2006) improved upon Zhao's model by presenting an analytical model that took into account different rates of bubble growth, at the initial and final phases. The problem with the analytical models is that due to the transient nature of the bubble growth, the changing shape of the bubble has proven to be difficult to capture.

5.2 Problem Setup

The setup of the problem is shown Figure 5.1. Due to the limitations of the size of mesh, the simulations have to begin with a small initial bubble. Usually, in actual boiling the nucleating is generated at locations where the heated surface is not smooth, or there are wedges on it (Dhir, 1998). For our analysis, we take the bubble to be pre-existing at time, $t = 0$. The regions associated with the nucleate boiling, including the microlayer and the macro-region can be seen in the schematic, Figure 5.2. The macro-region is a region of liquid near the heated surface and the vapor bubble.

5.3 Governing Equations

Besides the Navier-Stokes equation discussed in the preceding chapters, to account for the heat transfer, the conservation of energy equation is needed. It is of the form,

$$\frac{\partial \rho c T}{\partial t} + \nabla \cdot \rho c \mathbf{u} T = \nabla \cdot k \nabla T + \left(1 - (C_v - C_l) \frac{T_{sat}}{L}\right) \int \dot{q} \delta(x - x_f) dA,$$

where c is the specific heat, T is the temperature, k is the thermal conductivity, \dot{q} is the heat flux and δ is the delta function as described earlier. Now, the heat flux \dot{q} is defined as,

$$\dot{q} = k_l \left. \frac{\partial T}{\partial n} \right|_l - k_v \left. \frac{\partial T}{\partial n} \right|_v.$$

The subscripts l and v represent the liquid and vapor phases respectively. At the initial state, both the liquid and vapor phases are at saturated temperature.

$$T_l = T_v = T_{sat}(p_{sys}).$$

Due to the change in phase, the volume of the vapor in the system increases while there is a corresponding decrease in the volume of the liquid. Since the total mass of the system is conserved, the change of phase is accounted for by,

$$\nabla \cdot \mathbf{u} = \frac{1}{L} \left(\frac{1}{\rho_v} - \frac{1}{\rho_l} \right),$$

where L is the latent heat of vaporization. The velocity due to the phase change is calculated as,

$$V_n = \frac{1}{2} (u_l + u_v) + \frac{\dot{q}}{2L} \left(\frac{1}{\rho_v} + \frac{1}{\rho_l} \right).$$

Now the velocity at the interface can be found by integrating,

$$\frac{dx_f}{dt} = V_n \cdot \mathbf{n}_f.$$

5.4 Microlayer model

To model the evaporation of the thin film left behind as a vapor bubble grows, we will have a reasonably simple model, which can make accurate predictions on the nature of the microlayer. The film is sketched in the Figure 5.3, where the variables involved are also indicated. Initially we will assume that the wall temperature, T_w , is constant and the interface temperature is equal to the saturation temperature, T_f . We also assume that temperature variations in the film parallel to the wall are sufficiently small so that any heat flux along the wall can be neglected. The heat flux through the thin film is therefore given by

$$\dot{q} = k \frac{T_w - T_f}{\delta} = k \frac{\Delta T}{\delta}.$$

This heat is used at the film surface to convert the liquid into vapor. The evaporation of the film reduces its thickness at a rate given by

$$\frac{d\delta}{dt} = - \frac{\dot{q}}{\rho_f L} = - \frac{k \Delta T}{\delta \rho_f L} = - \frac{\beta}{\delta},$$

where L is the latent heat and ρ_f is the density of the liquid. This equation can be

integrated to give $\delta = \sqrt{\delta_o^2 - 2\beta t}$. At a given location, the film evaporates

completely (when its thickness becomes zero) in time, $t_e = \frac{\delta_o^2}{2\beta}$. The velocity of the

outer edge of the film, defined as the place where its thickness becomes δ_o , is given

by U_o , during time t_e , the outer edge moves a distance

$$D = U_o t_e = \frac{U_o \delta_o^2}{2\beta}.$$

Thus, if the velocity of the edge is constant, the length of the film is equal to D . The total heat absorbed by the film evaporation is given by integrating over its length. To do so, we move into a frame of reference moving with the outer edge by replacing time by distance divided by velocity, $t = \frac{x}{U_o}$. Thus, the total heat absorbed by the film is,

$$\dot{Q} = \int_0^D \dot{q} dx = \int_0^D \frac{k \Delta T}{\sqrt{\delta_o^2 - (2\beta/U_o)x}} dx = \frac{k \Delta T}{\delta_o} \int_0^D \frac{1}{\sqrt{1 - (2\beta/\delta_o^2 U_o)x}} dx$$

Carrying out the integration, and substituting for β , we find that the rate of heat absorption due to the evaporation of the microlayer is

$$\dot{Q} = \delta_o U_o L \rho_f .$$

The total vapor volume generated by the evaporation of the film is given by

$$\dot{V} = \frac{\dot{Q}}{L} \left(\frac{1}{\rho_v} - \frac{1}{\rho_f} \right).$$

Since the film length is sufficiently short, we can therefore account for the effect of the microlayer evaporation simply by adding a volume source to the pressure equation (mass conservation) at the wall, next to the outer edge of the film. In principle the boundary condition for the temperature should be changed to T_f where the film is, but since it is short enough, we can neglect that. Thus, no changes are needed for the energy equation. However, when the heat flux from the hot wall is computed, we also need to add the heat absorbed by the evaporation. This affects only the diagnostics, not the actual simulation. The front points away from the wall are

moved by the fluid velocity and the front point on the wall is set by extrapolating from the front points next to it.

5.5 Results and discussion

Given the following set of initial conditions (using arbitrary computational units), $g = 3.0$, $\Delta T = 1.0$, $\rho_l = 2.5$, $\rho_v = 0.25$, $\mu_l = \mu_v = 0.005$, $k_l = 0.07$, $k_v = 0.007$, $c_l = c_v = 1.0$, $L = 100.0$ and $\sigma = 0.5$, where g is the acceleration due to gravity, ΔT is the wall superheat (difference between the wall temperature and the saturation temperature), c_l and c_v are the specific heats for liquid and vapor respectively, L is the latent heat of vaporization and σ is the surface tension. The nondimensional numbers of interest are the Jacob number ($Ja = c \Delta T / L$) and the Prandtl Number ($Pr = \mu c / k$), which are defined using the liquid properties. Here, Figure 5.4 shows the progression of the growth of the vapor bubble, at $Ja = 0.01$ and $Pr = 0.715$. The property ratios and nondimensional numbers are similar to those of cryogenic fluids, like liquefied nitrogen and oxygen. At early times, the bubble moves radially outwards and the motion is slowed down due to surface tension and wall friction. The addition of heat is continuous, so the upper portion of the bubble grows outwards. The upward motion leads to a clockwise vortex formation near the bubble, which gains in strength as the bubble diameter becomes larger. When the strength of the vortex becomes large enough, it induces the base of the bubble to move inwards at a rapid speed. The buoyancy force of the expanded bubble overcomes the surface tension (Dhir, 1999) causing the bubble to depart to the top surface. The contraction of the base of the bubble is swift as compared to the time taken for it to grow to its maximum size.

The temperature fields close to the wall and near the bubbles paint a clearer picture of the difference in the heat transfer rates between liquid and vapor (Figure 5.5). The temperature contours in the vapor phase are bunched close to each other indicating lower heat transfer, while those in the liquid phase are spaced out demonstrating greater heat transfer. The bubble diameter continues to increase prominently in the early to middle part of the growth phase, and in later phase, diameter increases gradually, as the buoyancy forces push the vapor bubble to departure. This is seen in Figure 5.6, where the bubble diameter of the bubble for two different wall superheats ($\Delta T = 1$; $\Delta T = 2$) are plotted over time. The end points for both the lines indicate the point of departure for the bubbles. Lower wall superheat means that more time is needed to the bubble to depart. Both curves exhibit a similarity in the sense that for some time before departure, the diameter is nearly constant. The results from our simulations are compared with a set of experimental observations obtained by Seigel and Keshock (1964) during their study of water boiling (Figure 5.7). The curves show reasonable similarity and demonstrate the universal nature of the bubble diameter evolution during nucleate boiling. The bubble diameters for two different wall superheats ($\Delta T = 2$; $\Delta T = 3$) are displayed.

Figure 5.8 shows the variation of the Nusselt (Nu) number over time during the growth of the bubble. Here, Nu can be written as, $l_o \dot{q} / k \Delta T$, where l_o is the characteristic length. The characteristic length is given by $\sqrt{\sigma / g(\rho_l - \rho_v)}$. For a given run of an experiment the wall superheat, the characteristic length and the thermal conductivities are held constant. Thus, the Nusselt number is a measure of the convective heat flux generated over the time of the run. As the vapor bubble

grows, the heat flux should decrease as the thermal conductivity of the vapor is significantly lesser than that of the liquid. This decrease is reflected in the steady fall in Nu with the passage of time. The rise in Nu over the last part indicates that the contraction of the bubble base is in effect. There is an additional mass of liquid that moves towards the bottom wall due to the clockwise vortex formation at the liquid-vapor interface. Hence there is an increase in the heat flux, and subsequently in Nu too.

Our simulations are compared with the numerical simulations of Juric, Shin and Abdel-Khalik (2005) in Figure 5.9 (Top). Their simulations are for a non-dimensional wall superheat of 21, whereas our cases are for much lower superheats. But the common trend of both sets of results is unmistakable, and provides another validation of the method. The bottom figure refers to the Nusselt number averaged over the entire cycle starting from the incipience of nucleation to the bubble departure plotted for three different wall superheats. It shows that there is a moderate increase in Nu as the wall temperature is raised. For wall superheat of 2, the average increase in Nu is 4.1 %, while in case of a wall superheat of 3, the increase is 5.83 %. Son and Dhir (1999) estimated in their experiments that for a wall superheat of 8 °C, the contribution of microlayer to the total heat flux was 15-20 %.

5.6 Conclusions

The complex phenomenon of nucleate boiling, starting from an initial bubble to its departure is simulated and studied, taking into account the fluid mechanics, heat transfer and the interface dynamics of phase change. The conservation equations of

mass, momentum and energy were solved for the entire domain in an axi-symmetric formulation. No assumption is made of the evolution of shape of the bubble. Detailed information regarding the temperature distributions has also been obtained. It is also observed that the time required for the growth of the bubble far exceeds the time for the contraction. As the vapor bubble grows larger, the amount of heat flux transferred through the surface decreases. As the bubble contracts before departure, there is a dramatic increase in the heat flux indicated by the Nusselt number. The results for the bubble growth and Nusselt number correlations lie close to the experimental correlations found in the literature.

Concurrently with the rest of the simulations, a microlayer model was utilized to capture the effect of the evaporation of microlayer on the overall heat transfer. The model is relatively simple, compared to Dhir's iterative solution, but performs well in predicting the heat flux due to the microlayer evaporation. The model predicts that the contribution of the microlayer is increases slightly with an increase in the wall superheat. The microlayer is seen to contribute about 6 % to the overall heat transfer when the wall superheat is 3.

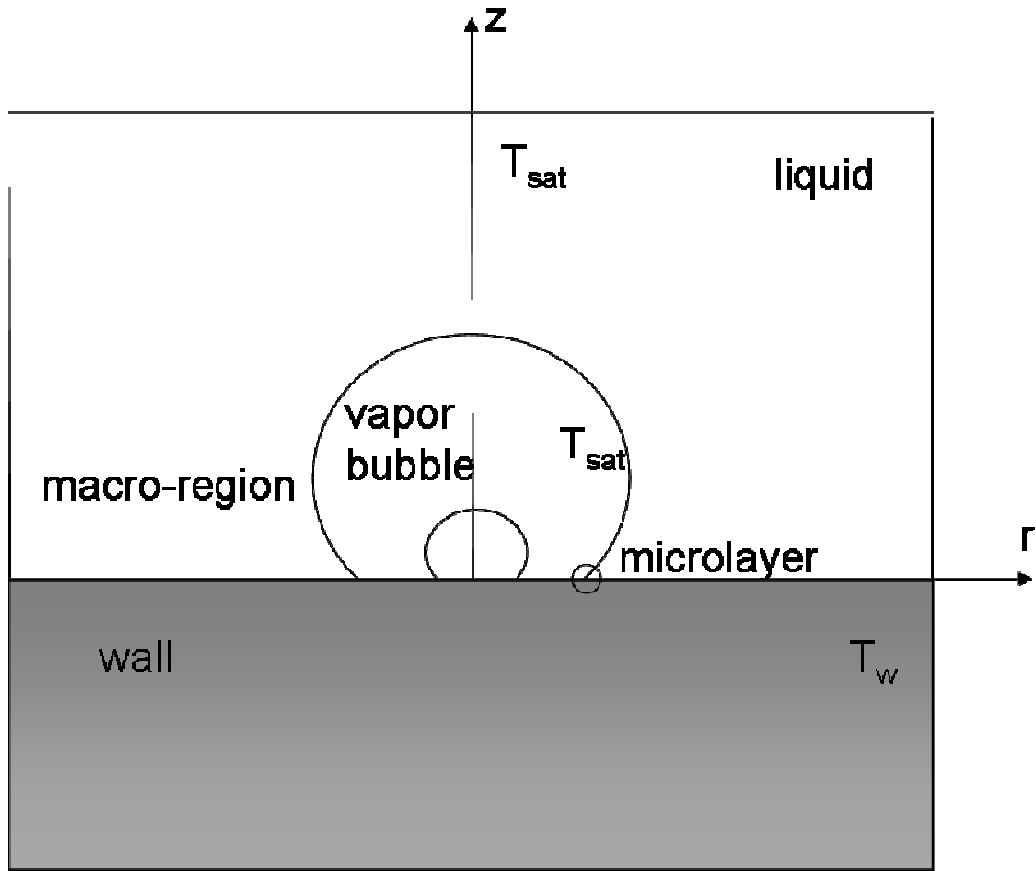


Figure 5.1: Setup of the nucleate boiling problem. The temperature at the liquid-vapor interface is the saturation temperature of the liquid.

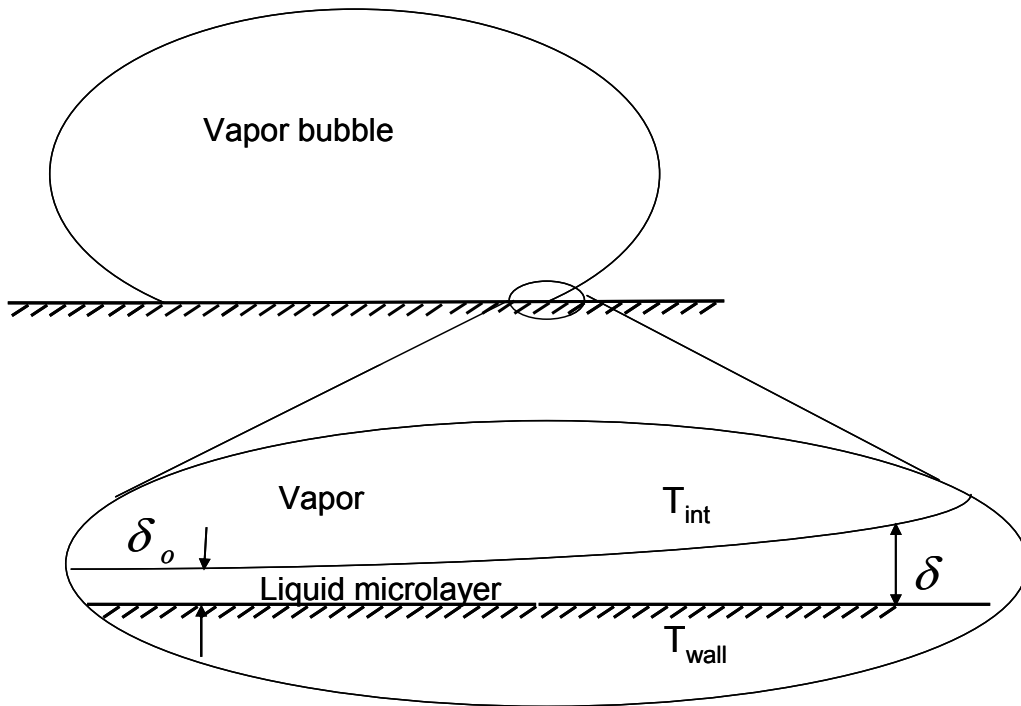


Figure 5.2: Schematic of microlayer.

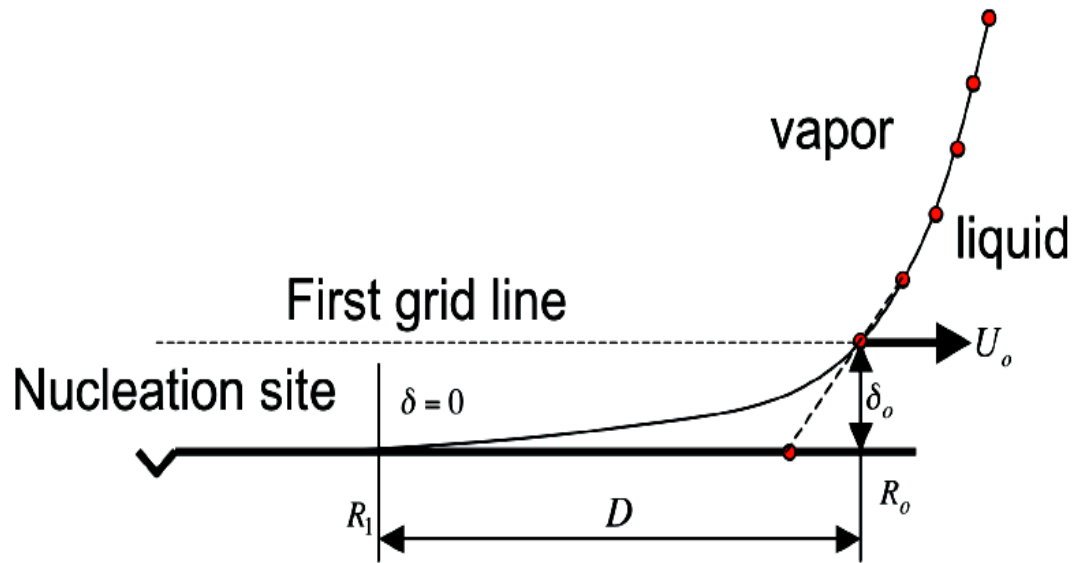


Figure 5.3: Modeling of the evaporation of the microlayer left behind as the apparent contact line moves outward. The location of the point where the front meets the wall is found by extrapolating the front to the wall.

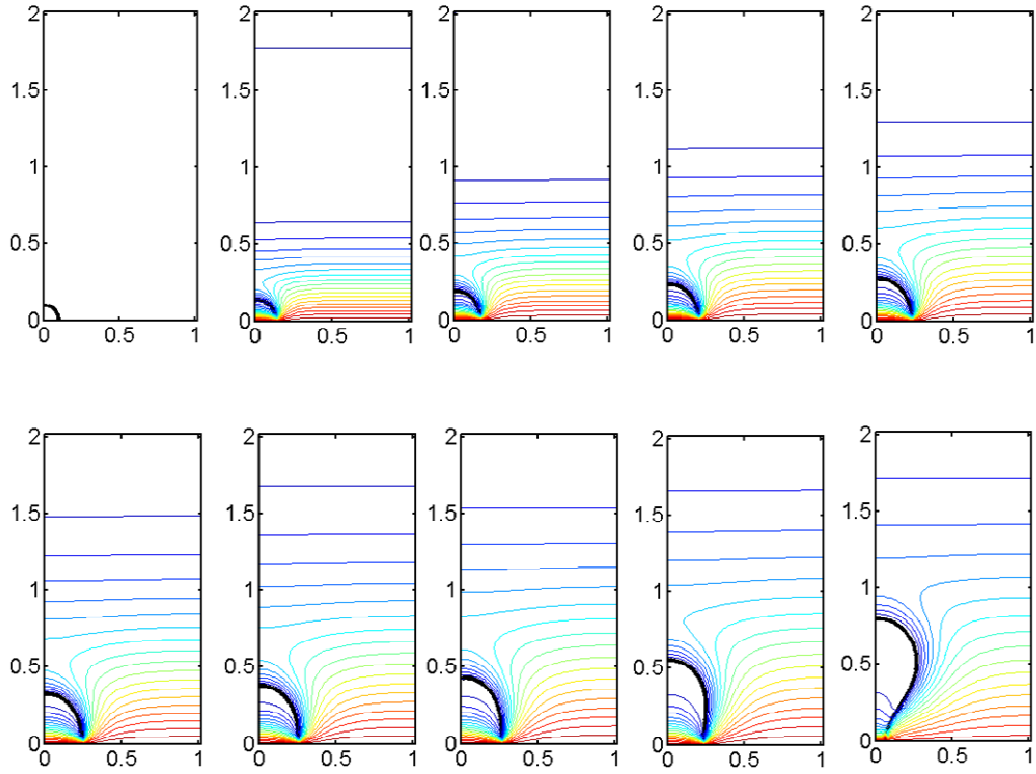


Figure 5.4: The growth of a vapor bubble in nucleate boiling. The time interval between two successive frames is 1 sec, starting at time, $t = 0$.

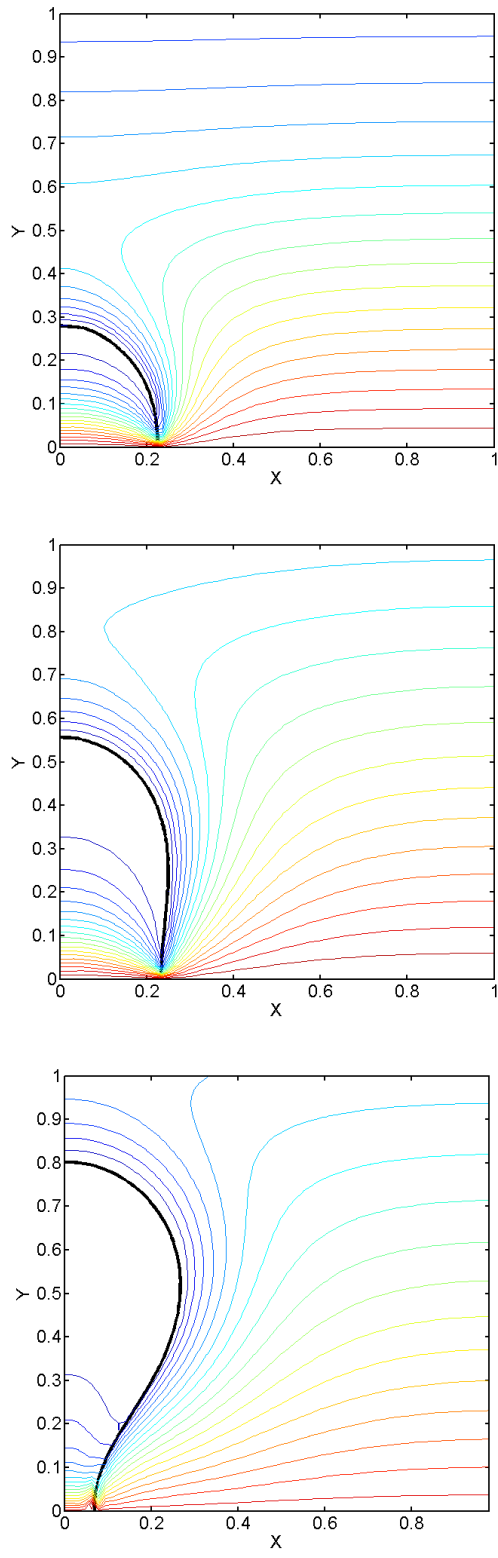


Figure 5.5: Close-up of the temperature contours around the vapor bubble at different times. (Top) Time, $t = 4$. (Middle) Time, $t = 8$. (Bottom) Time, $t = 9$.

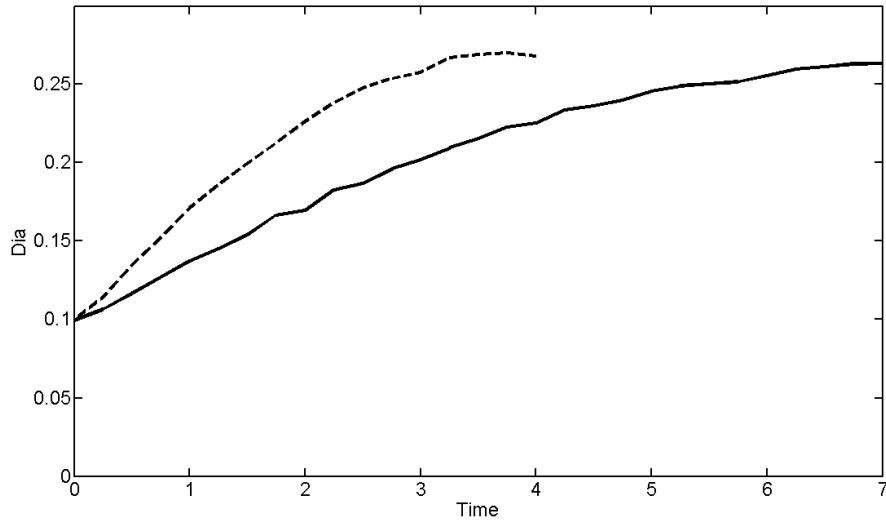


Figure 5.6: Bubble diameter till the departure occurs. The dashed line refers to a wall superheat of 2, while the solid line is for a wall superheat of 1. The end point of each line indicates the point of departure of the bubble.

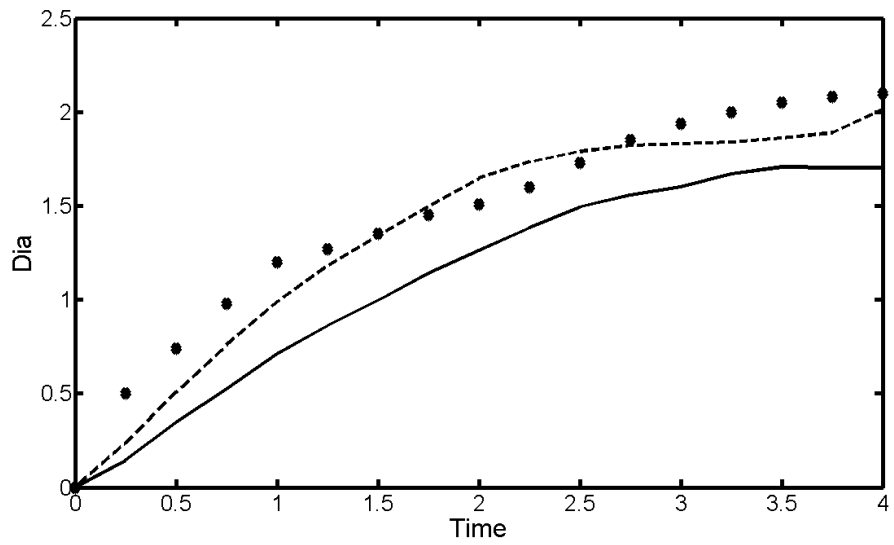


Figure 5.7: Bubble diameter over time. The solid line denotes bubble diameter for a wall superheat of 2, while dashed line is for a wall superheat of 3, and the circular dots represent the experimental results obtained by Seigel and Keshock (1964).

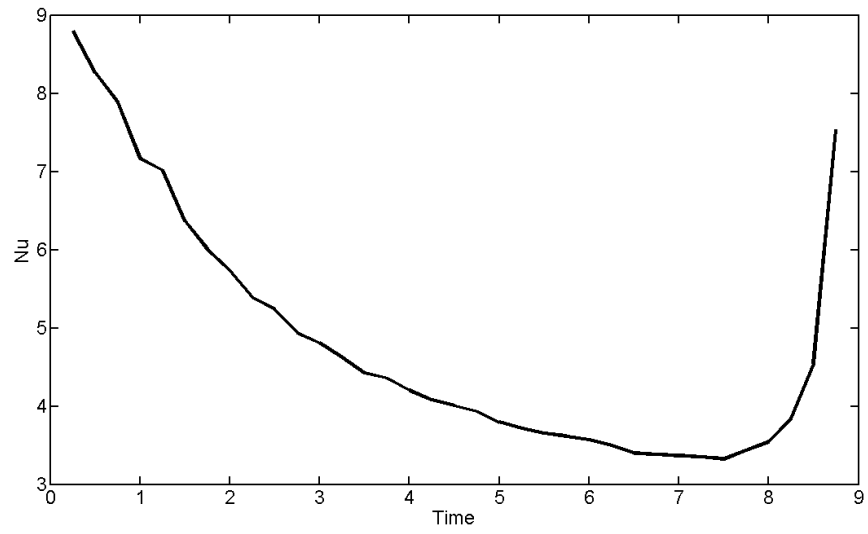


Figure 5.8: Variation of Nusselt Number over time during bubble growth for wall superheat of 1.

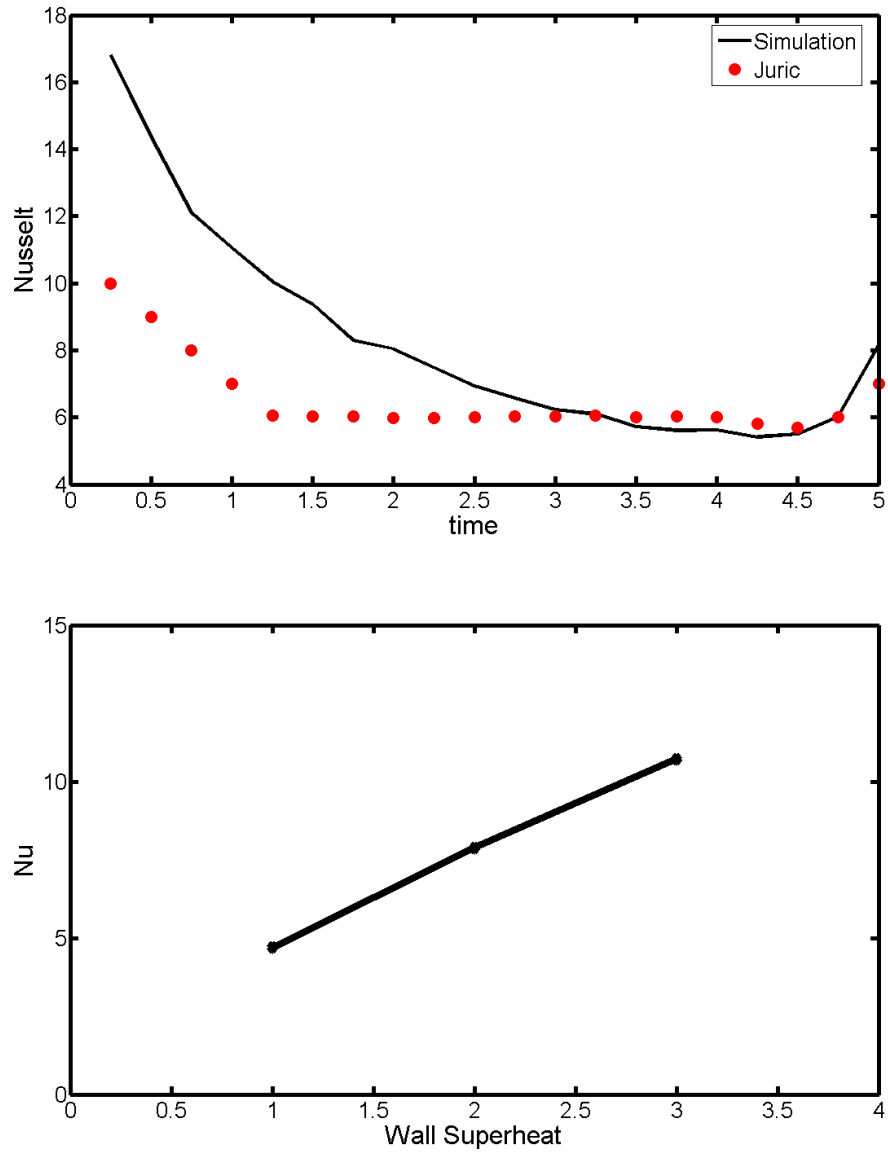


Figure 5.9: (Top) Comparison of Nusselt number with the results of Juric et al. (Bottom) Average Nusselt Number from inception to departure for different wall superheats.

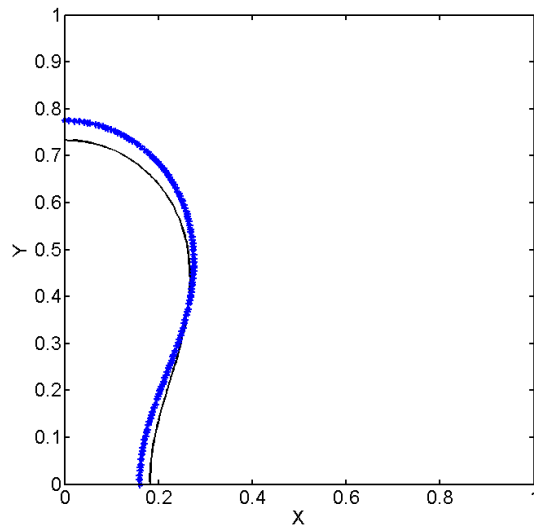
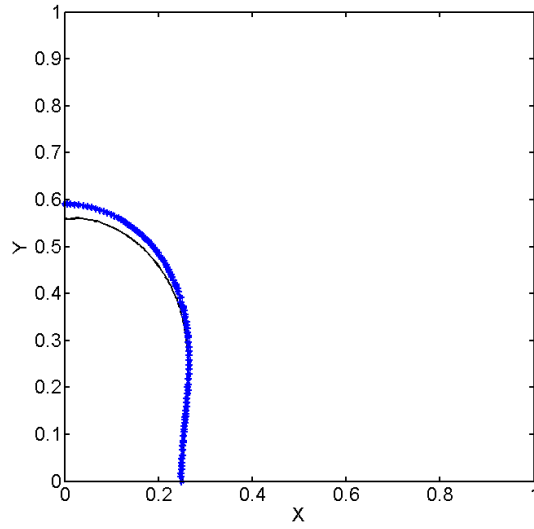


Figure 5.10: Comparison of the bubble shapes after the addition of the microlayer at a wall superheat of 2. The blue line shows the bubble shape with the microlayer, while the black line shows the bubble shape without the microlayer. (Top) Bubble shapes at time $t = 4.0$. (Bottom) Bubble shapes at time $t = 5.0$.

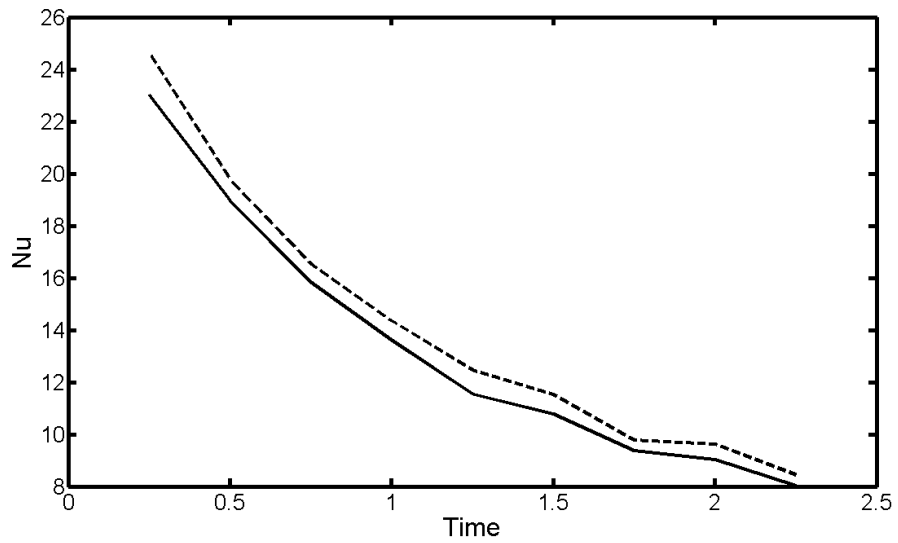
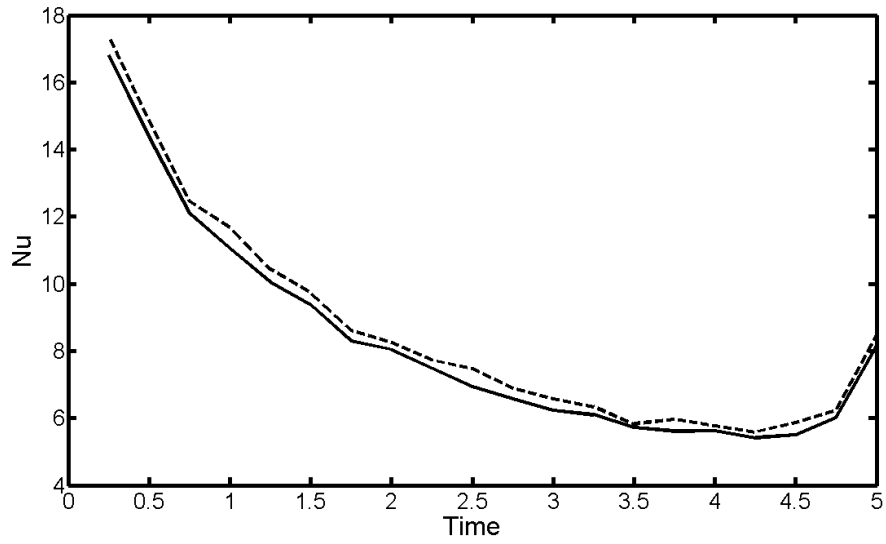


Figure 5.11: (Top). The Nusselt number variation over time at wall superheat of 2. The dashed lines are the simulations with the microlayer included. (Bottom). Nusselt number variation over time at wall superheat of 3.

CHAPTER 6

-

MASS TRANSFER

6.1 Introduction

Mass transfer between a dispersed drop and a continuous fluid/solid phase is of vital importance to a number of chemical processes like combustion, drying, polymerization etc. Besides industrial applications, mass transfer occurs naturally. Plants and animals have circulatory systems that exchange energy and nutrition, where mass transfer is decisive. Mass transfer can be defined as the process of transport of one or more components of a mixture, within a phase over a phase boundary. The driving forces behind the transfer of mass are the differences in concentration, pressure and/or temperature. The concentration gradient is the most commonly seen and studied. Equilibrium is reached when the gradient has disappeared.

Mass transfer by diffusion and convection are the two mechanisms of transporting different species. From a macroscopic standpoint, molecular diffusion is purely due to concentration difference. Mass transfer by convection takes place when there is a fluid flowing, instead of being still. Mass transfer by convection occurs at a faster rate than by diffusion, and hence is more widely applied.

Mass transfer from the surface of a solid to a flowing fluid, or mass transfer between two fluids that are barely miscible, depend on the properties of the materials involved and the type of the flow. When a fluid flows over a quiescent surface, with which a substance will be exchanged, a thin layer develops close to the surface. In this layer, the velocity is small and drops to zero at the surface. Therefore close to the surface the convective part of mass transfer is very low and the diffusive part of mass transfer dominates. The assumption is that the amount of material transferred from the substance is negligible when compared to the amount of fluid that flows over. The concentration of the substance beyond the interface separating it from the fluid remains constant, and the concentration of the substance in the passing fluid is taken to be negligible. Away from the interface separating the phases, the concentration levels are unchanged. The challenge is to capture the nature of the concentration gradient close to the interface..

Theoretical solutions for mass transfer exist in the literature; Baehr & Stephan (2006) calculated the mass transfer coefficients for cases like the steady state convective mass transfer and one-dimensional mass transfer in quiescent flow. Chen and Sun (1996) studied the effects of correlations of mass transfer coefficient with respect to the inlet Reynolds number and physical properties in a combined vertical film-type absorber-evaporator exchanger. Doan et al. (2001) measured the local and overall mass transfer coefficients to a sphere in a quiescent ferri-ferrocyanide solution. They found that the experimental Sherwood number for mass transfer to the whole sphere was 110 rather than 2 as for pure diffusion. The local mass transfer rate, in the absence of mass transfer to the rest of the sphere surface did not change

significantly with the angular position to the upward vertical as it does when mass transfer occurs over the whole sphere simultaneously.

Gumerov (1996) concluded that no semi-empirical model can accurately describe the mass flux from a rising vapor bubble and proscribed the need for mechanistic models or full-scale numerical simulations. Piarah et al. (2001) performed direct numerical simulations with commercial CFD software for the mass transfer between a single drop and ambient flow, where the setup is formulated as a “conjugate” problem where there is considerable resistance to the mass transfer in both the continuous and dispersed phases, and interfacial mass transfer occurs only for the solute. Favelukis and Mudunuri (2003) obtained a theoretical solution for the unsteady mass transfer around an axisymmetric drop in a continuous phase for creeping flow conditions by assuming that the resistance to the mass transfer lies only in the concentration boundary layer. Davidson and Rudman (2002) performed numerical simulations using the Volume-of-Fluid (VOF) method to calculate the simultaneous heat and mass transfer from deforming interfaces. For a rising bubble, the method matches very well to experimental results when the wake of the bubble is non-oscillating. Goldstein and Cho (1995) had previously used this heat-mass transfer analogy to measure the mass transfer coefficient during naphthalene sublimation to make universal predictions about mass transfer for a variety of complex flows and geometries, but with certain restrictions. For a further review of the empirical and mechanistic models of mass transfer for gas-fluidized beds, the paper by Yusuf et al. (2005) is a good source.

One of the applications prominently featured in recent times is the sequestration of carbon dioxide (CO₂). CO₂ extracted from factories, thermal power plants etc. are liquefied and injected in the depths of the ocean. This action instantly reduces the amount of CO₂ in the atmosphere from these sources. But the challenge is to allow for slow dissolution of the rising CO₂ bubbles into the ocean water in order to minimize its impact on biological life. It has been observed by Vasconcelos et al. (2002) that surface contaminants present on gas bubbles retard the surface mobility on an otherwise clean surface and thereby reduce the mass transfer across the interface. They also formulated the “surfactant-cap” model to illustrate this effect. Numerical studies by Jung and Sato (2001) using the marker density function captured the mass transfer across the interface of a rising bubble. They concluded that the dispersed phase dissolves completely into the continuous phase. The effect of surfactants on the dissolution rate of CO₂ bubbles was also studied by Ponoth et al. (2000) using the “surfactant-cap” model. The convective equation for the concentration field was solved by the Ryskin-Leal adaptive grid method and concentration boundary layer was resolved by means of molecule marker computations. Sharifullin and Luebbert (2000) experimentally observed the mass transfer from a single oxygen bubble in the presence of surfactants and found that surfactants decrease the rate of oxygen transfer by 10%. Alves et al. (2005) also used the spherical-cap hypothesis, which assumes a rigid cap which retards the rise and mass transfer to model mass transfer from low solubility gases, like air. Direct numerical simulations were performed by Sato et al. (2000) by solving the transport equation and thereby gaining an understanding of the unidirectional dispersal of CO₂ from the dispersed phase to the continuous phase.

Mass transfer from aerosols plays an important role in a large number of physical and chemical processes, fuel combustion and pulmonary drug delivery. Lim et al. (2008) used numerical simulations to capture the liquid evaporation of aerosols. The motions of the particles were tracked with the aid of Lagrangian schemes, while the Navier-Stokes equations were solved for the continuous phase. Two liquid evaporation models were incorporated for mass transfer and reasonable agreement was found between the computational and experimental results. The models showed a good match with experiments for less volatile liquids like water, but diverged with more volatile liquids like hexane, suggesting that the current liquid evaporation models are inadequate. Drying is an important industrial process and vital due to its energy intensive nature. Hussain and Dincer (2003) analyzed the moisture transfer of a cylindrical moist object subject to drying under diffusive conditions only. Kaya et al. (2006) put forward an expression for the mass transfer coefficient for drying moist objects under forced convection conditions by utilizing the relationship between the thermal and concentration boundary layers. Queiroz et al. (2001) studied the drying kinetics of bananas and provided a model to calculate the mass transfer coefficient to account for the shrinkage effect. With the help of experimental observations, Tiwari (1997) developed a semi-empirical model to evaluate the convective mass transfer in a solar distillation process. Mezhericher (2008) modeled the unsteady drying of a wet silica droplet in ambient air by assuming a quasi-steady state mass transfer and linear pressure profile within the capillary pores.

Other practical examples include: Li, Peng and Lee (2004) simulating mass transfer occurring during nucleate boiling by modeling the mass transfer across the vapor-liquid interface using a “thermo-capillary” flow model, Radl et al. (2007)

presenting an Upper-Convected Maxwell (UCM) model to describe the concentration fields of dissolved gas in visco-elastic fluids, wherein observing unexpected mixing characteristics, and Ma et al. (1997) quantitatively measuring the mass transfer of oxygen or atherogenic molecules at the carotid bifurcation, useful in the early detection of atherosclerosis by the observation that the convection of oxygen may be low in the regions where the thickening of the arteries has started.

As mentioned earlier, convective mass transfer across deformable fluid interfaces is of wide interest in a great number of industrial and scientific applications. In many cases however, the precise internal structure of the species concentration at the interface during mass transfer is of minor importance and attention can be focused on obtaining the global properties of the layer. Instead of refining the grid to be small enough to capture all the scales, which would run up the computational costs, the approach here is to determine the global property of principal interest, the species concentration through an accurate model.

To this achieve this end; we use the partial differential equations governing the unsteady evolution of the mass transfer profiles to derive an ordinary differential equation for the evolution of moments of these profiles. From these, it will be clear that the internal structure of the layer affects its evolution only through integrals. We model the internal structure by assuming the profiles to be self-similar and represented by a family of curves parameterized by four degrees of freedom. The moment equations then determine the time evolution of these degrees of freedom, which in turn obtains the concentration profile.

The central idea behind this way of thinking is quite similar in spirit to the integral methods used to compute the development of boundary layers in analytical fluid mechanics and wall-functions in turbulence modeling. In that case, the von Kármán momentum integral equation can be termed as the zeroth moment of the velocity profile. The von Kármán momentum equation calculates the downstream evolution of the boundary layer properties such as the wall shear stress, the boundary layer thickness etc. In the same way, the profile of the concentration layer is evaluated.

The species concentration is governed by a linear advection-diffusion equation and the reaction constitutes a (nonlinear) source term. In practice, however, the slow diffusion of mass compared to the evolution of the flow scales (and sometimes temperature) pose formidable stiffness and resolution requirements. Koynov, Khinast and Tryggvason (2005) found that mass transfer and chemical reactions is extremely sensitive to system hydrodynamics. For a single bubble, the mass transfer rate rises with increasing Reynolds number until the vortex-shedding regime is attained. The mass transfer in a swarm of bubbles is vastly different from that of a single bubble, owing to the motion of the swarm as a whole and the interactions between individual bubbles. Koynov, Khinast and Tryggvason (2006) also observed that in deformable bubble swarms, if the bubbles are close to each other, the dissolved gas and product formation is in their combined wake and not in the individual ones. The key observation is that in spite of the numerical difficulties, the solution is—in most cases—relatively simple. Since mass diffusion is slow, the competition with advection usually results in thin boundary layers (that require fine grid if we resolve them fully). Thus, the concentration of a gas dissolving from a rising bubble will change rapidly next to the bubble, but since it is the gradient at the bubble surface that determines the

rate at which the gas leaves the bubble it must be determined accurately. The thickness of the mass-boundary layer is usually much thinner than the fluid boundary layer and the fluid motion “seen” by the mass-boundary layer changes slowly on scales comparable to its thickness. The obvious way to accommodate the mass diffusion next to the bubble, without fully resolving the layer by refining the grid, is therefore to use a boundary layer approximation to capture it. It has been done earlier, in the context of numerical modeling of strained diffusion-reaction layers. Tryggvason and Dahm (1991) introduced a method for one-dimensional flames using a simple one step reaction model. The approach is based on assuming that the dynamics is governed by a one-dimensional equation across the layer, but including strain along the layer. ODEs for the various moments of the concentration profiles (or their gradients in some cases) were derived. The moments can be related directly to the total jump in concentration or the total amount of mass (zeroth moment of the profile or its gradient, respectively) and higher order moments give other properties. The source terms can only be computed by assuming specific shapes of the profiles but as shown in Chang, Dahm and Tryggvason (1992) even relatively crude approximations give good results.

In Chang et al. (1992) a similar approach was also used to model the vortex dynamics of the shear layer and although this is more challenging, the results nevertheless showed reasonably good agreement, including burnout in the core and flameout in the braids, depending on the governing parameters. Building on their earlier works, Dahm, Tryggvason et al. (1996) advanced the model to predict the dynamics of a flame in multi-step finite chemical reactions, for which the kinetics of

each reaction has to be taken into account, to reasonable accuracy, by still selecting reasonably simple profiles.

The rest of this chapter is organized as follows. First, the governing equations for the specie transport are formulated, and then the evolution of the moment equations is derived. In the next section, the equations are “closed” by imposing simple profile shapes. The profiles studied are linear, quadratic, exponential and bi-linear. Results from each profile shape are compared to the full simulation solutions and conclusions are presented.

6.2 Governing Equations

The unsteady, one-dimensional equation for specie transport across an interface is,

$$\frac{\partial C}{\partial t} + U \frac{\partial C}{\partial x} = D \frac{\partial^2 C}{\partial x^2} \quad (6.1)$$

where U is the local velocity and D is the coefficient of mass diffusion. The specie concentration is determined by a competition between advection and diffusion. The solution exhibits a concentration boundary layer behavior near the interface and the thickness of the boundary layer is proportional to D/U . For low D/U , a simple forward in time and centered in space code requires a large number of uniformly spaced grid points to adequately capture the solution. The nature of the variation of the concentration in this region is captured by a profile. Any concentration profile in the boundary layer is assumed to depend on four parameters,

$$C = C(C_w, C'_w, C_\delta, C'_\delta) \quad (6.2)$$

where δ is the thickness of the layer that we model (the first grid interval), the prime denotes a spatial derivative, C_w is the value of specie concentration at the wall (or interface), C'_w is the gradient at the wall, C_δ is the specie concentration at the first grid interval and C'_δ is the gradient at the first grid interval.

Of these, C_w is always constant and known, and C'_δ can be found from the finite difference solution for the rest of the domain. To solve for the two unknowns, we require two equations. The two equations are obtained by taking the moments of the concentration profile and solving for their time evolution. The moments allow us to compute quantities such as the value of the solution at the edge of the modeled interval and the gradient near the wall.

$$M_0 = \int_0^\delta C dx \quad (6.3)$$

$$M_1 = \int_0^\delta x C dx \quad (6.4)$$

To write the equation for the evolution of the zeroth moment of the concentration equation, we re-formulate the three terms in (5.1).

$$\frac{\partial M_0}{\partial t} = \frac{\partial}{\partial t} \int_0^\delta C dx \quad (6.5)$$

$$U \frac{\partial}{\partial x} \left(\int_0^\delta C dx \right) = U \int_0^\delta \frac{\partial C}{\partial x} dx = U(C_\delta - C_w) \quad (6.6)$$

$$D \frac{\partial}{\partial x} \left(\frac{\partial}{\partial x} \left(\int_0^\delta C dx \right) \right) = D \int_0^\delta d \left(\frac{\partial C}{\partial x} \right) = D(C'_\delta - C'_w) \quad (6.7)$$

Combining (5.5), (5.6) and (5.7), the evolution of the zeroth moment of concentration is written as,

$$\frac{\partial M_0}{\partial t} = -U(C_\delta - C_w) + D(C'_\delta - C'_w) \quad (6.8)$$

Using the same procedure to derive the equation for the first moment, the individual terms are,

$$\frac{\partial M_1}{\partial t} = \frac{\partial}{\partial t} \left(\int_0^\delta x C dx \right) \quad (6.9)$$

$$U \frac{\partial}{\partial x} \left(\int_0^\delta x C dx \right) = U \int_0^\delta x \frac{\partial C}{\partial x} dx = U \int_0^\delta \left(\frac{\partial x C}{\partial x} - C \right) dx = U(\delta C_\delta - M_0) \quad (6.10)$$

$$D \left(\int_0^\delta x \frac{\partial^2 C}{\partial x^2} dx \right) = D \int_0^\delta \left(\frac{\partial}{\partial x} \left(x \frac{\partial C}{\partial x} \right) - \frac{\partial C}{\partial x} \right) dx = D(\delta C'_\delta - C_\delta + C_w) \quad (6.11)$$

The equation for the first moment will be,

$$\frac{\partial M_1}{\partial t} = -U(\delta C_\delta - M_0) + D(\delta C'_\delta - C_\delta + C_w) \quad (6.12)$$

At every time step, the new values of M_0 and M_1 will be updated and then used to solve the equations for C_δ and C'_w simultaneously.

6.3 Time evolution of the profiles

6.3.1 Evolution of the linear profile

Figure 5.1 shows the schematic of the linear profile. The concentration profile in the linear is of the form,

$$C(x) = ax + b$$

where a and b are to be determined. To solve for the unknowns, the following boundary conditions are utilized,

$$\begin{aligned}
\text{at } x = 0; \quad C(0) &= C_w \\
\therefore b &= C_w \\
\text{at } x = \delta; \quad C'(\delta) &= C'_w \\
\therefore a &= C'_w = \frac{C_\delta - C_w}{\delta}
\end{aligned}$$

The linear equation in its final form is,

$$C(x) = \frac{C_\delta - C_w}{\delta} x + C_w \quad (6.13)$$

In the linear case, there is only one unknown, C_δ and therefore just the zeroth moment equation is required.

$$M_0 = \int_0^\delta C(x) dx = \int_0^\delta \left(\frac{C_\delta - C_w}{\delta} x + C_w \right) dx$$

On solving,

$$M_0 = \frac{\delta}{2} (C_\delta + C_w)$$

Re-writing the above expression for C_δ

$$C_\delta = \frac{2M_0}{\delta} - C_w \quad (6.14)$$

Now, the value of C_δ obtained from (5.14) is substituted in the time evolution equation for the zeroth moment (6.8) to evaluate the value of M_0 at the next time step.

6.3.2 Evolution of the quadratic profile

Figure 5.2 represents the quadratic concentration profile. In general it is written as,

$$C(x) = ax^2 + bx + c$$

where a , b and c are the unknowns. The appropriate boundary conditions are

$$\text{at } x = 0; \quad C(0) = C_w$$

$$\therefore c = C_w$$

$$\text{at } x = 0; \quad C'(0) = C'_w$$

$$\therefore b = C'_w$$

$$\text{at } x = \delta; \quad C(\delta) = C_\delta$$

$$\therefore a = \frac{C_\delta - C_w - \delta C'_w}{\delta^2}$$

The quadratic equation in its final form is,

$$C(x) = \frac{C_\delta - C_w - \delta C'_w}{\delta^2} x^2 + C'_w x + C_w \quad (6.15)$$

In the quadratic case, however, C_δ and C'_w are both unknowns and thus two moment equations are used.

$$M_0 = \int_0^\delta \left(\frac{C_\delta - C_w - \delta C'_w}{\delta^2} x^2 + C'_w x + C_w \right) dx$$

$$M_1 = \int_0^\delta x \left(\frac{C_\delta - C_w - \delta C'_w}{\delta^2} x^2 + C'_w x + C_w \right) dx$$

On solving the integrals,

$$M_0 = \frac{1}{3} (C_\delta - C_w - \delta C'_w) \delta + \frac{1}{2} C'_w \delta^2 + C_w \delta$$

$$M_1 = \frac{1}{4} (C_\delta - C_w - \delta C'_w) \delta^2 + \frac{1}{3} C'_w \delta^3 + \frac{1}{2} C_w \delta^2$$

The unknowns C_δ and C'_w can be calculated by solving the equations for M_0 and M_1 simultaneously.

$$C_\delta = - \frac{6\delta M_0 - C_w \delta^2 - 12 M_1}{\delta^2} \quad (6.16)$$

$$C'_w = \frac{6(3\delta M_0 - C_w \delta^2 - 4 M_1)}{\delta^3} \quad (6.17)$$

The values from (6.16) and (6.17) are used in (6.8) and (6.9) to update M_0 and M_1 at each time step.

6.3.3 Evolution of the bi-linear profile

The concentration profile in the bi-linear formulation is,

$$\begin{aligned} C(x) &= ax + b && \text{if } 0 \leq x \leq \Delta \\ &= c_1(x - \delta) + d && \text{if } \Delta \leq x \leq \delta \end{aligned}$$

where a , b , c_1 and d are the unknowns. The schematic representation of the profile is shown in Figure 6.3. The unknowns are evaluated from the boundary conditions,

$$\begin{aligned} \text{at } x = 0; C(0) &= C_w \\ \therefore b &= C_w \\ \text{at } x = 0; C'(0) &= C'_w \\ \therefore a &= C'_w \\ \text{at } x = \delta; C(\delta) &= C_\delta \\ \therefore d &= C_\delta \\ \text{at } x = \delta; C'(\delta) &= C'_\delta \\ \therefore c_1 &= C'_\delta \end{aligned}$$

The bi-linear equation in its final form is,

$$\begin{aligned} C(x) &= C'_w x + C_w && \text{if } 0 \leq x \leq \Delta \\ &= C'_\delta(x - \delta) + C_\delta && \text{if } \Delta \leq x \leq \delta \end{aligned} \quad (6.18)$$

where

$$\Delta = \frac{C_\delta - C_w + C'_\delta \delta}{(C'_w - C'_\delta)} \quad (6.19)$$

In the quadratic case, C_δ and C'_w are both unknowns and thus, two moment equations will be used.

$$M_0 = \int_0^\Delta (C'_w x + C_w) dx + \int_\Delta^\delta (C'_\delta(x - \delta) + C_\delta) dx$$

On solving the zeroth moment equation,

$$M_0 = C_w \Delta + \frac{1}{2} C'_w \Delta^2 + \frac{1}{2} C'_\delta (\delta^2 - \Delta^2) + C_\delta (\delta - \Delta) - C'_\delta \delta (\delta - \Delta)$$

The first moment can be similarly solved as,

$$M_1 = \int_0^{\Delta} x (C'_w x + C_w) dx + \int_{\Delta}^{\delta} x (C'_\delta (x - \delta) + C_\delta) dx$$

On solving the integrals,

$$M_1 = -\frac{1}{3} \frac{C'_w (C_w - C_\delta + C'_\delta \delta)^3}{(C'_w - C'_\delta)^3} + \frac{1}{3} \frac{C_w (C_w - C_\delta + C'_\delta \delta)^2}{(C'_w - C'_\delta)^2} +$$

$$\frac{1}{3} C'_\delta \left(\delta^3 + \frac{(C_w - C_\delta + C'_\delta \delta)^3}{(C'_w - C'_\delta)^3} \right) + \frac{1}{2} (C_\delta - C'_\delta \delta) \left(\delta^2 - \frac{(C_w - C_\delta + C'_\delta \delta)^2}{(C'_w - C'_\delta)^2} \right)$$

On solving the equations for M_0 and M_1 simultaneously, the unknowns C_δ and C'_w can be calculated.

$$C_\delta = A$$

$$C'_w = -\frac{1}{\delta^2 (-2M_0 + C'_\delta \delta^2 - 2\delta A)} \left(-5A\delta^2 C_w + 3C'_\delta \delta^3 C_w - 6\delta^2 M_0 C'_\delta \right.$$

$$\left. + 2\delta^2 C_w^2 - 6AM_1 + 8AM_0 \delta + 6M_1 C_w \right.$$

$$\left. + 6M_1 C'_\delta \delta - 4M_0^2 \right)$$

(6.20)

where

$$A = -\frac{1}{2\delta^2} \left\{ 3C_w \delta^2 + 6M_1 + 8\delta M_0 + \right.$$

$$\left(36M_1^2 - 60C_w \delta^2 M_1 - 96M_1 \delta M_0 + 9C_w^2 \delta^4 - 48C_w \delta^3 M_0 \right.$$

$$\left. + 48\delta^2 M_0^2 + 4\delta^5 C'_\delta C_w - 16\delta^4 M_0 C'_\delta + 24\delta^3 M_1 C'_\delta \right)^{\frac{1}{2}} \left. \right\}$$

(6.21)

6.3.4 Evolution of the exponential profile

The exponential profile is sketched in Figure 5.4, and is represented as

$$C(x) = (C_w - a)e^{-bx} + a$$

where a and b are the unknowns. The boundary conditions are

at $x = \delta$; $C(\delta) = C_\delta$

$$C_\delta = (C_w - a)e^{-b\delta} + a \quad (6.22)$$

at $x = 0$; $C'(0) = C'_w$

$$C'_w = -(C_w - a)b \quad (6.23)$$

Trying to solve for a and b , the following nonlinear expression is obtained,

$$\frac{1}{b}(1 - e^{-b\delta}) = \frac{C_\delta - C_w}{C'_w} \quad (6.24)$$

To resolve this difficulty, an approach similar to the one employed by Smith et al. (2007) is utilized. In their formulation, they used an exponential profile to study boundary layer behavior in biofilm growth under steady state conditions. They adjusted the coefficient in the exponential term such that its value at the edge of the modeled interval is almost zero, i.e.

$$\text{at } x = \delta, \quad e^{-b\delta} \rightarrow 0$$

Now,

$$a = C_\delta$$

$$b = -\frac{C'_w}{C_w - C_\delta}$$

The exponential equation in its final form is,

$$C(x) = (C_w - C_\delta)e^{-\left(-\frac{C'_w}{C_w - C_\delta}\right)x} + C_\delta \quad (6.25)$$

The moment equations are,

$$M_0 = \int_0^\delta \left((C_w - C_\delta)e^{-\left(-\frac{C'_w}{C_w - C_\delta}\right)x} + C_\delta \right) dx$$

$$M_1 = \int_0^\delta x \left((C_w - C_\delta)e^{-\left(-\frac{C'_w}{C_w - C_\delta}\right)x} + C_\delta \right) dx$$

On solving the integrals,

$$M_0 = \frac{1}{C'_w} \left(-C_w^2 + 2C_w C_\delta - C_\delta^2 + e^{-b\delta} C_w^2 - 2e^{-b\delta} C_w C_\delta + e^{-b\delta} C_\delta^2 + \delta C_\delta C'_w \right)$$

$$M_1 = \frac{1}{2C_w'^2} \left(-6C_w^2 C_\delta - 2C_\delta^3 + 2C_w^3 + 6C_w C_\delta^2 + 2e^{-b\delta} C_w^2 \delta C'_w \right. \\ \left. - 4e^{-b\delta} C_\delta C_w \delta C'_w - 2e^{-b\delta} C_w^3 + 6e^{-b\delta} C_w^2 C_\delta \right. \\ \left. - 6C_w e^{-b\delta} C_\delta^2 + 2C_\delta^2 e^{-b\delta} \delta C'_w + 2C_\delta^3 e^{-b\delta} + \delta^2 C_\delta C_w'^2 \right)$$

As $e^{-b\delta} \rightarrow 0$

The equations for M_0 and M_1 reduces to,

$$M_0 = C_\delta \delta - \frac{(C_w - C_\delta)^2}{C'_w}$$

$$M_1 = \frac{1}{2} C_\delta \delta^2 - \frac{(C_w - C_\delta)^3}{C_w'^2}$$

The unknowns C_δ and C'_w can be calculated,

$$C_\delta = A$$

$$C'_w = \frac{1}{3} \frac{(3\delta C_w^2 - 5A + 2AM_1 + 4A\delta M_0 - 2C_w M_1 - 2M_0^2)}{\delta^2 (-M_0 + A\delta)}$$

where

$$A = \frac{1}{6\delta^2} \left(C_w \delta^2 + 2M_1 + 4\delta M_0 + \left(C_w^2 \delta^4 - 20C_w \delta^2 M_1 + 8C_w \delta^3 M_0 + 4M_1 + 16M_1 \delta M_0 - 8\delta^2 M_0^2 \right)^{\frac{1}{2}} \right)$$

6.4 Results and Discussion

The validity of the integrals solved above has been tested with the full finite difference simulations. The full finite difference solution for the 1-D unsteady concentration equation is presented and its evolution can be seen in Figure 6.5. The intention is to provide for a stable, robust and accurate model that works with relatively simple equations and which then can be ported to more complex setups, like 3-D mass transfer, or multi-step chemical reactions etc. The present set of equations is useful in calculating mass transfer from a rising gas bubble in ambient liquid.

The problem at hand has been calculated at an initial velocity, $U = 1$ and diffusion coefficient, $D = 0.05$ and length scale, $L = 1$, for both the full simulations and the models for the sake of simplicity. The product of the Reynolds number and Schmidt (Sc , $Sc = \frac{U}{D}$) number gives a rough estimate of the size of the concentration boundary layer. Generally as the nondimensional product $Re \cdot Sc$ increases, the concentration boundary layer becomes thinner.

All the full simulation runs used in comparison with the models are at maximum resolution of $n = 1000$. The assumption is that the mass transfer occurs from the dispersed phase to the ambient phase only. The evolution of the concentration profile over time (Figure 6.5) shows that there is a finite amount of time taken for the profile to reach the steady state. The value of $Re \cdot Sc$ is 20. In Figure 6.5, the concentration value far away from the interface ($x = 0$) remains close to zero, and the profile changes dramatically in the concentration boundary layer. The code developed for the full simulations converges to a single steady state curve for a range of grid

resolutions, ranging from 100 to 1000 grid points (Figure 6.6). For a given set of initial conditions, the time required for the evolution to attain steady state is the same irrespective of the grid resolution.

6.4.1 Linear Model

Figure 6.7 shows the comparison of the concentration profile between the linear model at a grid resolution, $n = 31$ and the full simulation results at $n = 1001$. The linear profile is easier to program than the other profile as there is only a single degree of freedom. The profile is steeper than the actual profile close to the interface, but converges to the actual values with increasing resolution. From Table 5.1, it is clear that the linear model fails at the very coarse grid resolutions and matches well with the full simulations for all the higher grid resolutions. The linear model is stable for a range of resolutions.

6.4.2 Quadratic Model

Figure 6.8 shows the quadratic model and the full simulation results. The quadratic model profile ($n = 31$) fits almost exactly with the full simulation results. The quadratic model, like the linear model is unable to provide a solution at the lower resolutions ($n = 11$ & $n = 21$). From grid resolutions of $n = 31$ to $n = 1001$, the model is stable and accurate (Table 5.2).

6.4.3 Bi-linear model

Figure 6.9 displays the steady state profile incorporating the bi-linear model ($n = 21$). The results with the bilinear model are unlike those of the other profiles. The model shows good agreement with the full simulation results at the lower grid

resolutions ($n = 11 - 26$), but is unstable at the higher grid resolutions. The bilinear model, though useful for a coarse grid setup is ultimately not very robust.

6.4.4 Exponential model

Figure 6.10 shows the closeness of the exponential model and the full simulation results. There is a slightly more observable deviation from the actual profile at the plotted resolution, $n = 31$. But it matches the exact value with increasing resolution. Like both the linear and quadratic profiles, the exponential model is not successful in predicting the profile shape at the lowest resolutions (Table 5.4) and is robust for a range of resolutions beyond that.

6.4.5 Reducing the Diffusion Coefficient

The diffusion coefficient, D is decreased from 0.05 to 0.01. The change in the diffusion coefficient changes the nature of the steady state concentration profile. The concentration boundary layer becomes thinner due to the lower diffusion coefficient (Figure 6.11). The nondimensional product $Re \cdot Sc$ is 100. Figure 6.11 shows the comparison of the linear, quadratic and exponential models with the full simulations. Here, the bilinear model is not successful in simulating the smaller diffusion layer. The minimum grid resolution required for the full simulations is 300 grid points. As can be seen, the other three models provide an accurate description of the evolution of the concentration profile.

The plots shown are for the lowest resolution (or largest mesh size) for which the model works accurately. For a grid resolution greater (or lower mesh size) than that value, the model fits the full simulations accurately, and hence not displayed.

The diffusion coefficient is reduced further to $D = 0.005$ ($Re \cdot Sc = 200$), which is a tenth of the original value, and the resulting profiles are plotted in Figure 6.12. As in the case with $D = 0.01$, the bilinear model fails, but the linear, quadratic and exponential models are successful. The minimum grid resolution required for the full simulations is 500 grid points.

6.4.6 Raising the Velocity

The method is put through another test by increasing the velocity. Increasing the velocity means that the diffusion layer will become thinner. Capturing the thinner diffusion layer is another testament to the veracity of our models.

Figure 6.13 shows the profiles when the velocity is $U = 2$ ($Re \cdot Sc = 40$). All the four models work well. As the velocity is increased to $U = 3$ ($Re \cdot Sc = 60$), the bilinear model does not work, while the other three capture the evolution nicely. When the velocity is quadrupled ($Re \cdot Sc = 80$), the concentration boundary layer becomes even thinner, and only the quadratic profile is able to capture that.

6.5 Conclusions

One-dimensional mass transport equation is solved and model profiles are employed to accurately predict the concentration of a substance in the concentration boundary layer. Four models profiles, viz. linear, bilinear, quadratic and exponential were tested for a variety of conditions and results were obtained.

The linear model is computationally less intensive, and provides stable and accurate results, for a large range of operating parameters ($Re \cdot Sc = 20 - 200$). However, for large values of velocity ($U = 4$), and very low grid resolution ($n = 10$), the linear profile fails. The bilinear model is valid when running extremely coarse grids. It does not work well when the grid size is very high, or the diffusion coefficient is reduced or the velocity is increased. The quadratic model is the most stable, working accurately for all the cases that were tested, except at coarse resolution. It is a robust profile, though it usually runs a little longer than the linear profile. The exponential model is more accurate than the linear profile for all the cases tested. Like the linear profile, it does not work for the highest velocity ($U = 4$). The accuracy of the quadratic and exponential models is always slightly better than the other profiles for our range of tests.

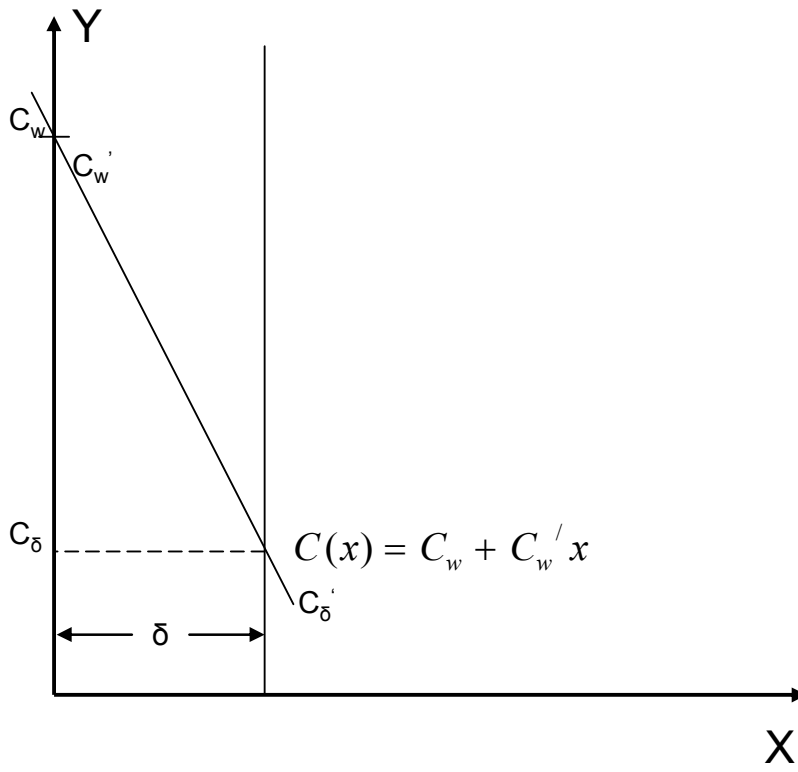


Figure 6.1: Schematic of the linear concentration profile

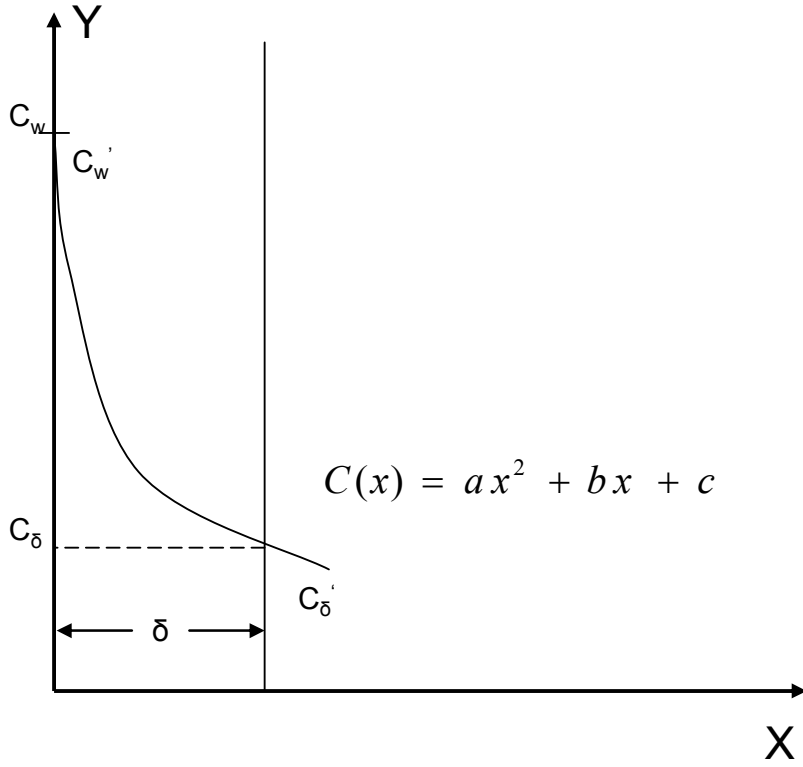


Figure 6.2: Schematic of the quadratic profile

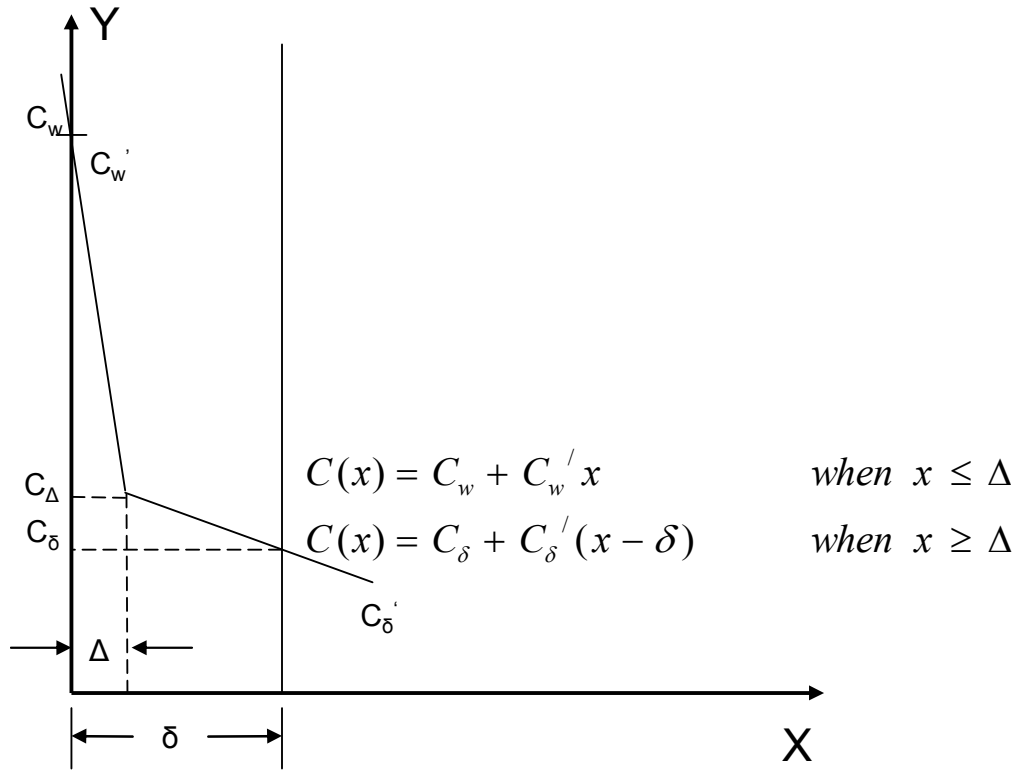


Figure 6.3: Schematic of the bi-linear concentration profile

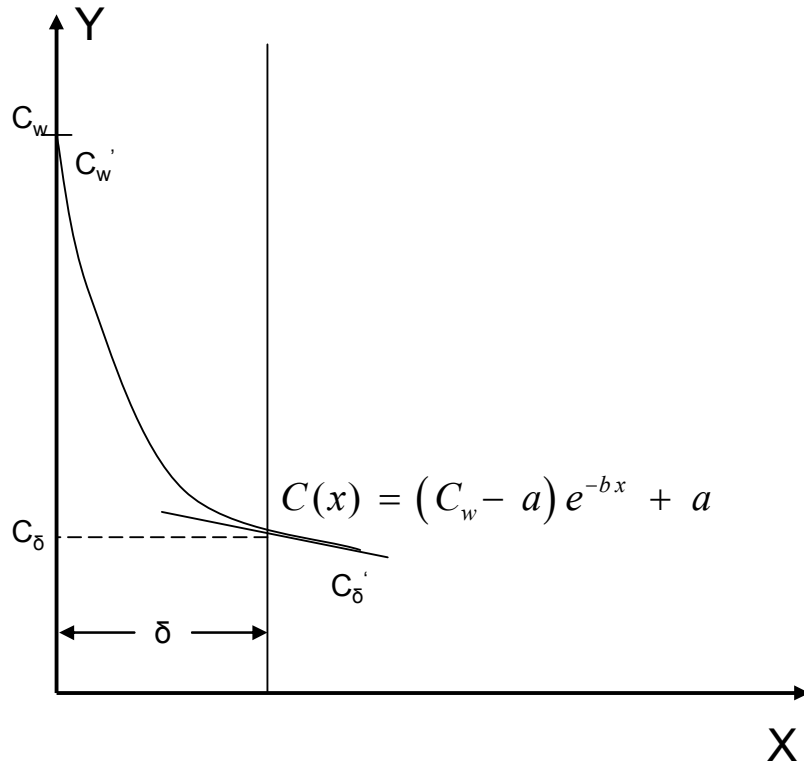


Figure 6.4: Schematic of the exponential profile

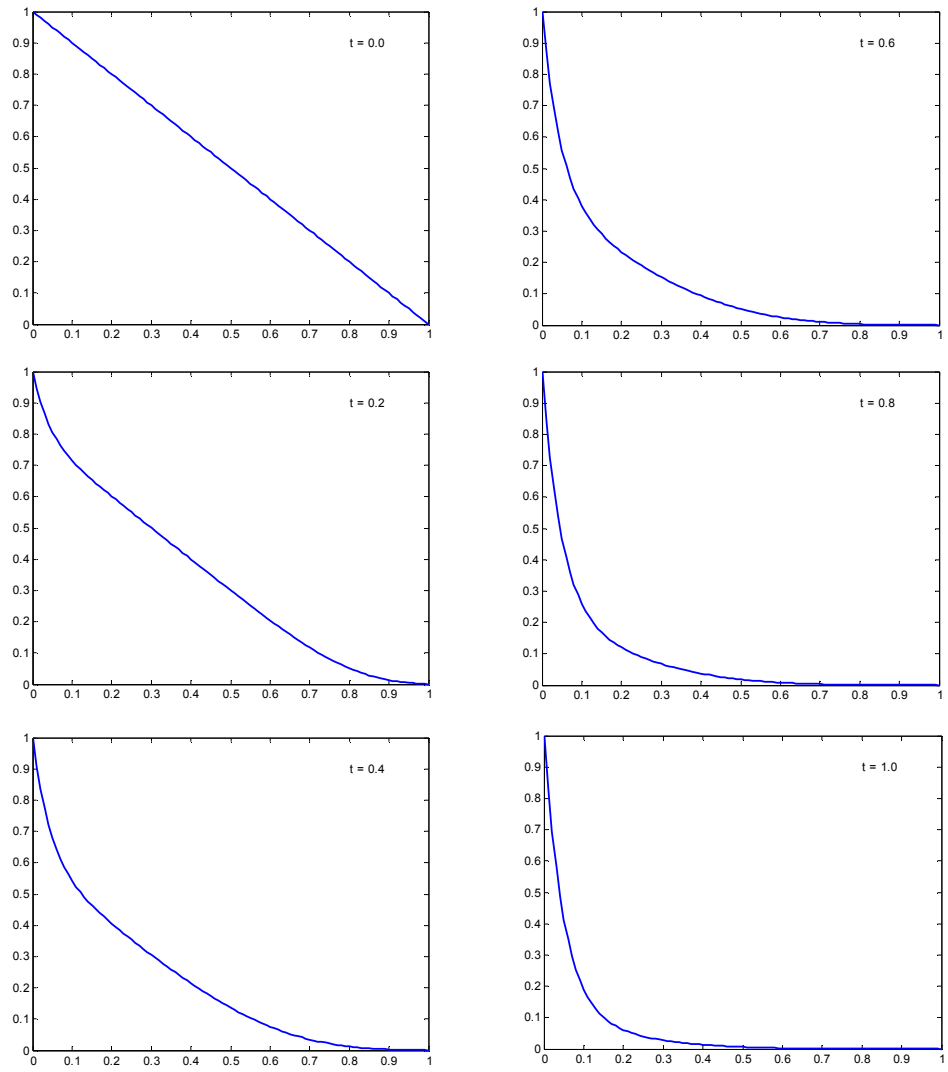


Figure 6.5 Time evolution of the concentration profile using finite difference methods, grid resolution = 1000 pts

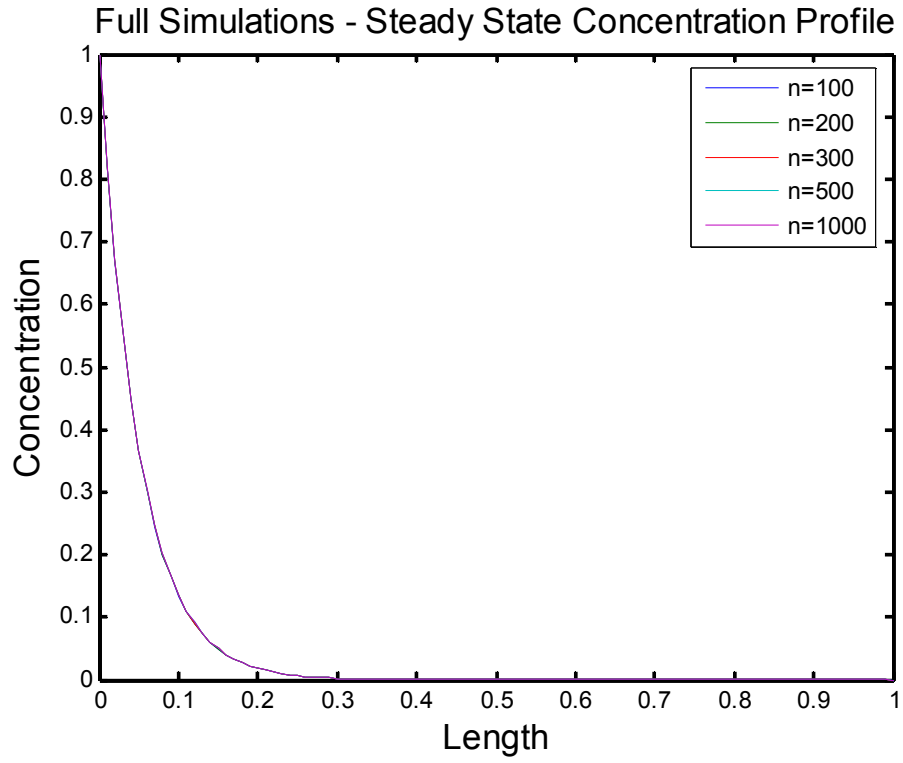


Figure 6.6: Steady state convergence of the finite difference method in solving the species transport equation

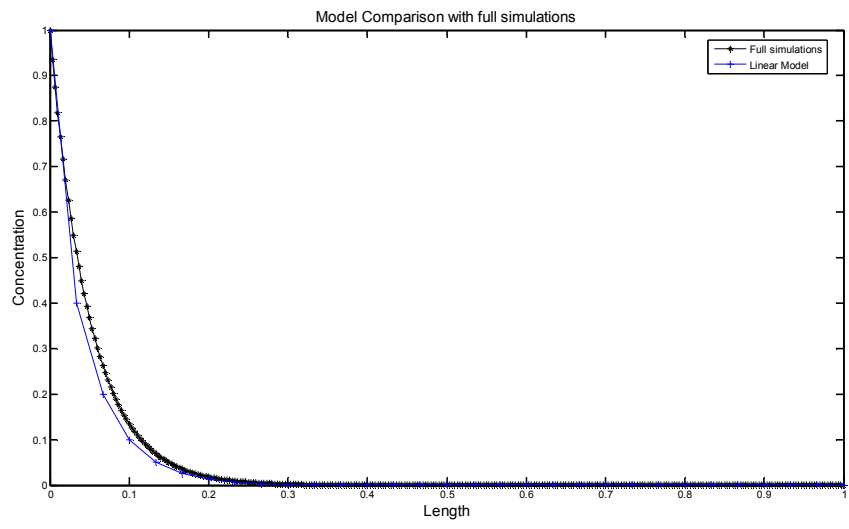


Figure 6.7: Steady state comparison of the linear model and the finite difference method

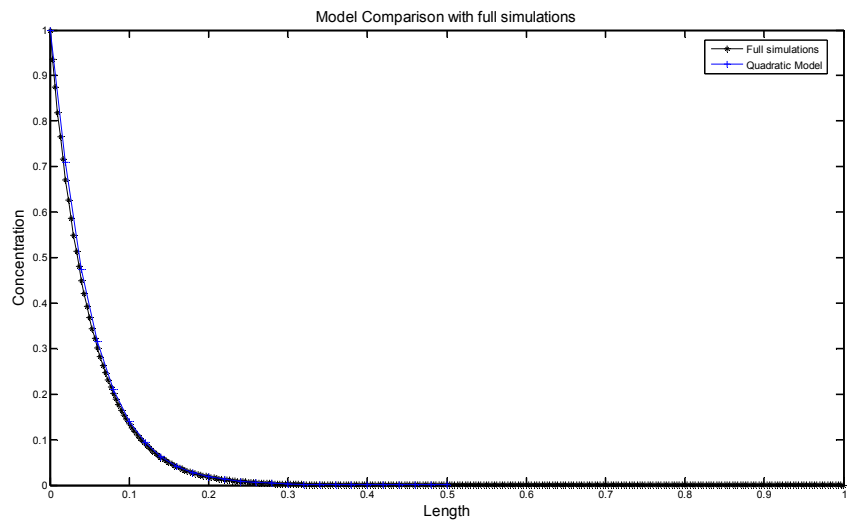


Figure 6.8: Steady state comparison of the quadratic model and the finite difference method

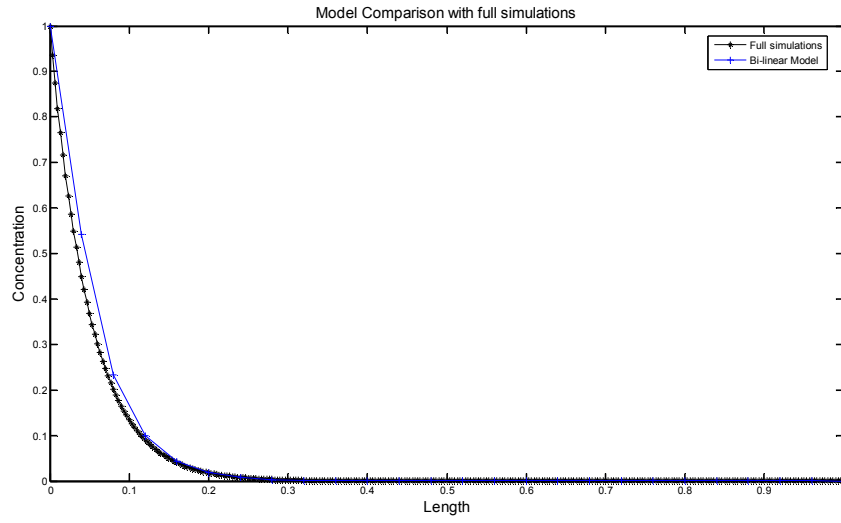


Figure 6.9: Steady state comparison of the bi-linear model and the finite difference method

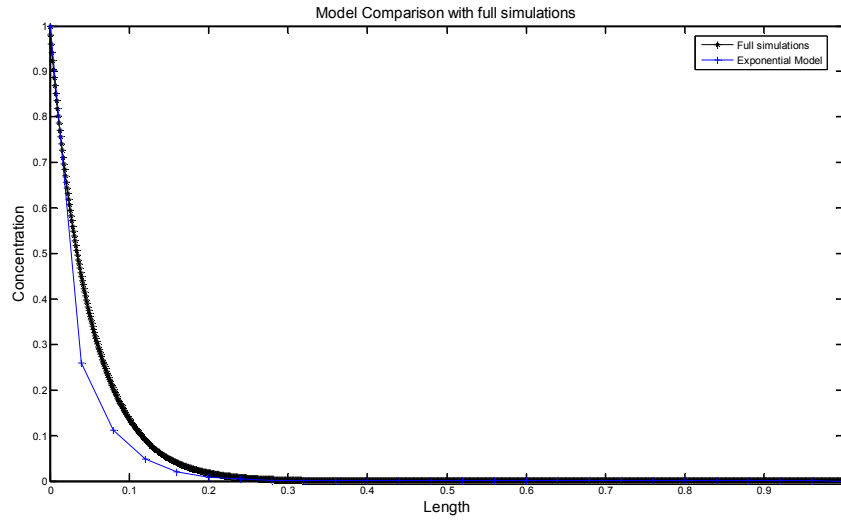


Figure 6.10: Steady state comparison of the exponential model and the finite difference method

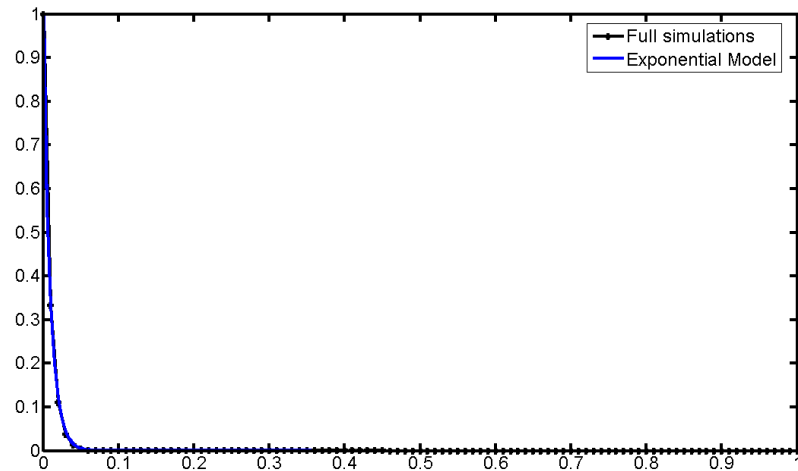
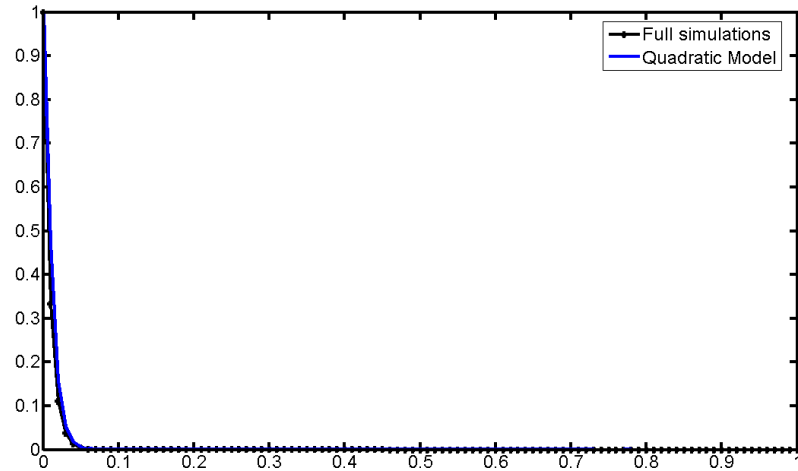
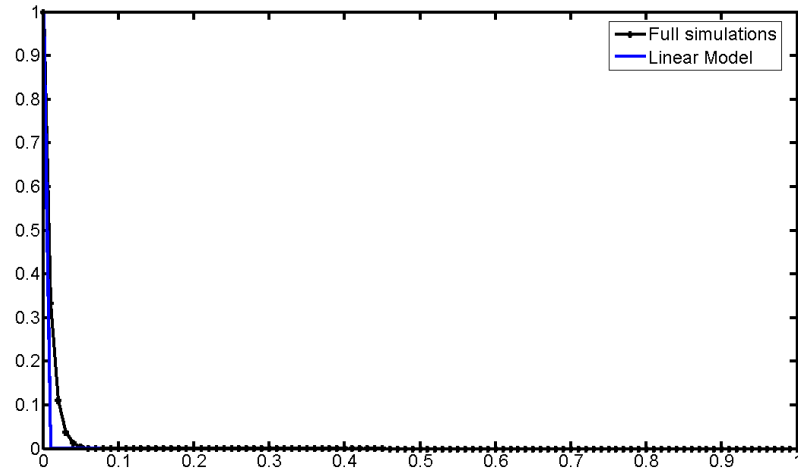


Figure 6.11: Comparison of the models with the full simulations if the diffusion coefficient is reduced to 0.01. The models are plotted only at the lowest working resolution. At all resolutions above it, the models are accurate.

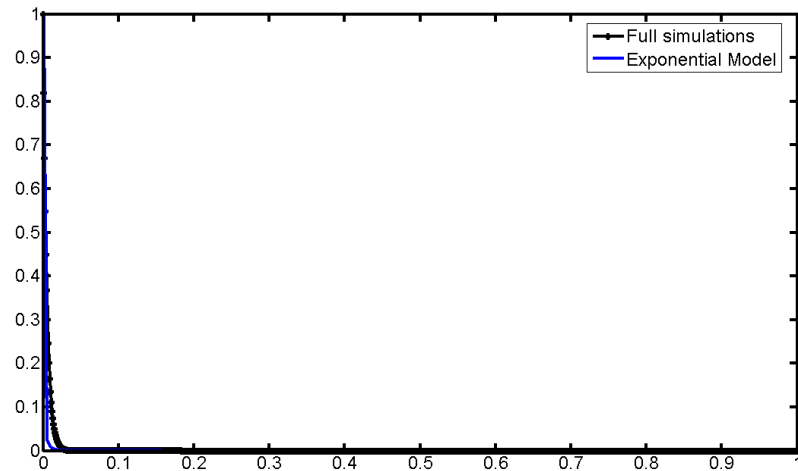
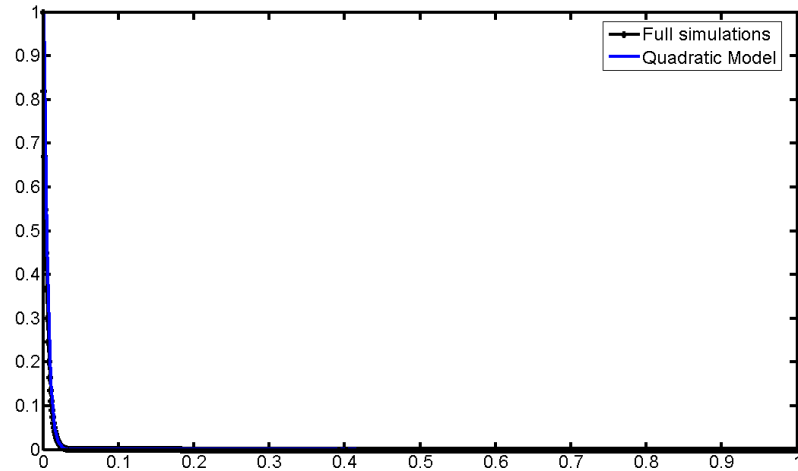
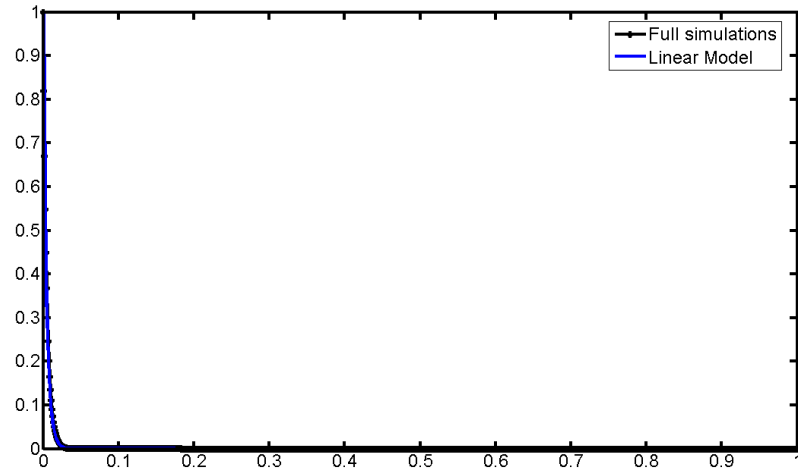


Figure 6.12: Comparison of the models with the full simulations if the diffusion coefficient is reduced to 0.005. The models are plotted only at the lowest working resolution. At all resolutions above it, the models are accurate.

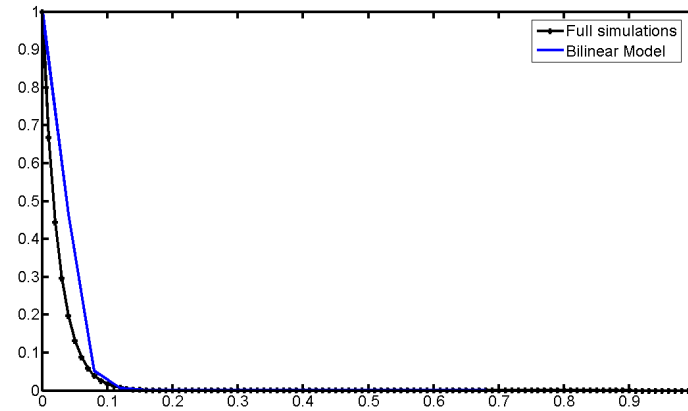
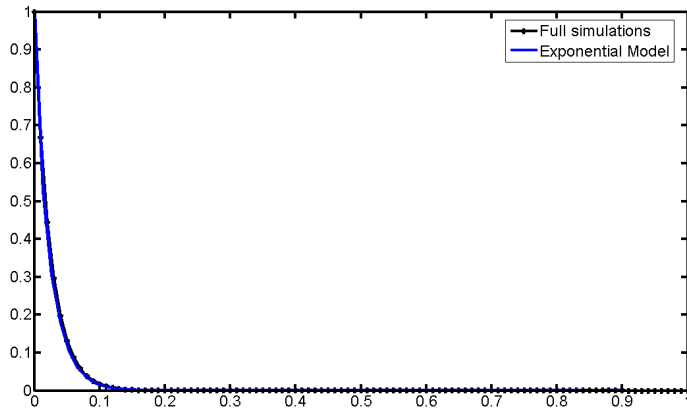
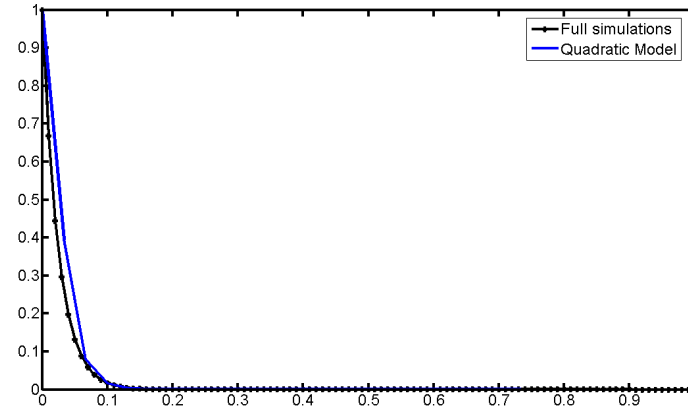
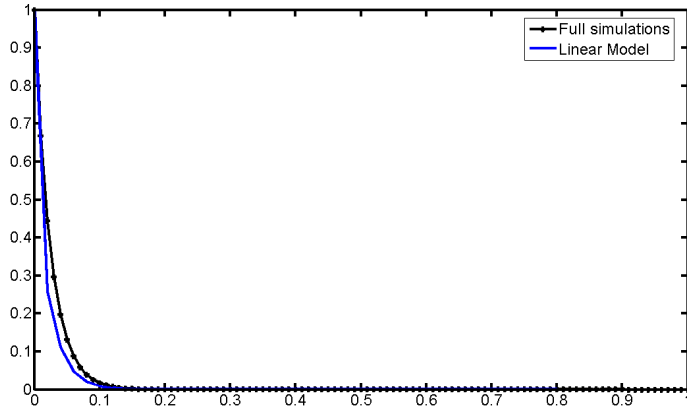


Figure 6.13: Comparison of the models with the full simulations if the velocity is doubled to 2. The models are plotted only at the lowest working resolution. At all resolutions above it, the models are accurate.

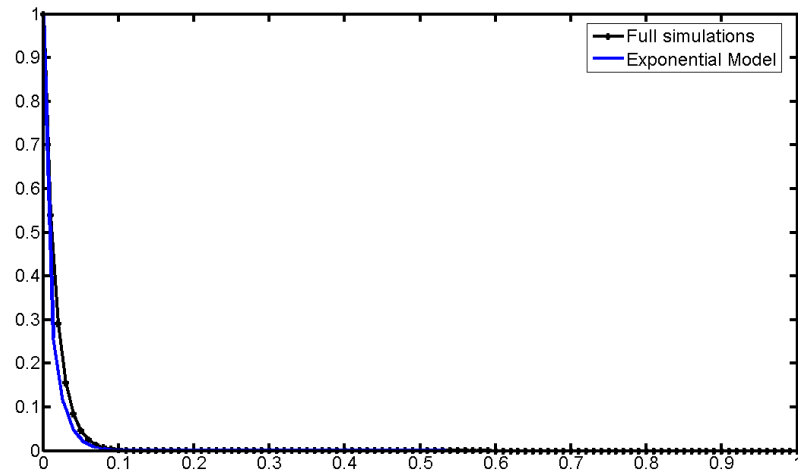
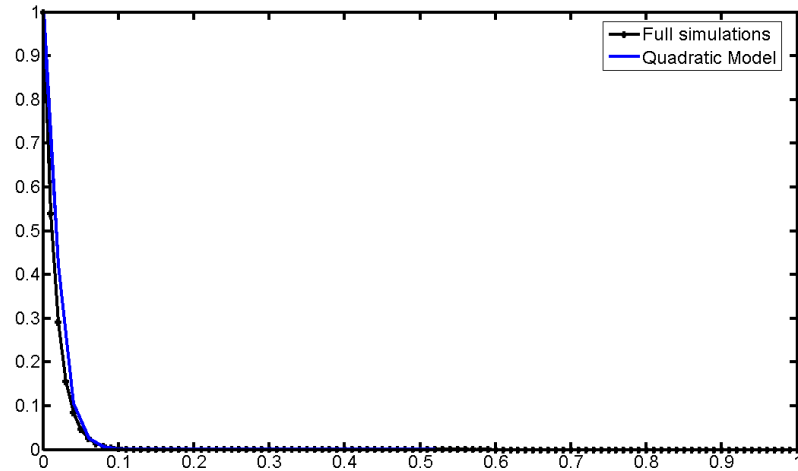
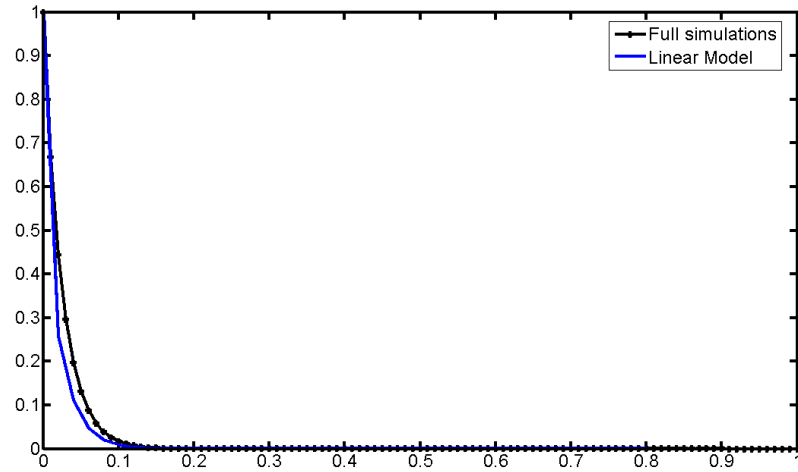


Figure 6.14: Comparison of the models with the full simulations if the velocity is tripled to 3. The models are plotted only at the lowest working resolution. At all resolutions above it, the models are accurate.

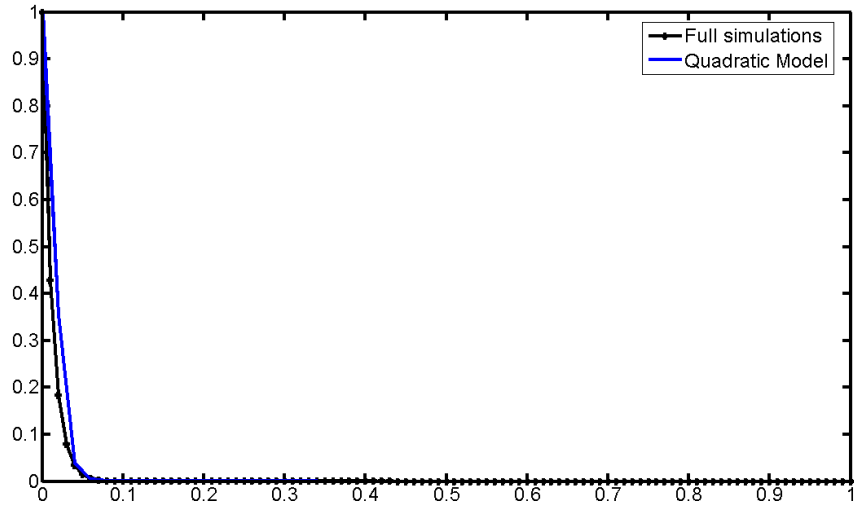


Figure 6.15: Comparison of the models with the full simulations if the velocity is quadrupled to 4. The quadratic model is plotted only at the lowest working resolution. At all resolutions above it, the model is accurate.

Number of grid points	End Time	Slope	Conc layer thickness
11	10.5	-15.000	0.0666667
21	10.5	-15.000	0.0666667
31	10.5	-15.000	0.0666667
51	10.5	-16.667	0.0599988
101	10.5	-18.182	0.0549995
201	10.5	-19.047	0.0525017
301	10.5	-19.3548	0.0516668
501	10.5	-19.6078	0.0510001
1001	10.5	-19.802	0.0504999

Table 6-1: Grid resolution for the full simulations at $U = 1$, $D = 0.05$.

Number of grid points	End Time	Slope	Conc layer thickness
11	10.5	Fails	NA
21	10.5	Fails	NA
31	10.5	-17.069	0.05858587
51	10.5	-17.6349	0.0567057
101	10.5	-18.4864	0.0540938
201	10.5	-19.1343	0.0522622
301	10.5	-19.3952	0.0515991
501	10.5	-19.6229	0.0509609
1001	10.5	-19.8058	0.0504903

Table 6-2: Grid resolution test for the linear model at $U=1$, $D=0.05$.

Number of grid points	End Time	Slope	Conc layer thickness
11	10.5	Fails	NA
21	10.5	Fails	NA
31	10.5	-17.069	0.05858587
51	10.5	-17.6349	0.0567057
101	10.5	-18.4864	0.0540938
201	10.5	-19.1343	0.0522622
301	10.5	-19.3952	0.0515991
501	10.5	-19.6229	0.0509609
1001	10.5	-19.8058	0.0504903

Table 6-3: Grid resolution test for the quadratic model at $U = 1$, $D = 0.05$.

Number of grid points	End Time	Slope	Conc layer thickness
11	10.5	-15.8579	0.0630601
21	10.5	-16.000	0.062500
31	10.5	-16.902	0.05858587
51	10.5	Fails	NA
101	10.5	Fails	NA
201	10.5	Fails	NA
301	10.5	Fails	NA
501	10.5	Fails	NA
1001	10.5	Fails	NA

Table 6-4: Grid resolution tests for the bi-linear model at $U = 1$, $D = 0.05$.

Number of grid points	End Time	Slope	Conc layer thickness
11	10.5	Fails	NA
21	10.5	Fails	NA
31	10.5	-18.000	0.0555556
51	10.5	-17.8571	0.0560001
101	10.5	-18.5185	0.0540001
201	10.5	-19.1388	0.0522499
301	10.5	-19.3966	0.0515554
501	10.5	-19.6232	0.0509601
1001	10.5	-19.8059	0.0504900

Table 6-5: Grid resolution tests for the exponential model. The slope is the inclination in the first grid interval where the exponential model is applied.

CHAPTER 7

-

SUMMARY AND FUTURE WORK

7.1 Summary

Multiphase flows simulations, as opposed to single phase flows, involve a greater numerical sophistication. To be able to predict two-phase flow requires accurate modeling of the complex interactions of fluid flow, surface tension, heat transfer and phase change. Empirical correlations have a place in engineering analysis of large scale multiphase systems, but they are often inadequate and inaccurate. The numerical methods described in the preceding chapters help to provide closure to multiphase systems accurately with a reduction in computational expense.

Computational techniques were developed for three different flow situations: droplet impact (Chapters 3 and 4), nucleate boiling (Chapter 5), and mass transfer (Chapter 6). In each case, a comprehensive set of “one-fluid” equations describing the phenomena, including the discontinuities in the material properties are first written down. The equations are solved using a front-tracking/finite difference based method. To accurately capture the flow within a reasonable amount of time, a mathematical model is incorporated, which is solved concurrently with the rest of the simulations and whose chief aim is to provide numerical descriptions of the small-scale features of the flow. The computational methodology and its results are validated through previously published work, and grid resolution studies.

The contributions made by this work include:

- Droplet Impact.

The development of a thin film model that accounts for thin films trapped between a drop and a solid wall in front tracking simulations, without the need for local adaptive grid refinement. The flexibility of the model in activating itself only when the drop is close enough to the wall and automatically reducing its contribution as the mesh size becomes finer is to be noted.

- Nucleate Boiling.

The phenomenon of microlayer evaporation adding to wall heat flux is captured with the help of a mathematical model. The microlayer model does not assume a fixed shape for the vapor bubble, and it is based on the position of the base of the bubble on the heated wall.

- Mass Transfer.

The variation of the concentration of species in the concentration boundary layer can be taken as one of a few self-similar profiles. The quadratic profile is found to be accurate and robust for a range of operating conditions.

7.2 Recommendations for future work

In this section, ideas for improving the numerical method and new avenues for research are explored.

7.2.1 Droplet Impact

The model presented is self-contained and although it has been implemented here only in two-dimensions, it can be extended to three dimensions. The present study will arrive at its logical conclusion when a three-dimensional model is solved concurrently with the three-dimensional full simulations. Our studies have only dealt with isothermal conditions in the domain. There is immense potential to combine the droplet impact studies with the energy equations solved in Chapter 5 to understand droplet impact on a heated wall. A prominent application of this phenomenon is impact cooling.

So far, only a single drop impact has been considered. When there is a series of drops, the interactions between the drops and between the drops and the ambient fluid will play an important role in the dynamics of the system. To study a train of droplets falling on a solid wall, with constant or variable frequency is an area that needs to be explored.

7.2.2 Nucleate Boiling

The first avenue for improvement would be the addition of more nucleation sites. It would be a worthy exercise to study the effect of bubble dynamics, how the number of nucleation sites and their relative spacing influences the overall heat transfer.

The heated wall is considered to be a “thermal reservoir” of sorts. Its temperature does not change even when heat is transferred out of it. If heated body is relatively small in size, the concept of the isothermal wall will not hold. Therefore, the temperature changes in the wall have to be accounted for, when dealing with practical applications, like electronic cooling.

Three-dimensional studies will be very constructive in providing more accurate statistical information and a better description of the phenomenon. Our study has focused only a single cycle of bubble nucleation, growth and departure. The next step in improving the present setup would be to incorporate multiple cycles so as to ensure that the average behavior over a series of cycles do not change by much. Adding a thermal boundary layer will be useful when the wall superheat is large to make sure that the time taken for the thermal boundary layer to develop does affect the heat transfer statistics.

7.2.3 Mass Transfer

The simulations are one-dimensional. The obvious path is to broaden the current formulation to two and three dimensions. This is definitely more involved and complex analysis, but beneficial for a full-scale simulation of 2-D or 3-D mass transfer problems.

Although the models were derived for the purpose of mass transport, the profiles can be extended to any transient field equation that contains the transport of a passive scalar. Numerical simulations of chemical reactions, combustion modeling, species transport in turbulence modeling are only some of the areas that the models can be

used. These equations, coupled with actual models of real, physical systems will generate a greater understanding of the boundary effects in different transport phenomena.

BIBLIOGRAPHY

1. Hamming R.W., “*Numerical Methods for Scientists and Engineers*”, New York: McGraw-Hill, (1962).
2. Buzbee B.L., “Gaining insight from Supercomputing”, *Proc. IEEE*, **72** (1), 19-21 (1984).
3. Harlow F.H, and J. E. Welch, “Numerical Calculation of Time-Dependent Viscous Incompressible Flow of Fluid with Free Surface”, *Phys. Fluids*, **8**, 2182-2189 (1965).
4. Hirt, C.W. and Nichols B.D., “Volume of fluid method (VOF) for the dynamics of free boundaries”, *J. Comput. Phys.*, **39**, 201-225 (1981).
5. Unverdi S.O. and Tryggvason G., “A front-tracking method for viscous incompressible flows”, *J. Comput. Phys.*, **100**, 25-37 (1992).
6. Brackbill J.U., Kothe D.B., and Zemach C., “A continuum method for modeling surface tension”, *J. Comput. Phys.*, **100**, 335 (1992).
7. Osher S., and Sethian J. A., “Fronts propagating with curvature-dependent speed: Algorithms based on Hamilton-Jacobi formulations”, *J. Comput. Phys.*, **79**, 2-49 (1988).
8. Jacqmin D., “Calculation of two-phase Navier-Stokes flows using phase-field modeling”, *J. Comput. Phys.*, **155**, 96-127 (1999).
9. Takewaki H., Nishiguchi A. and Yabe T., “Cubic interpolated pseudo-particle method (CIP) for solving hyperbolic-type equations”, *J. Comput. Phys.*, **61**, 261-268 (1985).
10. Longuet-Higgins M.S., and Cokelet E.D., "The Deformation of Steep Surface Waves on Water. I. A Numerical Method of Computation.", *Proc. R. Soc. London A*, **350**, 1-26 (1976).
11. Youngren, G.K. and Acrivos A., “Stokes flow past a particle of arbitrary shape. A numerical method of solution.”, *J. Fluid Mech.*, **69**, 377-403 (1975).
12. Ryskin G. and Leal L. G., “Numerical solution for free-boundary problems in fluid mechanics”, *J. Fluid Mech.*, **148**, 1-17 (1984).
13. Greenbaum, A., “*Iterative Methods for Solving Linear Systems*”, Society for Industrial and Applied Mathematics, Philadelphia, 1997.
14. Tryggvason, G. Bunner, B., Esmaeeli A., Juric, D., Al-Rawahi N., Tauber W., Han J., Nas S., and Jan Y.-J., “A front tracking method for the computations of multiphase flow”, *J. Comput. Phys.*, **169**, 708-759 (2001).

15. Esmaeeli A., and Tryggvason G., “Direct numerical simulations of bubbly flows. Part I – Low Reynolds number arrays”, *J. Fluid Mech.*, **377**, 313-345 (1998).
16. Esmaeeli A., and Tryggvason G., “Direct numerical simulations of bubbly flows. Part I – Moderate Reynolds number arrays”, *J. Fluid Mech.*, **385**, 325-358 (1999).
17. Bunner B., and Tryggvason G., “Dynamics of homogenous bubbly flows: Part I. Rise velocity and microstructure of the bubbles”, *J. Fluid Mech.*, **466**, 17-52, (2002).
18. Bunner B., and Tryggvason G., “Dynamics of homogenous bubbly flows: Part I. Fluctuations of the bubbles and the liquid”, *J. Fluid Mech.*, **466**, 53-84, (2002).
19. Lu J., Fernandez A., and Tryggvason G., “The effect of bubbles on the wall shear in a turbulent channel flow”, *Phys. Fluids*, **17**, 093303, (2005).
20. Han J., “*Numerical studies of drop motion in axisymmetric geometry*”, PhD Thesis, University of Michigan, (1998).
21. Weatherburn, C.E., “*Differential Geometry of Three Dimensions*”, Cambridge University Press, London, (1927).
22. Clift R., Grace J. R., and Weber M. E., “*Bubbles, Drops and Particles*”, Academic Press Inc., San Diego (1978).
23. Harlow F.H. and Shannon J. P., “The Splash of a Liquid Drop”, *J Appl. Phys.*, **38**, 3855 (1967).
24. Lesser M., “Thirty years of liquid impact research: a tutorial review”, *Wear*, 186-187, 28-34 (1995).
25. Lesser M. B., “The Impact of Compressible Liquids”, *Ann. Rev. Fluid Mech.*, 97-122, (1983).
26. Rodriguez F. and Mesler R., “Some drops do not splash”, *J. Colloid Interface Sci.*, **106**(2), 347-352 (1985).
27. Rein M., “Phenomena of liquid drop impact on solid and liquid surfaces”, *Fluid Dyn. Res.*, **12**, 61-93 (1993).
28. Prosperetti A. and Oguz H. N., “The impact of drops on liquid surfaces and the underwater noise of rain”, *Ann. Rev. Fluid Mech.*, 577-602 (1993).
29. Morton D., Rudman M., Liow J-L, “An investigation of the flow regimes resulting from splashing drops”, *Phys. Fluids*, **12**, 747 (2000).
30. Trujillo M. F. and Lee C. F., “Modeling crown formation due to the splashing of a droplet”, *Phys. Fluids*, **13**, 2503 (2001).
31. Thoroddsen S. T., “The ejecta sheet generated by the impact of a drop”, *J. Fluid Mech.*, **451**, 373-381 (2002).

32. Davidson M. R., "Spreading of an inviscid drop impacting on a liquid film", *Chem. Engg. Science*, **57**, 3639-3647 (2002).
33. Yarin A. L. and Weiss D. A., "Impact of drops on solid surfaces: self-similar capillary waves, and splashing as a new type of kinematic discontinuity", *J. Fluid Mech.*, **283**, 141-173 (1995).
34. Xie H., Koshizuka S., and Oka Y., "Modelling of a single drop impact onto liquid film using particle method", *Int. J. Numer. Meth. Fluids*, **45**, 1009-1023 (2004).
35. Shin J. and McMahon T. A., "The tuning of a splash", *Phys. Fluids A*, **2** (8), 1312-1317 (1989).
36. Manzello S. L. and Yang J.C., "An experimental study of a water droplet impinging on a liquid surface", *Exps. Fluids*, **32**, 580-589 (2002).
37. Rein M., "The transitional regime between coalescing and splashing drops", *J. Fluid Mech.*, **306**, 145-165 (1996).
38. Gunjal P. R., Ranade V., and Chaudhari R. V., "Dynamics of drop impact on solid surfaces: Experiments and VOF simulations", *AIChE Journal*, **51**, 1, 59-77 (2005).
39. Pasanzadeh-Fard M., Qiao Y. M., Chandra S., and Mostaghimi J., "Capillary effects during droplet impact on a solid surface", *Phys. Fluids*, **8**, 3, 650-659 (1996).
40. Mao T., Kuhn D.C.S., and Tran H., "Spread and Rebound of Liquid Droplets upon Impact on Flat Surfaces", *AIChE Journal*, **43**, 2169-2179 (1997).
41. Bussmann M. "On a three-dimensional volume tracking method of droplet impact", *Phys. Fluids*, **11**, 1406 (1999).
42. Busmann, M. Chandra S. and Mostaghimi J., "Modeling the splash of a droplet impacting a solid surface", *Phys. Fluids*, **12**, 3121-3132 (2000).
43. Josserand C. and Zaleski S., "Droplet splashing on a thin liquid film", *Phys. Fluids*, **15**, 1650 (2003).
44. Weiss D. A. and Yarin A. L., "Single Drop Impact onto liquid films: neck distortion, jetting, tiny bubble entrainment, and crown formation", *J. Fluid Mech.*, **385**, 229-254, (1999).
45. Fedorchenko A. and Wang A., "On some common features of drop impact on liquid surfaces", *Phys. Fluids*, **16**, 1349 (2004).
46. Trujillo M. F., and Lee C. F., "Modeling crown formation due to the splashing of a drop", *Phys. Fluids*, **13**, 9, 2503-2516 (2001).
47. Cossali G. E., Marengo M., Coghe A and Zhadnov S., "The role of time in single drop splash on thin film", *Exp. Fluids* **36**, 888-900 (2004).
48. Batchelor G. K., "*An introduction to fluid dynamics*", Cambridge University Press, Cambridge, UK (1967).

49. Panton R. L., *"Incompressible Flow"*, John Wiley & Sonc, Inc., New York (1996).
50. Oron A., Davis S. H., and Bankoff S. G., "Long scale evolution of thin films", *Rev. Mod. Phys.*, **69**, 931-980 (1997).
51. Werder T., Welther J. H., and Koumoutsakos P., "Hybrid atomistic–continuum method for the simulation of dense fluid flows", *J. Comput. Phys.*, **205**, 373-390 (2005).
52. Nie X. B., Chen S. Y., E W. N., and Robbins M. O., "A continuum and molecular dynamics hybrid method for micro and nano-fluid flow", *J. Fluid Mech.*, **500**, 55-64 (2004).
53. Nukiyama S., "The maximum and minimum values of heat Q transmitted from metal to boiling water under atmospheric pressure", *Int. J. Heat Mass Transfer*, **9**, 1419-1433 (1966).
54. Tong L.S., *"Boiling Heat Transfer and Two-Phase Flow"*, John Wiley & Sons, New York, (1965).
55. Rohsenow W. M., "A method of correlating heat transfer data for surface boiling of liquids", *Trans. ASME*, **84**, 969 (1962).
56. Cooper M. G., and Lloyd A. J. P., "The microlayer in nucleate pool boiling", *Int. J. Heat Mass Transfer*, **12**, 895-913 (1969).
57. Gaertner R. F., "Photographic study of nucleate pool boiling on a horizontal surface", *J. Heat Transfer*, **87**, 17-29 (1965).
58. Judd R. L. and Hwang K. S., "Comprehensive model for nucleate pool boiling including microlayer evaporation", *J. Heat Transfer*, **98**, 4, 623-639(1976)
59. Ohta H., Kawasaki K., Okada S., Azuma H., Yoda S., and Nakamura T., "On the heat transfer mechanisms in microgravity nucleate boiling", *Adv. Space Res.*, **24**, 10, 1325-1330 (1999).
60. Lay J. H. and Dhir V. K., "Shape of a vapor stem during nucleate boiling of saturated liquids", *J. Heat Transfer*, **117**, 394-401 (1995).
61. Cooper M.G., "The microlayer and bubble growth in nucleate pool boiling", *Int. J. Heat Mass Transfer*, **12**, 915-933 (1969)
62. Wayner P.C. Jr, "Long range intermolecular forces in change-of-phase heat transfer", *Proceedings of the 33rd National Heat Transfer Conference*, Albuquerque New Mexico, (1999).
63. Son G., Dhir V.K., and Ramanujapu N., "Dynamics and heat transfer associated with a single bubble during nucleate boiling on a horizontal surface", *J. Heat Transfer*, **121**, 623-631 (1999).

64. Mukherjee A., and Kandlikar S. G., “Numerical study of single bubbles with dynamic contact angle during nucleate pool boiling”, *Int. J. Heat Mass Transfer*, **50**, 127-138 (2007).
65. Mann M., Stephan K., and Stephan P., “Influence of heat conduction in the wall on nucleate boiling heat transfer”, *Int. J. Heat Mass Transfer*, **43**, 2193-2203 (2000).
66. Plesset M. S. and Zwick S. A., “The growth of vapor bubbles in superheated liquids”, *J. Appl. Phys.*, **25**, 493 (1954).
67. Takata Y., Shirakawa H., Kuroki T., and Ito T., “Numerical analysis of a single bubble departure from a heated surface”, *Proceedings of the 11th IHTC*, Vol. **4**, 355-360 (1998).
68. Esmaeeli, A. and Tryggvason G., “Computations of explosive boiling in microgravity”, *J. Sci. Comp.*, **19**, 163-182 (2003).
69. Esmaeeli, A. and Tryggvason G., “Computations of film boiling. Part I: numerical method”, *Int. J. Heat Mass Transfer*, **47**, 5451-5461 (2004).
70. Welch S.W.J., and Wilson J., “A volume of fluid method for fluid flows with phase change”, *J. Comput. Phys.*, **160**, 662-682 (2000).
71. Yoon H.Y., Koshizuka S., and Oka Y., “Direct calculation of bubble growth, departure and rise in nucleate pool boiling”, *Int. J. Multiphase Flow*, **27**, 277-298 (2001).
72. Lakehal D., Meier M. and Fulgosi M., “Interface tracking towards the direct simulation of heat and mass transfer in multiphase flows”, *Int. J. Heat Mass Transfer*, **23**, 242-257 (2002).
73. Shin S., and Juric D., “Modeling three-dimensional multiphase flow using a level contour reconstruction method for front tracking without connectivity”, *J. Comput. Phys.*, **180**, 427-470 (2002).
74. Shin S., Abdel-Khalik S.I., and Juric D., “Direct three-dimensional numerical simulation of nucleate boiling using the level contour reconstruction method”, *Int. J. Mutliphase Flow*, **31**, 1231-1242 (2005).
75. Tu J.Y. and Yeoh G.H., “On numerical modeling of low-pressure subcooled boiling flows”, *Int. J. Heat Mass Transfer*, **45**, 1197-1209 (2002).
76. Zhao Y.-H., Masuoka T., and Tsuruta T., “Unified theoretical prediction of fully developed nucleate boiling and critical heat flux based on a dynamic microlayer model”, *Int. J. Heat Mass Transfer*, **45**, 3189-3197 (2002).
77. Das A. K., Das P. K., and Saha P., “Heat transfer during pool boiling based on evaporation from micro and macrolayer”, *Int. J. Heat Mass Transfer*, **49**, 3487-3499 (2006).
78. Dhir V.K., “Boiling heat transfer”, *Ann. Rev. Fluid Mech.*, **30**, 365-401 (1998).

79. Seigel R., and Keshock E. G., "Effects of reduced gravity on nucleate boiling bubble dynamics in saturated water.", *AIChE Journal*, Vol **10**, 509-517 (1964).
80. Plesset M.S., and Prosperetti A., "The contribution of latent heat transport in subcooled nucleate boiling", *Int. J. Heat Mass Transfer*, **21**, 725-734 (1978).
81. Baehr H.D. & Stephan K., "*Heat and Mass Transfer*", Springer, New York, 2nd Edition (2006).
82. Chen Y-M. and Sun C-Y., "Experimental study on the heat and mass transfer of a combined absorber-evaporator exchanger", *Int. J. Heat Mass Transfer*, **40**, 961-971 (1997).
83. Doan H. D., Fayed M. E., and Trass O., "Measurement of local and overall mass-transfer coefficients to a sphere a quiescent using a limiting current technique", *Chem. Engg. Journal*, **81**, 53-61 (2001).
84. Gumerov N. A., "The heat and mass transfer of a vapor bubble with translatory motion at high Nusselt numbers", *Int. J. Multiphase Flow*, **22**, 259-272 (1996).
85. Piarah W. H., Paschedag A., and Kraume M., "Numerical simulation of mass transfer between a single drop and an ambient flow", *AIChE Journal*, **47**, 1701-1704 (2001).
86. Favelukis M. and Mudunuri R. R., "Unsteady mass transfer in the continuous phase around axisymmetric drops of revolution", *Chem. Engg. Science*, **58**, 1191-1196 (2003).
87. Davidson M. R. and Rudman M., "Volume-of-fluid calculation of heat or mass transfer across deforming interfaces in two-fluid flow", *Numerical Heat Transfer, Part B*, **41**, 291-308 (2002).
88. Goldstein R. J., and Cho H. H., "A review of mass transfer measurements using naphthalene sublimation", *Expt. Thermal Fluid Science*, **10**, 416-434 (1995).
89. Yusuf R., Melaaen M. C., and Mathiesen V., "Convective heat and mass transfer modeling in gas fluidized beds", *Chem. Eng. Technology*, **28**, 13-24 (2005).
90. Vasconcelos J. M. T., Orvalho S. P., and Alves S. S., "Gas-liquid mass transfer to single bubbles: effect of surface contamination", *Fluid Mechanics and Transport Phenomena*, **48**, 1145-1154 (2002).
91. Jung R.-T. and Sato T., "Direct numerical simulation on single-droplet flow with mass transfer", *Chem. Eng. Technology*, **24**, 1071-1075 (2001).
92. Ponoth S. S. and McLaughlin J. B., "Numerical simulation of mass transfer for bubbles in water", *Chem. Eng. Science*, **55**, 1237-1255 (2000).
93. Sharifullin V. N. and Luebbert A., "Mass transfer from a single bubble in the presence of surfactants", *Theoretical Foundations of Chem. Eng.*, **36**, 230-234 (2002).
94. Alves S. S., Orvalho S. P., and Vasconcelos J. M. T., "Effect of bubble contamination on rise velocity and mass transfer", *Chem. Eng. Science*, **60**, 1-9 (2005).

95. Sato T., Jung R.-T., and Abe S., "Direct simulation of droplet flow with mass transfer at interface", *Trans. ASME*, **122**, 510-516 (2000).
96. Lim E. W. C., Koh S. W., Lim L. K., Ore S. H., Tay B. K., Ma Y. and Wang C.-H., "Experimental and computational studies of liquid aerosol evaporation", *Aerosol Science*, **39**, 618-634 (2008).
97. Husain M. M. and Dincer I., "Two-dimensional heat and moisture transfer analysis of a cylindrical moist object subjected to drying: A finite-difference approach", *Int. J. Heat Mass Transfer*, **46**, 4033-4039 (2003).
98. Kaya A., Aydin O., and Dincer I., "Numerical modeling of heat and mass transfer during forced convection drying of rectangular moist objects", *Int. J. Heat Mass Transfer*, **49**, 3094-3103 (2006).
99. Queiroz M. R. and Nebra S. A., "Theoretical and experimental analysis of the drying kinetics of bananas", *J. Food Eng.*, **47**, 127-132 (2001).
100. Tiwari G. N., Minocha A., Sharma P. N, and Khan M. E., "Simulation of convective mass transfer in a solar distillation process", *Energy Convers. Mgmt.*, **38**, 761-770 (1997).
101. Mezhericher M., Levy A. and Borde I., "Heat and mass transfer of single droplet/wet particle drying", *Chem. Eng. Sci.*, **63**, 12-23 (2008).
102. Li Z. M., Peng X. F. and Lee D. J., "Interfacial mass transfer around a vapour bubble during nucleate boiling", *Heat Mass Transfer*, 5-11 (2004).
103. Radl S., Tryggvason G., Khinast J., "Flow and mass transfer of fully resolved bubbles in non-Newtonian fluids", *AIChE Journal*, **53**, 1861-1878 (2007).
104. Ma P., Li X. and Ku D. N., "Convective mass transfer at the carotid bifurcation", *J. Biomechanics*, **30**, 565-571 (1997).
105. Koynov A., Khinast J. G. and Tryggvason G., "Mass transfer and chemical reactions in bubble swarms with dynamic interfaces", *AIChE Journal*, **51**, 2786-2800 (2005).
106. Koynov A., Tryggvason G., Schluter M., and Khinast J. G., "Mass transfer and chemical reactions in reactive deformable bubble swarms", *Appl. Phys. Letters*, **88**, 134102 (2006).
107. Tryggvason G. and Dahm W. J., "An integral method for mixing, chemical reactions and extinction in unsteady strained diffusion layers", *Combust. and Flame*, **83**, 207-220 (1991).
108. Chang C. H. H., Dahm W. J. and Tryggvason G., "Lagrangian model simulations of molecular mixing, including finite rate chemical reactions, in a temporally developing shear layer", *Phys. Fluids A*, **3**, 1300-1311 (1992).
109. Dahm W. J., Tryggvason G. and Zhuang M., "Integral method solution of time-dependent strained diffusion-reaction layers with multistep kinetics", *SIAM J. Appl. Math.*, **56**, 1039-1059 (1996).

110. Dahm W. J., Tryggvason G. and Zhuang M., "Integral method solution of time-dependent strained diffusion-reaction layers with multistep kinetics", *SIAM J. Appl. Math.*, **56**, 1039-1059 (1996).